

THE EFFECT OF CRYSTAL DEFECTS
ON MICRODIFFRACTION PATTERNS

BY

JOHN BEVERLY WARREN

A DISSERTATION PRESENTED TO THE GRADUATE COUNCIL OF
THE UNIVERSITY OF FLORIDA IN PARTIAL
FULFILLMENT OF THE REQUIREMENTS FOR THE DEGREE OF
DOCTOR OF PHILOSOPHY

UNIVERSITY OF FLORIDA
1978

ACKNOWLEDGMENTS

The author wishes to express his sincere gratitude to his advisor, Dr. J. J. Hren, whose continuing encouragement during a decade spanning periods of graduate study, military service and employment in industry enabled the author to complete his degree. In addition, the advice of the supervisory committee, Dr. C. S. Hartley, Dr. R. E. Reed-Hill, Dr. R. T. DeHoff and Dr. M. Eisenberg, was most useful in the final preparation of the manuscript.

Support from the Department of Materials Science in the form of a research assistantship is also gratefully acknowledged.

Finally, the author thanks his wife for her unending patience and encouragement.

TABLE OF CONTENTS

	page
ACKNOWLEDGMENTS.....	ii
ABSTRACT.....	v
CHAPTER	
1 INTRODUCTION.....	1
2 THE EFFECT OF A CONVERGENT ELECTRON BEAM ON ELECTRON SCATTERING.....	6
2.1 A Review of Electron Diffraction and the Reciprocal Lattice.....	6
2.2 A Review of the Dynamical Theory of Electron Diffraction.....	10
2.3 The Effect of STEM on the Reciprocal Lattice Construction.....	18
2.4 The Effect of STEM on the Dynamical Theory....	22
2.5 A STEM Computer Simulation Program.....	29
3 MICRODIFFRACTION METHODS.....	47
3.1 A Review of the Effect of Inelastic Scattering on the Diffraction Pattern.....	47
3.2 The Use of Channeling Patterns to Characterize Polycrystalline Specimens.....	61
3.3 A Review of Ray Optics for Convergent Beam Diffraction.....	65
3.4 The Effect of Lens Aberrations.....	77
3.5 A Review of the Rocking Beam Micro- diffraction Method.....	81
3.6 Transmission Channeling Patterns by the Rocking Beam Method.....	88

TABLE OF CONTENTS (continued)

CHAPTER		page
4	EXPERIMENTAL PROCEDURES AND MATERIALS.....	94
	4.1 Ray Optics and Computations.....	94
	4.2 Sample Preparation.....	105
	4.3 The Character of the Dislocations Introduced.....	111
	4.4 Determination of Crystal Directions by Diffraction Patterns.....	115
5	EXPERIMENTAL RESULTS.....	121
	5.1 A Comparison of the Microdiffraction Methods.....	121
	5.2 Identification of Crystal Defects by Microdiffraction.....	135
	5.3 Computer Simulation of STEM Crystal Defect Images.....	143
	5.4 Determination of Grain Orientation of a Fine-grained Superalloy Using Focused Condenser Aperture Micro- diffraction.....	156
6	CONCLUSIONS AND SUGGESTIONS FOR FUTURE RESEARCH.....	163
	APPENDIX.....	167
	REFERENCES.....	173
	BIOGRAPHICAL SKETCH.....	175

Abstract of Dissertation Presented to the
Graduate Council of the University of Florida in Partial
Fulfillment of the Requirements for the Degree of Doctor of Philosophy

THE EFFECT OF CRYSTAL DEFECTS
ON MICRODIFFRACTION PATTERNS

by

John Beverly Warren

June, 1978

Chairman: Dr. J. J. Hren
Major Department: Materials Science and Engineering

The various modes of microdiffraction that can be performed with an electron microscope equipped with a scanning transmission attachment are examined from both an experimental and a theoretical standpoint. Particular attention is paid to the development of microdiffraction to analyze crystal defects such as dislocations and stacking faults.

The objective lens of the scanning transmission electron microscope forms a focused electron probe with a comparatively large convergence angle. Such a probe can produce a convergent beam diffraction pattern from an area on a crystalline specimen as small as $50 \overset{\circ}{\text{Å}}$ in diameter. The scanning coils used to raster the probe over the specimen can also be used to rock a well-collimated electron beam over a region of the specimen in such a way that a microdiffraction pattern is formed on the cathode ray tube normally used to display the specimen image. By varying either the convergence angle of the incident beam or the transmitted beam it is possible in both of these methods to

produce microdiffraction patterns with high angular resolution or transmission channeling patterns with low angular resolution but excellent signal-to-noise ratios.

In every case, the convergence angles of the incident and transmitted electron beams determine the appearance of the specimen image and the associated diffraction pattern. The Howie-Whelan dynamical theory must be modified to correctly predict the intensities of the scattered beams present in the diffraction pattern as well as the diffraction contrast image of crystal defects.

Computer programs that simulate the electron beam-specimen interaction for the convergent beam case are developed and compared to experiment. A numerical method that utilizes transmission channeling patterns to precisely determine the orientation of a crystalline specimen and an electron beam is also presented.

CHAPTER 1 INTRODUCTION

Since the advent of Scanning Transmission Electron Microscopy (STEM), several years ago, it was expected that STEM techniques would provide increased specimen penetration, electronically enhanced image quality, and improved capabilities to analyze areas a few nanometers in diameter by microdiffraction and energy dispersive X-ray microanalysis. For crystalline materials where diffraction contrast imaging plays the dominant role, only the last of these, the analysis of a small region excited by a stationary electron probe, has enjoyed a measure of success.

This thesis examines the ability of the STEM probe to form a microdiffraction pattern from a column of material roughly equal to its own diameter. A microdiffraction pattern formed by this method can be produced from an area more than two orders of magnitude smaller than the patterns from standard selected area diffraction. While this method is the most direct of several possible microdiffraction techniques, most work up to now has been limited by the poor angular resolution in the pattern resulting from the convergent TEM probe and by the high contamination rates associated with it.

Another approach, rocking beam diffraction, circumvents the limitations of the stationary electron probe and is also studied in detail. Here, the deflection coils in the upper half of the microscope

column, used to scan the probe across the specimen in the normal mode of operation, are adjusted to rock a well-collimated electron beam about a pivot-point level with the specimen, thus producing a time-dependent display of the variations of electron scattering as a function of the angle of rock. If an objective aperture of appropriate size is placed below the specimen plane, the rocking motion of the incident beam results in the bright field and the associated dark field images being swept over the STEM detector. This motion forms a simulated diffraction pattern on the STEM cathode ray tube that corresponds precisely to the portion of the sample image "seen" by the detector. Since the incident beam is relatively well-collimated, contamination rates are much lower than for convergent beam STEM microdiffraction. Angular resolution is now controlled by the objective aperture, and can be varied from values comparable to those found in standard selected area diffraction to values that result in low angular resolution but produce a scanning transmission channeling pattern with an excellent signal-to-noise ratio.

For all methods of microdiffraction, the convergence angles of the incident and scattered beams are the crucial factors that determine the manner in which the information in the microdiffraction pattern is presented. In convergent beam microdiffraction, gradually increasing α_i , the semi-angle of incidence, changes the appearance of the pattern from the normal diffraction spot array to a transmission channeling pattern where discrete diffraction spots are no longer visible. Although the method of formation is quite different, the rocking beam method can produce a similar variety of effects if α_o ,

the exit semi-angle, is varied by changing the objective aperture size.

Once the basic concepts of convergent beam and rocking beam microdiffraction can be quantitatively described, they can be used to solve problems of interest to the metallurgist. In this work, these techniques are used to examine dislocation strain fields, stacking fault images, and to provide very accurate information on the orientation of adjacent areas in fine-grain polycrystalline materials.

The information provided by microdiffraction from small distorted regions of the specimen close to the defects is comparable in many respects to that provided by the computer simulation of defect diffraction contrast images. To review, the computer simulation method numerically integrates two or more simultaneous differential equations that describe the interaction of the transmitted and scattered beams as they pass through the crystal lattice. If the equations are solved for several thousand columns in the vicinity of a defect strain field, and the solutions (for example, the bright field intensity, $|T|^2$, or the dark field intensity, $|S|^2$) are plotted in a dot matrix to form a picture, a simulation of the experimental diffraction contrast image of the defect can be formed.

The major limitation of the computer simulation technique is simply the time required to compute the interaction for each of several thousand columns before the simulation can be formed. Computation time for n-beam situations, where there are several strongly excited beams, escalates accordingly. In practice, computer simulation is limited to the two-beam case, where information from only one

diffraction plane is available in the image. Thus, several simulated images are needed to completely characterize a defect strain field.

Microdiffraction can aid the computer simulation process by providing the $|S|^2/|T|^2$ value directly from the diffraction pattern resulting from a column passing through the dislocation strain field that is less than 100 \AA in diameter. By comparing the calculated ratios to the experimental ones for several columns spaced along the dislocation, it should be possible to identify the dislocation with a much smaller expenditure of computation time. Such a procedure could be done with ordinary Transmission Electron Microscopy (TEM) techniques only by measuring the intensity in the bright field and dark field images at precisely the same point. This is not possible with ordinary TEM for two reasons. First, the process of obtaining a dark field image involves tilting the beam, and it is very difficult to get a dark field image with precisely the same Bragg deviation as the associated bright field image. Second, it is very difficult to locate exactly the same specimen point on different two-beam images due to the diffuse nature of the image itself.

When the STEM probe is used to display the defect image on the Cathode Ray Tube (CRT) in the scanning mode, the probe convergence plays an important role in determining the appearance of the crystal defect image. The convergence effect must be carefully controlled if STEM images are to be used for computer simulation, and this point is explored by examining the effect of beam convergence on computer simulated images of stacking faults in silicon.

For crystal orientation problems, the electron-beam specimen orientation can be determined directly from the Kikuchi lines (or channeling lines for high convergence angles) present in the microdiffraction pattern. The diffraction spots themselves persist over specimen tilts of several degrees, and cannot be used to determine the local electron beam direction.

The location of both Kikuchi and channeling patterns is defined by the intersection of the Bragg diffracting cones of apex angle $180^\circ - 2\theta_B$ and the Ewald sphere. Each diffracting cone is normal to a particular diffracting plane and local lattice rotation caused by defect strain fields rotates each cone to a new position. Measurement of the relative shift of the lines in the microdiffraction pattern can be used to determine the precise crystal orientation of the crystal volume producing the pattern. While this approach can be accomplished with standard selected area diffraction, it has been limited to areas larger than $2 \mu\text{m}$ in diameter and to low atomic number materials where Kikuchi lines are more readily formed. Microdiffraction, and in particular, transmission channeling formed by a highly convergent probe overcomes both of these limitations.

In summary, this thesis uses several microdiffraction techniques to analyze individual crystal defects and also to solve orientation problems in polycrystalline materials. The advantages and disadvantages of each technique will be compared, but it will be shown that all of the phenomena in any type of microdiffraction pattern are critically dependent upon the convergence angle of the incident electron beam.

CHAPTER 2

THE EFFECT OF A CONVERGENT ELECTRON BEAM ON ELECTRON SCATTERING

2.1 A Review of Electron Diffraction and the Reciprocal Lattice

Scanning Transmission Electron Microscopy (STEM) enables the production of microdiffraction patterns two orders of magnitude smaller than previous techniques (Geiss, 1975). However the short focal length objective lens used to produce a small, focused spot for STEM results in a far more convergent beam impinging on the specimen than standard TEM techniques. It is necessary to understand how a highly convergent electron beam effects diffraction contrast imaging if the STEM microdiffraction patterns are to be correctly interpreted.

The difference between imaging with TEM and STEM can be readily understood with the aid of geometrical ray optics (Fig. 2.1). In TEM, the upper half of the objective lens in the Philips 301 electron microscope forms a collimated beam of radiation that impinges upon the specimen and is focused by the lower half of the objective lens field to a point in its back focal plane (Thompson, 1977). In STEM, the upper half of the objective lens produces a focused probe in the specimen plane. This probe diverges after passing through the specimen but the lower objective lens field partially refocuses the probe and forms a stationary, convergent beam diffraction pattern in the same objective focal plane as in TEM.

(a) TEM

(b) STEM

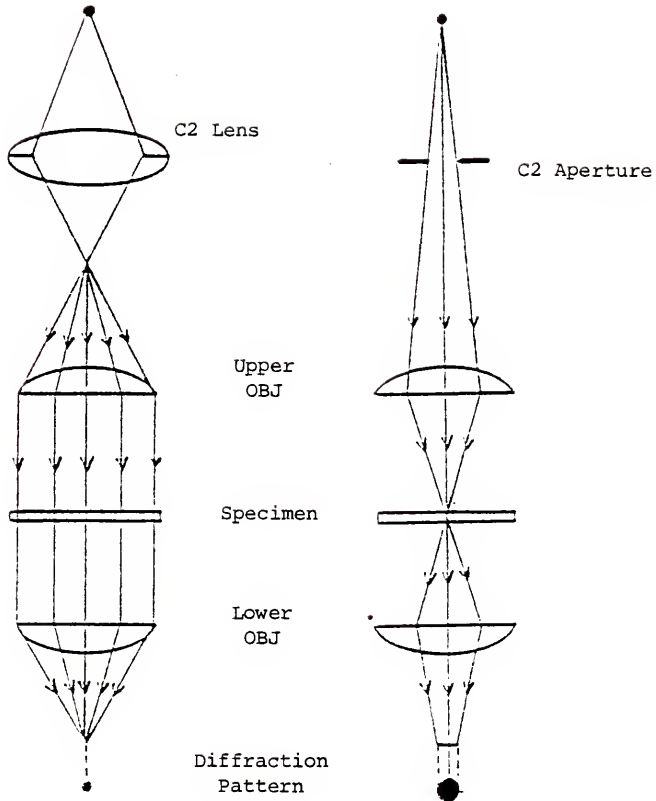


Figure 2.1 Ray diagrams for TEM and STEM conditions in the Philips 301. In STEM, the convergence of the beam is controlled by the second condenser aperture diameter, while the upper half of the objective lens focuses the probe onto the specimen. In TEM, the second condenser lens offers an additional control of convergence.

The effect of the large difference in beam convergence on electron diffraction for STEM and TEM can be shown with the reciprocal lattice construction. Elastic scattering of electrons in the reciprocal space is diagrammed in Fig. 2.2 where a vector \vec{P}_t is drawn parallel to the transmitted electron beam and a number of vectors \vec{P}_s are drawn parallel to the scattered beams. The magnitude of the transmitted vector is defined as $\frac{1}{\lambda}$. Because scattering is assumed to be elastic, the wavelength of the electrons does not change upon diffraction and $\lambda_T = \lambda_S$. Inspection of Fig. 2.2a shows that the tips of all possible scattering vectors trace out a surface called the reflecting, or Ewald, sphere.

The Laue conditions show that diffraction occurs only when the reflecting sphere intercepts a point in the reciprocal lattice that corresponds to a particular diffracting plane. This is written algebraically as

$$\frac{(\vec{P}_t - \vec{P}_s)}{\lambda} = \vec{g}_{hkl} \quad (2.1)$$

where \vec{g}_{hkl} is a vector drawn from the origin of the reciprocal lattice to any point hkl that represents the set of hkl diffracting planes.

For 100 KV, $\frac{1}{\lambda} = 27 \text{ \AA}^{-1}$ units while $|g_{111}|$ for Si = $.32 \text{ \AA}^{-1}$. Thus, for low index lattice planes, the radius of the reflecting sphere is 25 to 85 times greater than the spacing between the reciprocal lattice. Even for these conditions, diffraction would rarely occur since the reciprocal lattice points for a perfect crystal of infinite size are considered to be dimensionless. However, if the

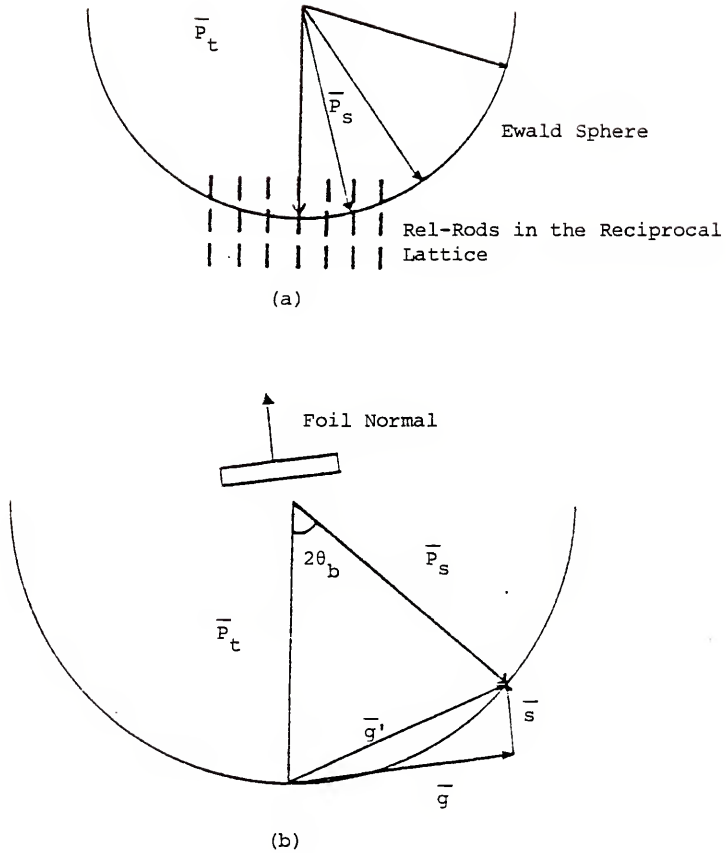


Figure 2.2. Reciprocal lattice diagram (a) showing that the reflecting sphere must intersect a rel-rod if the corresponding diffractive spot is to appear in the diffraction pattern. The Bragg deviation is defined in (b) as a vector drawn from the center of the rel-rod to its intersection with the reflecting sphere.

total diffracted intensity is computed for only a finite number of unit cells, structure factor arguments (Edington, 1975) show the reciprocal lattice points can now be represented as a volume of dimensions $\frac{2}{N_x}$, $\frac{2}{N_y}$ and $\frac{2}{N_z}$ where z is the specimen foil normal and N is the number of unit cells along a particular direction. For typical foil thicknesses, the dimension N_z is much less than N_x or N_y so the reciprocal lattice points are stretched into rods whose long axis is parallel to the foil normal of the specimen. As shown in Fig. 2.2a, the reflecting sphere can now intersect many of the elongated lattice points forming an electron diffraction pattern with numerous higher order diffraction spots.

The distance between the diffraction vector and the reciprocal lattice point center is defined by the vector \bar{s} , which shows the direction and magnitude of the deviation from the exact Bragg condition. In Fig. 2.2b, \bar{s} is drawn parallel to the foil normal from the reciprocal lattice center to the intersection point with the reflecting sphere. By convention, the positive direction of \bar{s} is defined as anti-parallel to the electron beam direction.

2.2 A Review of the Dynamical Theory of Electron Diffraction

STEM's effect on the formation of the diffraction contrast image can be understood if the Howie-Whelan dynamical theory is modified to account for convergent beam radiation (Whelan and Hirsch, 1957).

To review, the dynamical theory states that the transmitted and scattered waves resulting from electron diffraction can no longer be treated independently. Now the scattered wave is considered to be

continually rescattered back in the original direction of the transmitted beam as shown in Fig. 2.3. The transmitted and the scattered wave will interfere and the amplitudes, T and S , of the waves will oscillate with the penetration depth, z , into the crystal. This interaction is described by two, simultaneous linear differential equations:

$$\frac{dT}{dz} = -\eta T + (i - A)S$$

$$\frac{dS}{dz} = (i - A)T + (-\eta + 2is\xi_g + 2\pi i\beta)S$$

The complete derivation of the equations, based on a quantum mechanical approach is discussed by Hirsch et al. (1965). In this chapter, it will be sufficient to explain the effects of the various terms on the transmitted and scattered intensities $|T|^2$ and $|S|^2$, since this is the primary type of information available in the STEM microdiffraction patterns.

Ordinary absorption that controls the absolute intensities of the transmitted and scattered beams is defined as η . This "normal" absorption simply lessens the intensity of both transmitted and scattered beams for crystalline sections of increasingly greater thickness. The absorption effect is thought to result from the inelastic, or high-angle, scattering of electrons since actual absorption of electrons does not occur (Hirsch, 1965).

The anomalous absorption parameter, A , would actually be better described as "enhanced transmission" of the beam at certain positive deviations from the exact Bragg angle. A complete explanation of why the enhanced transmission phenomenon occurs can be made

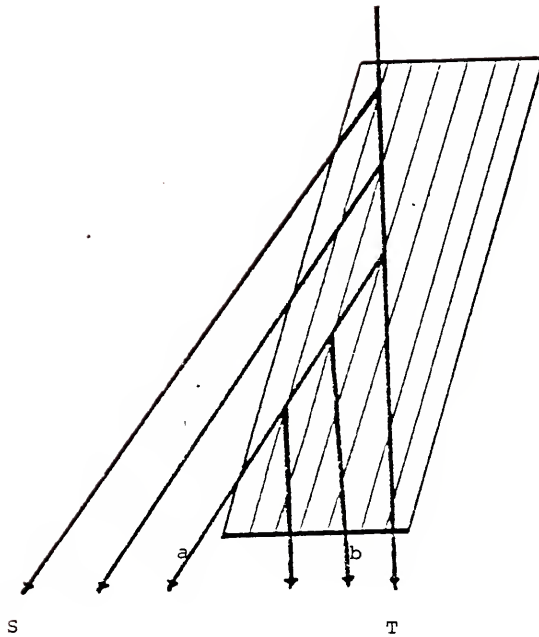


Figure 2.3 The multiple scattering assumption of the dynamic theory. Ray "a," elastically scattered in direction S, can undergo additional elastic scattering to be rescattered in direction T, the original beam direction.

only with extended reference to the derivation of the dynamical theory. In brief, one of the standing Bloch waves contributing to the solution distributes electronic charge in between the ion cores. Such a wave has lower average potential energy than a Bloch wave which distributes charge close to the ion cores and enhances the transmission of electrons through the lattice.

The variable ξ_g , or extinction distance, is the depth of the crystal necessary for either T or S to increase to their maximum amplitude and then decay to their minimum value. Thus, the wavelength of both T and S is $2\xi_g$. The extinction distance increases with increasing Bragg deviations, so the "effective" extinction distance is usually written as $W = \xi_g s$ (Hirsch et al., 1965).

The parameter describing the effect of a defect strain field, β , is written as

$$\beta = \frac{d}{dz} (\bar{g} \cdot \bar{R}) \xi_g \quad (2.3)$$

β describes the relative amount of lattice distortion produced by a defect displacement field, \bar{R} . The magnitude of strain, $\bar{g} \cdot \frac{d\bar{R}}{dz}$, changes the effective value of s and thus plays a primary role in determining the diffraction contrast image resulting from the defect.

The two-beam equations depend upon two important assumptions, both of which may have to be modified for the convergent beam STEM case. First, the two-beam assumption itself is strictly valid only for a completely collimated electron beam and crystals that are several extinction distances thick. For these conditions, a "thin-walled" Ewald sphere can be oriented such that it intercepts only one

rel- rod that has a relatively short reciprocal length. For increasingly convergent beam radiation or for acceleration voltages much greater than 100 KV, additional scattered beams will tend to be excited and each additional excited beam results in an additional differential equation.

Second, the assumption that T and S vary significantly only in the z direction, such that $\frac{\partial T}{\partial x} = \frac{\partial T}{\partial y} = \frac{\partial S}{\partial x} = \frac{\partial S}{\partial y} = 0$, known as the column approximation (Howie and Basinski, 1968), is less valid for STEM. Here, interactions between the transmitted and scattered electron waves are considered to be confined to a narrow column parallel to the incident electron beam. Interactions between electrons in adjacent columns are considered to be negligible. However, this is strictly true only if θ_B is small and the beam is well collimated.

While θ_B does not change for STEM, the incident beam is now spread over a range of directions and it would seem that differentiation should take place along all possible electron beam directions contained in the convergent beam cone.

These effects will be discussed further in the next section. At this point, it is helpful to solve the two-beam equation for the perfect crystal case and illustrate the effects of varying the anomalous absorption and the Bragg deviation. Since β now equals zero, the equations become

$$\frac{dT}{dz} = -\pi\eta T + \pi(i - A)S \quad (2.4)$$

$$\frac{dS}{dz} = \pi(i - A)T + [-\pi\eta + 2\pi i(w + \xi_g)]S$$

Only for the perfect crystal can the equations be solved analytically. After some manipulation the solution for the transmitted amplitude is

$$T = - \frac{\gamma_2 + \pi\eta}{\gamma_1 - \gamma_2} \exp(\gamma_1 z) + \frac{\gamma_1 + \pi\eta}{\gamma_1 - \gamma_2} \exp(\gamma_2 z) \quad (2.5)$$

where

$$\gamma_{1,2} = -\pi\eta + i\pi[w \pm \sqrt{w^2 + (i - A)^2}] \quad (2.6)$$

The amplitude of T thus oscillates not only with depth z but also the Bragg deviation. This is shown in Fig. 2.4 where $|T|^2$ is plotted versus s to form the rocking curve. The rocking curve has a maximum at $s = 0$ only when A is set equal to 0. Experimental evidence (Head et al., 1973) shows the proper value of A to vary between 0.07 and 0.13 according to the Bragg reflection used to form the scattered wave. The rocking curve closely resembles the contrast seen at a bend contour, where a section of a thin foil bent at a constant radius results in a constant change in s . Since bend contours can be observed in both TEM and STEM, the experimental images offer a good test of numerical calculations.

The variation of $|T|^2$ with z is shown in Fig. 2.5 where the period is $2\xi_g$ and the A/N ratio is clearly revealed as an attenuating effect to the wave. T and S are always 180° out of phase, thus explaining the contrast reversal seen in bright and dark-field images. This example also correctly predicts the presence of thickness fringes

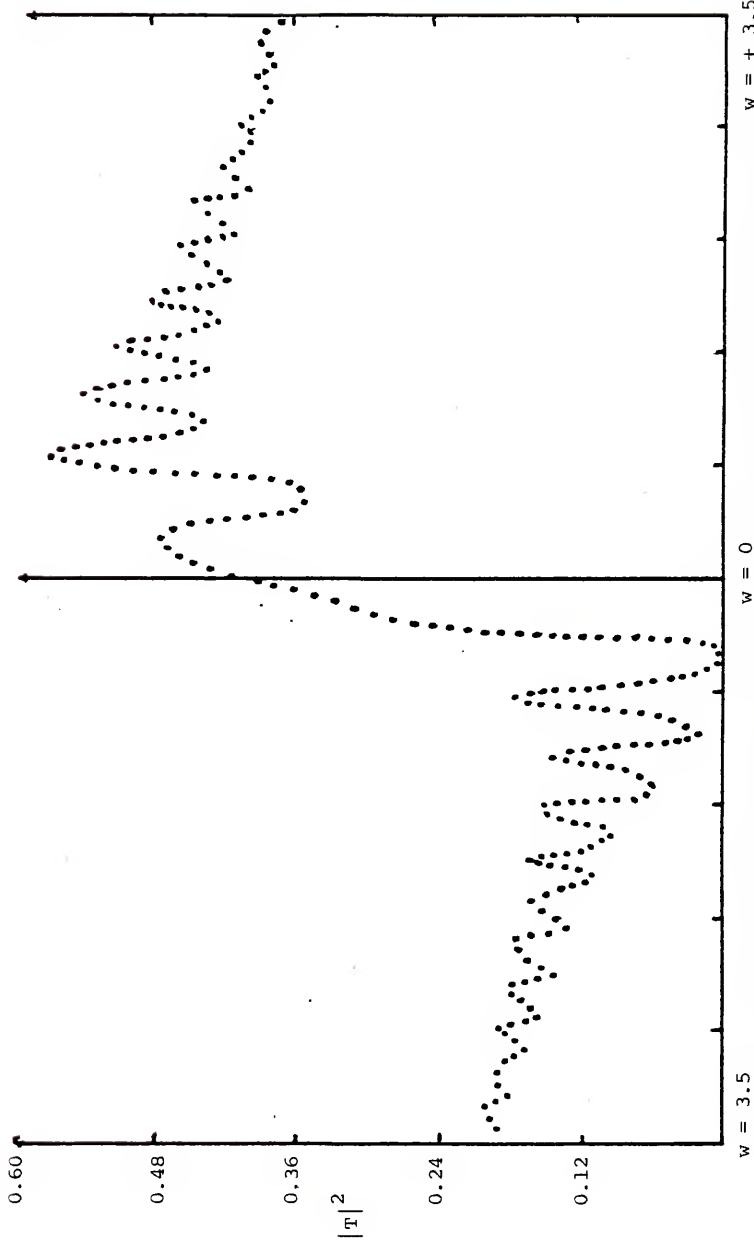


Figure 2.4 Rocking Curve for $|T|^2$ as a function of s . The curve is symmetrical about $s = 0$ only if $A = 0$. Increasing values of anomalous absorption shift the maximum of the curve to positive s values.

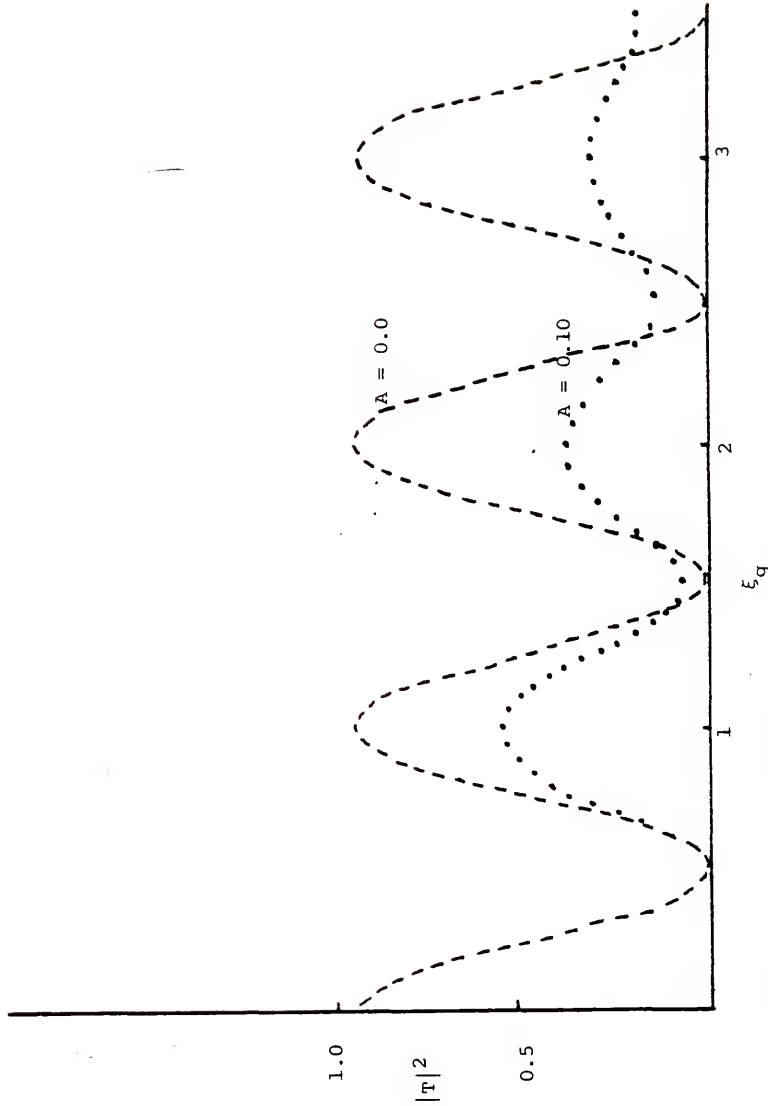


Figure 2.5 Intensity curves for T and S as a function of z and anomalous absorption. Higher A values damp out the oscillations of $|T|^2$ which are seen experimentally as thickness fringes. Higher values of normal absorption, η , cause the curve to decrease to some fixed, but non-zero value.

commonly seen in a wedge-shaped foil. Convergent beam radiation will again affect the shape of these curves and will be discussed in the next section.

2.3 The Effect of STEM on the Reciprocal Lattice Construction

The strongly convergent STEM beam must be represented as a volume in reciprocal space rather than a simple spherical surface. This volume is constructed geometrically from Fig. 2.6a, where the electron beam for STEM is represented by a cone-shaped bundle of rays. Each ray corresponds to a particular \bar{P}_t direction in reciprocal space with its associated reflecting sphere. Addition of all of the possible reflecting spheres forms a "reflecting volume" (Fig. 2.6b) with a node at the origin of the reciprocal lattice. This volume could also be formed by rocking the reflecting sphere for the TEM case through all possible angles, α_i are 5×10^{-4} rad in TEM, and 5×10^{-3} to 10^{-2} rad in STEM.

It is apparent from Fig. 2.6b that the STEM convergent beam alters the diffracting conditions in two ways. First, the Laue diffraction equation becomes increasingly relaxed for higher order spots as the rel-rods are more likely to be situated inside the reflecting volume at greater distances from the reciprocal lattice origin. Second, the deviation from the exact Bragg condition for a particular diffraction spot can no longer be assigned a specific value. It now corresponds to a range of values determined by the portion of the rel-rod's length that lies inside the reflecting volume.

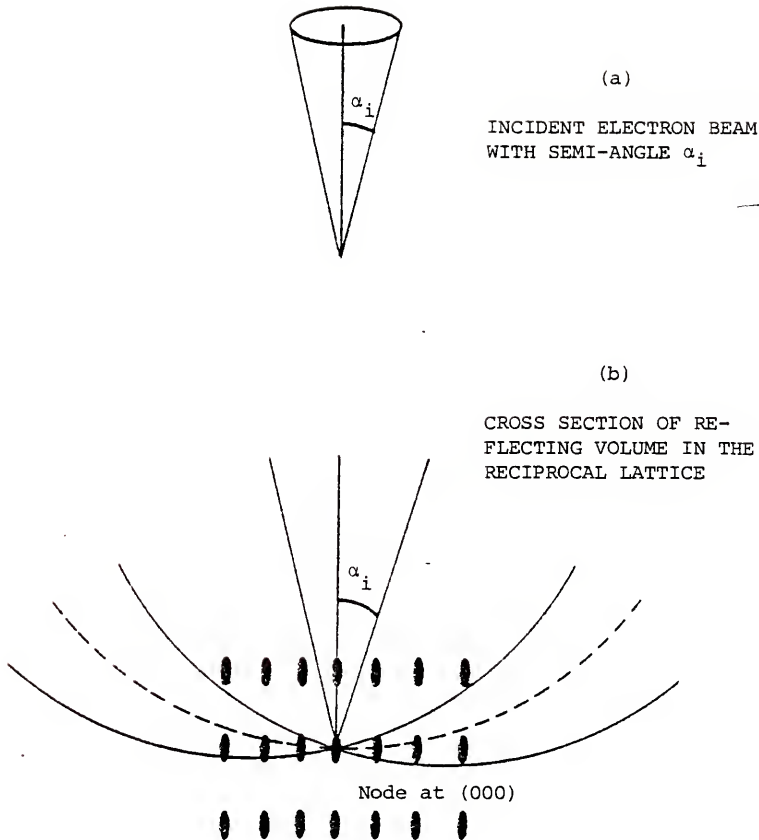


Figure 2.6 Cross section of the reflecting volume for a convergent beam of semi-angle α_i shown in (a). The reflecting volume gradually increases in thickness at greater distances from the reciprocal lattice origin.

Analytical geometry can be used to describe the reflecting volume for the convergent beam case and provides quantitative estimates of both these effects. To begin, the central beam direction, \bar{B} , is defined as parallel to the optic axis and is drawn from the origin of the reciprocal lattice anti-parallel to the electron beam. We then define the set of all vectors lying on the surface of the convergent beam cone at angle α_i away from \bar{B} as \bar{B}' . Since both \bar{B} and \bar{B}' are equal to $\frac{1}{\lambda}$, it follows that

$$\bar{B}' \cdot \bar{B} = \frac{\cos \alpha_i}{\lambda^2} \quad (2.7)$$

$$|\bar{B}'| = |\bar{B}|$$

Any vector \bar{B}' satisfying these conditions can act as radius for its associated reflecting sphere. The equation for each of the reflecting spheres is

$$(x - B'_1)^2 + (y - B'_2)^2 + (z - B'_3)^2 = \frac{1}{\lambda^2} \quad (2.8)$$

Once an initial \bar{B}' is chosen, additional radii may be computed by specifying that each vector on the cone lies ϕ degrees away from its neighbor. These additional vectors, \bar{B}'' , are found by solving the simultaneous equations

$$\bar{B}'' \cdot \bar{B}' = \frac{\cos \phi}{\lambda^2}$$

$$\bar{B}'' \cdot \bar{B} = \frac{\cos \alpha_i}{\lambda^2} \quad (2.9)$$

$$|\bar{B}''| = \frac{1}{\lambda}$$

Each \bar{B}'' , when substituted into Eq. 2.8, defines a segment of the outer surface of the reflecting volume for angle ϕ . The equation defining both the upper and lower surfaces of the reflecting volume is then

$$(x \pm B_1'')^2 + (y \pm B_2'')^2 + (z \pm B_3'')^2 = \frac{1}{\lambda^2} \quad (2.10)$$

Satisfaction of Bragg condition for any given reciprocal lattice point can now be checked by substituting its coordinates into x , y , and z of Eqn. 2.10 and solving for a given set of \bar{B}'' .

However, it has been shown that any reciprocal lattice point is stretched out to a rod parallel to the foil normal. For the convergent beam case, it is necessary to compute the ranges of s values for a particular operating reflection. If the rel-rod is arbitrarily divided into ten segments, the location of each segment in the reciprocal lattice is given by

$$\bar{g}' = \bar{g} + \bar{s} \quad (2.11)$$

where \bar{s} is a vector parallel to the foil normal

$$\bar{s} = \frac{2}{N_z} \left(\frac{\bar{FN}}{|\bar{FN}|} \right) \cdot n \quad (-5 \leq n \leq 5) \quad (2.12)$$

Each rel-rod segment, defined by \bar{g}' , can now be checked with Eqn. 2.10 to tell whether it lies within the upper and lower surfaces of the reflecting volume.

2.4 The Effect of STEM on the Dynamical Theory

The dynamic theory must be modified to take the convergent electron beam used in STEM into account. Section 2.3 has already shown that the reflecting sphere shape must be modified to account for convergent radiation. As was shown in Fig. 2.6b, the diffraction excitation rules are relaxed for higher order reflections and thus the two-beam conditions should be more difficult to achieve for STEM. Of greater importance is the fact that even if two-beam conditions are achieved, the Bragg deviation is now spread over a range of values. Since the Howie-Whelan two-beam equations depend directly on s it can be seen immediately that both the rocking curve for $|T|^2$ and the curve for $|T|^2$ versus z will be modified for STEM.

For purposes of illustration, it is best to use a non-column-approximation set of two-beam equations, and see how beam convergence relates to the various terms. The work of Howie and Basinski shows that

$$\frac{\partial T}{\partial z} + \gamma_z \frac{\partial T}{\partial z} + \gamma_y \frac{\partial T}{\partial y} = \frac{\pi i}{\xi_0} T + \frac{\pi i}{\xi_g} \exp[2\pi i (sz + \bar{g} \cdot \bar{R})] S \quad (2.13)$$

$$\frac{\partial T}{\partial z} + \gamma_x \frac{\partial T}{\partial x} + \gamma_y \frac{\partial T}{\partial y} = \frac{\pi i}{\xi_0} T \exp[-2\pi i (sz + \bar{g} \cdot \bar{R})] + \frac{\pi i}{\xi_0} S$$

where

$$\gamma_x = \frac{(\bar{p}_t + \bar{g})_x}{(\bar{p}_t + \bar{g} + \bar{s})_z} \quad \gamma_y = \frac{(\bar{p}_t + \bar{g})_y}{(\bar{p}_t + \bar{g} + \bar{s})_z} \quad (2.14)$$

and the subscripts refer to the components of the vector sums for the x, y, and z directions.

For the Bragg angles encountered in electron diffraction, $(P_t + g)_x$ or $y \ll (\bar{P}_t + \bar{g} + \bar{s})_z$ and the variation of s with respect to the x or y directions can be ignored. In STEM, θ_B remains the same so this inequality should still hold. However, by Fig. 2.6b, \bar{P}_t now has a range of directions determined by α_i , the angle of incidence. Thus, for STEM, it is no longer a good approximation to differentiate in the z direction parallel to the optic axis of the microscope, and the two-beam equations must be solved repeatedly for a range of specific propagation directions determined by α_i . For each propagation direction, however, the terms γ_x and γ_y are no larger than before and thus the form of the equations remains unchanged.

For the beam convergences generally used in STEM crystal defect images, α_i is still only a fraction of the Bragg angle, and it is evident that varying s, the Bragg deviation, gives results equivalent to those obtained from differentiating over the range of propagation directions.

For STEM conditions, the only necessary change in the two-beam equations is to replace T and S by T_n and S_n .

$$\frac{dT_n}{dz} = -\pi\eta T_n + (i - A)S_n \quad (2.15)$$

$$\frac{dS_n}{dz} = \pi(i - A)T_n + [-\pi\eta + 2\pi i(w_n + \xi_g \beta)]S_n$$

where n indicates the equations must be solved repeatedly for n values of $w + \Delta w$. The Bright-field intensity is then

$$|T_{STEM}|^2 = \sum_n |T_n|^2 \quad (2.16)$$

In experimental practice, an additional control on the form of the STEM image is α_o , the angle subtended by the STEM detector. In the Philips 301 microscope, α_o can be varied either with the final projector lens or by using the objective aperture to block part of the beam from striking the detector. In both cases reducing α_o means that rays from only the central portion of the incident beam are used to form the image and the convergence can be equivalent to one where α_i was reduced instead.

Since α_o offers the last opportunity in the column to control the convergence of the beam, Maher and Joy (1976) have defined the equation

$$\Delta w = |g| \xi_g \alpha_o \quad (2.17)$$

where Δw shows the extent of the variation from ideal TEM imaging with a perfectly collimated beam. As shown in Fig. 2.7, the range of Bragg deviations is proportional to α_i and thus also to α_o for the reasons outlined above.

The equation for Δw shows directly which electron optical conditions and which materials will show the greatest amount of image modification under STEM imaging conditions. As discussed by Booker et al. (1974), higher order reflections for STEM imaging produce situations where the variation in the Bragg deviation range increases due

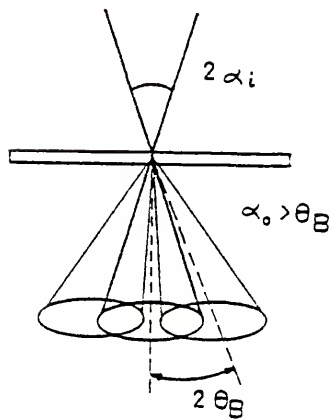
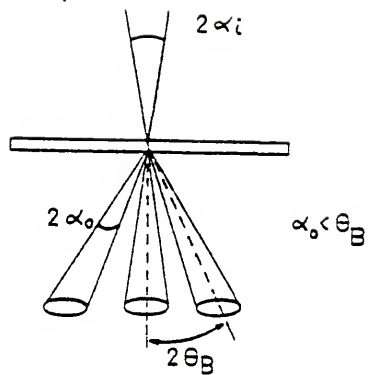


Figure 2.7 Beam convergence values for low cone angle STEM (a) and MBI (b).

to the greater thickness of the convergent beam reflecting volume. Low atomic number materials with relatively longer extinction distances for a particular reflecting plane will also tend to show greater Δw values. For example, at 100 KV and $\alpha_i \approx 5 \times 10^{-3}$, $\Delta w = .97$ for silicon but only .58 for Cu due to their different values for ξ_{111} and d_{111} .

The Δw relation can be used only in "low-cone angle" STEM where $\alpha_i < \theta_B$. If this condition is not satisfied, the first order diffraction cones overlap the central beam as shown in Fig. 2.7b and it may be physically impossible to place the detector such that it is struck by only one beam. This case, known as Multi-Beam Imaging (MBI) was studied by Reimer (1976). As might be expected, in a case where both bright-field and dark-field images are used to simultaneously form an image, crystal defect contrast is reduced but it also decreases rapidly with foil depth. Except for this feature, which allows easy determination of which end of a defect penetrates the top of the foil, MBI offers no advantage over standard TEM or low-cone angle STEM techniques.

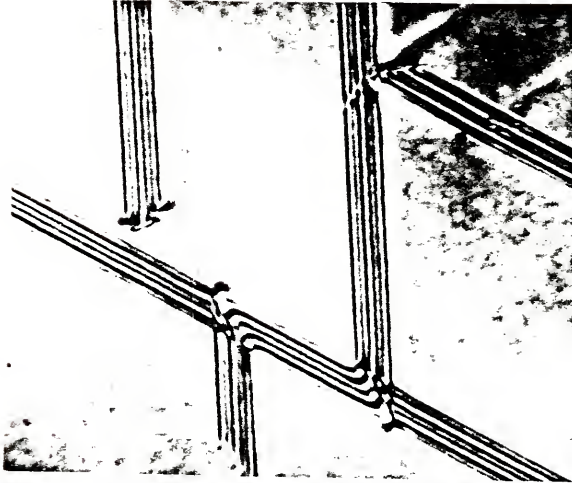
Reimer attempted to compare calculated profiles of stacking faults with experimental MBI images and obtained reasonable agreement by assuming a non-coherent source. If some degree of coherence of the incident electron beam is assumed, it is apparent from Fig. 2.7b that the primary transmitted and scattered waves could interact even if the multiple scattering phenomena used in the development of the dynamic theory are ignored. This does not occur with a standard hairpin filament because the tip of the filament from which electrons

are emitted is approximately 15 μm in diameter and the 100 KV electron wavelength is only .037 \AA . For a much smaller source size, such as the field emission STEM, the dynamic theory may have to be modified to take increased coherence into account.

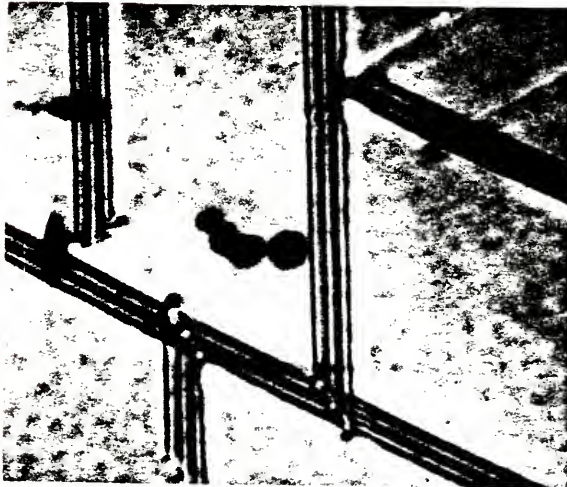
If imaging is restricted to low-cone angle STEM, the Δw equation provides a good indication of the extent of image modification. Joy and Maher (1975) examined bend contours in silicon for a range of $\alpha_0 = 7.5 \times 10^{-3}$ rad to 3×10^{-7} rad for the $\langle 220 \rangle$ reflection ($\theta_B = 10^{-2}$ rad) and found that alterations in fringe contrast that became negligible once α_0 was less than 8×10^{-4} rad. Thus, if $\Delta w < 0.1$, the STEM image should be virtually identical to conventional TEM. These conditions can be easily satisfied in the Philips 301 and Fig. 2.8 shows experimental confirmation of Joy and Maher's results comparing a well collimated ($\alpha_0 = 5 \times 10^{-4}$ rad) TEM image to that of STEM ($\alpha_0 = 1 \times 10^{-3}$ rad) with $g = \langle 220 \rangle$ for an extrinsic stacking fault in silicon.

Stacking faults and dislocation images are less susceptible to convergent beam imaging modification than bend contours or thickness fringes. Apparently, this occurs because defect displacement fields strongly affect transmitted and scattered beams only in a localized area, while a bent foil supplies a more gradual, but constant, modification to the beam amplitude along the entire column. Since these features often obscure contrast from defects, STEM imaging with $\Delta w \approx 1.0$ may prove to be more advantageous than TEM in highly deformed specimens.

As explained in the last section, a bent foil of constant radius produces an intensity curve quite similar to the rocking curves in



(a) TEM



(b) STEM

Figure 2.8 Extrinsic stacking faults in silicon imaged for two-beam conditions in TEM with $\alpha_0 = 5 \times 10^{-4}$ rad (a) and in STEM with $\alpha_0 = 1 \times 10^{-3}$ (b).

Fig. 2.4 that plot T^2 versus w . STEM conditions force the replacement of TEM rocking curve by a family of curves each slightly displaced along the w axis up to an amount $\frac{\Delta w}{2}$. Figure 2.9 shows the results for both 4 and 6 curves that are added together and then normalized to produce the "STEM" rocking curve. As implied by Fig. 2.9, further summations beyond 4 curves improve the accuracy by only a small amount. The same procedure is used to produce the thickness fringe curve in Fig. 2.10, where curves are plotted for different values of s and then averaged to produce the STEM version of the $|T|^2$ as a function of thickness curve.

In each case, the "square aperture approximation" developed by Fraser et al. (1976) is used for computation. Here, the convergent beam diffraction pattern is approximated by a square array (Fig. 2.11) and the range of Δw is determined by the distance of the centroid of the square to the appropriate Kikuchi line.

2.5 A STEM Computer Simulation Program

Since a crystal defect image is simply a greatly magnified image of the main beam or one of the diffraction spots, it follows that a microdiffraction pattern from the vicinity of the defect can contain no more information than the defect image itself. However, it will be shown in subsequent chapters that if α_i and the spot size are kept sufficiently small, it is possible to directly obtain intensity information such as $|T|^2$ or $|S|^2$ for a two-beam condition from an area as small as 50 \AA in diameter.

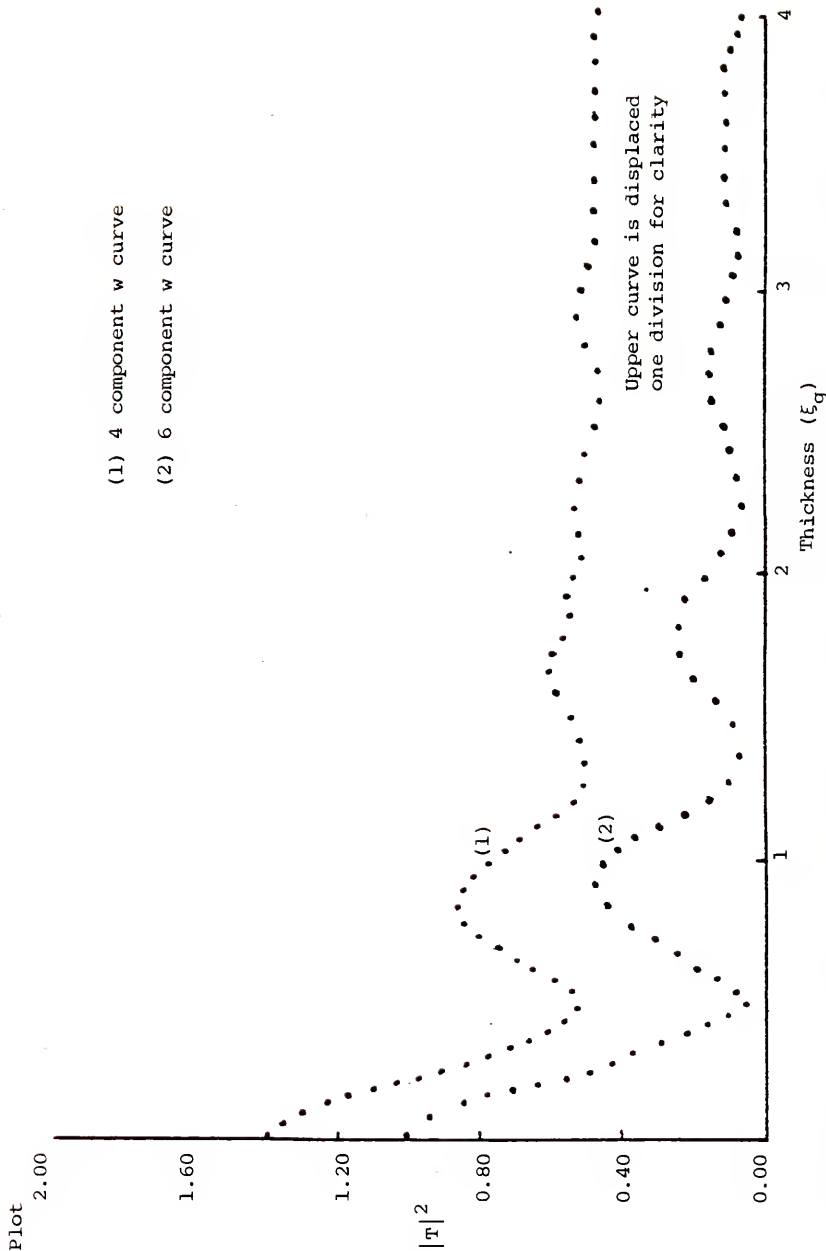


Figure 2.9 The effect of convergent beam radiation on a thickness fringe curve shown in Fig. 2.6. For the curves, $\alpha_i = 5 \times 10^{-3}$ rad, $\bar{g} = 220$, and $A = 0.10$. The separation of w into six different values is sufficient to approximate STEM conditions.

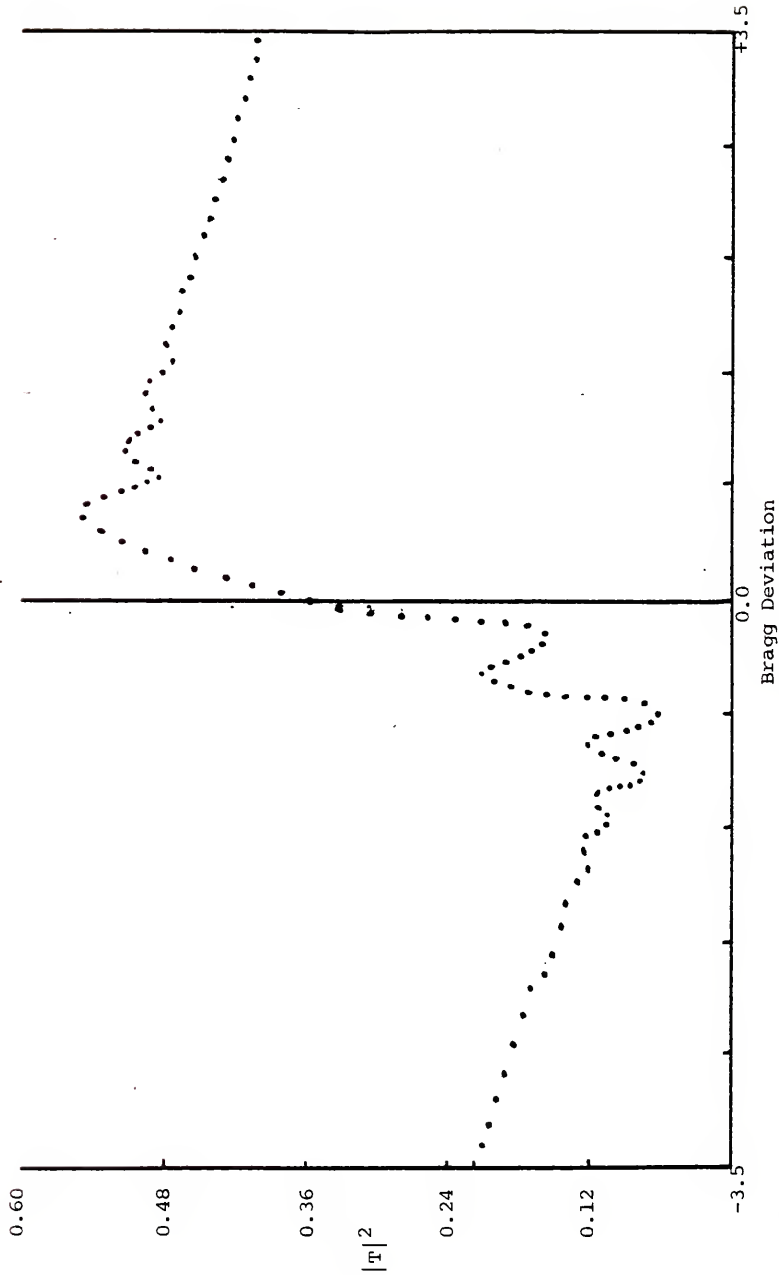


Figure 2.10 Rocking curves for convergent beam radiation with $A = 0.10$ and $\alpha_i = 5 \times 10^{-3}$. As in Fig. 2.9, the convergent beam reduces the amplitudes of the oscillations in the curve.

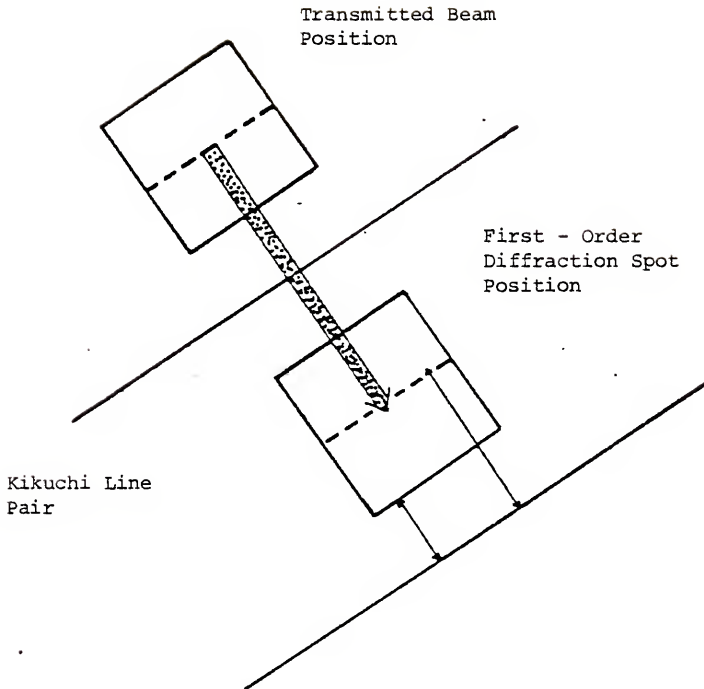


Figure 2.11 The square aperture approximation (after Fraser) used to compute Fig. 2.9 and 2.10. The maximum and minimum w values are found by measuring the distance from the "diffraction square" center to the appropriate Kikuchi line. Any given w value does not vary in the x direction. This would not be the case for a circular aperture that would produce a circular diffraction disc.

The microdiffraction pattern provides, in one image, the direct $|T|^2/|S|^2$ intensity ratio (measured experimentally by a densitometer from the photographic plate) that could be obtained only by measuring intensities at exactly the same point in the bright-field and dark-field defect images. Since after tilting the beam to get a dark-field image it is impossible to keep the Bragg deviation precisely the same, obtaining $|T|^2/|S|^2$ ratio is possible only with microdiffraction. If the location of the incident beam can be precisely determined, experimental $|T|^2/|S|^2$ ratios can then be "simulated" by mathematically modeling the effect of the defect strain field, \bar{R} , on the T-S interaction. The various experimental variables such as foil thickness or the Burgers vector can then be varied until the computed ratios are the same as the experimental model. This approach has been developed by Head et al. (1973) by matching defect images to a high degree. The microdiffraction ratio method potentially offers a method of characterizing the defect strain field with a much smaller expenditure of computer time than the image matching method, where several thousand columns must be computed to produce a simulated image.

A program to simulate $|T|^2/|S|^2$ ratios need not be as efficient as the one used by Head, since only a few columns should need to be computed before the defect is identified. While the approach used here was chosen for algebraic simplicity, it is sufficiently rapid that it can be used to produce defect image simulations if desired.

Reference to Fig. 2.12 shows the two coordinate systems required for the intensity calculations. The first, crystal coordinates, is used because necessary input data such as dislocation line direction,

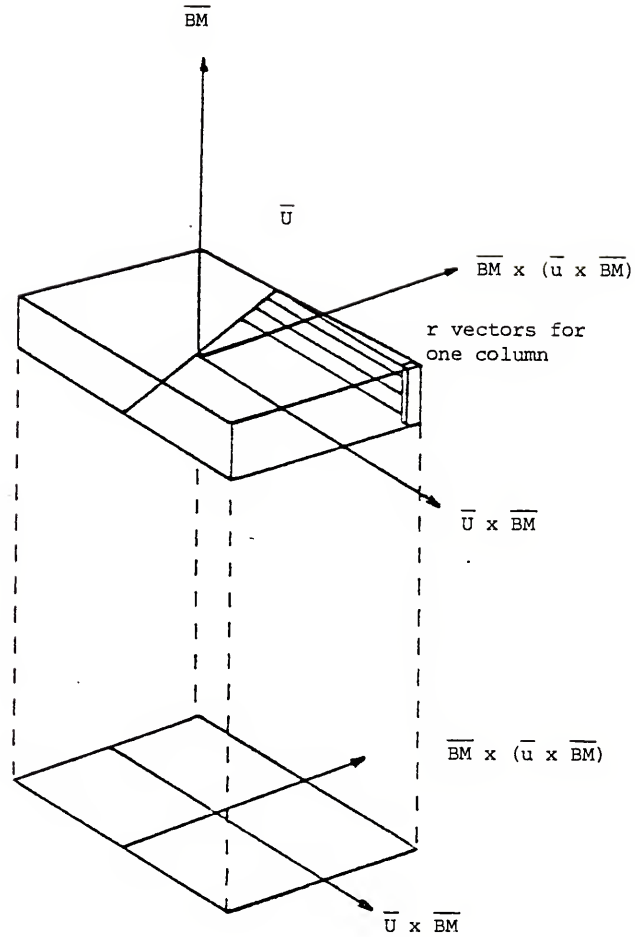


Figure 2.12 Coordinate system in relation to dislocation and the image plane.

foil normal and the \bar{g} vector can be determined only by using the hkl coordinates found in the diffraction patterns. The second, image plane coordinates, are used to determine, \bar{R} , the displacement field values necessary to solve the two-beam equations for a particular column.

Once the necessary geometry transformations have been determined, the intensity calculation is relatively simple. Each column, parallel to the electron beam direction, is divided into a number of segments, dz , and \bar{R} , the defect displacement field, is computed for each segment. Then by using the approach of Thörlén (1970), each column segment is considered to be a slab of perfect crystal rotated a slight amount by the defect displacement field. Each segment can be considered to have a different Bragg deviation, and the analytic solution (Eqn. 2.5) is used to compute T or S for that segment. Thörlén showed how to manipulate the analytic solution such that the amplitude T and S exiting from any random slab are related to the incident amplitude by a 2×2 matrix:

$$\begin{pmatrix} T \\ S \end{pmatrix}_{\text{out}} = \begin{bmatrix} a_{11} & a_{12} \\ a_{21} & a_{22} \end{bmatrix} \begin{pmatrix} T \\ S \end{pmatrix}_{\text{in}} \quad (2.18)$$

where

$$a_{11} = \frac{(\gamma_2 + \pi\eta)}{(\gamma_1 - \gamma_2)} [-\gamma_2 \exp(\gamma_1 dz) + \gamma_1 \exp(\gamma_2 dz)] \quad (2.19)$$

$$a_{12} = a_{21} = \frac{\pi(i - A)}{(\gamma_1 - \gamma_2)} [\exp(\gamma_1 dz) - \exp(\gamma_2 dz)]$$

$$a_{22} = \frac{(\gamma_1 + \pi\eta)}{(\gamma_1 - \gamma_2)} [\gamma_1 \exp(\gamma_1 dz) - \gamma_2 \exp(\gamma_2 dz)]$$

and

$$\gamma_{1,2} = i\pi(w \pm \sqrt{w^2 + (i - A)^2}) \quad (2.20)$$

With this approach, the two-beam equations do not need to be numerically integrated down a column of distorted crystal. Prediction of the amplitudes of T or S is now achieved by matrix multiplication, where each matrix corresponds to a slab of perfect crystal with thickness, dz , and a specific Bragg deviation. After the necessary transformations converting all crystal directions to image plane coordinates, the sequence for the numerical calculations of $|T|^2$ or $|S|^2$ proceeds in the following manner:

First, the distance, r , between the dislocation line and the column segment is determined. The displacement field, \bar{R} , is now a function of r , θ , and \bar{b} , where \bar{b} is the Burgers vector and θ is the angle between r and the slip plane. With r known, compute \bar{R} at the top and bottom of the segment.

It is important to realize that \bar{R} is a function of only two independent variables, r and θ , for any given Burgers vector. Large savings in computer time can result if \bar{R} is pre-computed for a range of r and θ values that correspond in size to an area somewhat larger in diameter than the specimen thickness. By storing $\bar{g} \cdot \bar{R}$ in matrix form, with subscripts corresponding to r and θ , repetitive calculations of the same value of \bar{R} can be greatly reduced. This idea, never used by Thölén, is feasible because the dislocation displacement field is "two-dimensional," i.e., an \bar{R} value for a given r and θ , is the same along any point of the dislocation length, assuming the infinite solution.

When $\overline{g \cdot R}$ has been determined, the effect of the dislocation on each slab, dz , is

$$\beta = \frac{d}{dz} (\overline{g \cdot R}) \xi_g = \frac{g \cdot (\overline{R}_{\text{top}} - \overline{R}_{\text{bottom}})}{z_{\text{top}} - z_{\text{bottom}}} \cdot \xi_g \quad (2.21)$$

Now, the effective Bragg deviation $w + \beta \xi_g$ and a scattering matrix a_{ij} of a specific value are known for the slab. Thörlén has shown that it is possible to pre-compute the scattering matrices for increments of w just as was done for \overline{R} . β can then be used to select the appropriate pre-computed matrix needed for a particular slab. Once a scattering matrix has been selected for every slab in the column, the transmitted amplitude, T , at the top surface is set equal to 1 and $S = 0$. The amplitude of T and S at the bottom surface is then found by successively multiplying each scattering matrix times the exiting amplitude of T and S from the slab immediately above:

$$\begin{pmatrix} T \\ S \end{pmatrix}_{\text{out}} = a_1 a_2 a_3 \dots a_n \begin{pmatrix} T \\ S \end{pmatrix}_{\text{in}} \quad \text{where } a_n = \begin{pmatrix} a_{11} & a_{12} \\ a_{21} & a_{22} \end{pmatrix} \quad (2.22)$$

In practice, it is necessary to divide the foil thickness into 80 segments to compute $|T|^2$ to a sufficient accuracy. Thus, 80 scattering matrices must be multiplied together to compute the $|T|^2$ for a single column. The actual intensity $|T|^2$ of $|S|^2$ can then be divided by the intensity found when r is set to a very large value, or to intensity computed for the perfect crystal where $\overline{R} = 0$.

The geometrical conversions can be much simplified if the analytic geometry formulations for a line and a plane given rectangular coordinates are used. Thus, for vector, \bar{A}

$$\bar{C} = C_x \bar{i} + C_y \bar{j} + C_z \bar{k} \quad (2.23)$$

the equation of a line parallel to the vector is

$$\frac{x - x_o}{C_x} = \frac{y - y_o}{C_y} = \frac{z - z_o}{C_z} \quad (2.24)$$

and the equation of a plane normal to the vector is

$$C_x(x - x_o) + C_y(y - y_o) + C_z(z - z_o) = C \quad (2.25)$$

All important features in Fig. 2.12 such as the foil surfaces, or the dislocation line and column directions, can be represented by one of these equations.

To begin the calculations, it is assumed that all necessary input vectors such as the beam direction, \bar{B} , the foil normal, \bar{F} , and diffracting vector, \bar{g} , and the dislocation line direction, \bar{U} , have been computed from experimental hkl coordinates. The Bragg deviation and the anomalous absorption are entered as dimensionless quantities while the foil thickness is entered in units of ξ_g , the extinction distance. Units for \bar{b} , the Burgers vector, and \bar{g} are not important as all units cancel when $\bar{g} \cdot \bar{b}$ is calculated for a particular slab.

An "image plane" coordinate system can now be defined where the vertical axis is parallel to \bar{B} , and one horizontal axis is parallel

to $\overline{U} \times \overline{BM}$, and the final horizontal axis is parallel to $\overline{BM} \times (\overline{u} \times \overline{BM})$. If the direction cosines between the hkl coordinate system and the image coordinates are computed, a 3 x 3 matrix C_{ij} is defined where

$$C_{ij} = x_i \cdot U_j \quad (2.26)$$

C_{ij} can be used immediately to transform all vectors to picture coordinates

$$U'_i = C_{ij} U_j \quad (2.27)$$

$$B'_i = C_{ij} B_j$$

$$b'_i = C_{ij} b_j$$

$$F'_i = C_{ij} F_j$$

$$g'_i = C_{ij} g_j$$

The dislocation is now situated such that its mid-point lies at the origin of the image coordinate axes. Thus the line equation for the dislocation is

$$\frac{x}{U_x} = \frac{y}{U_y} = \frac{z}{U_z} \quad (2.28)$$

To find equations for the upper and lower foil surfaces, x and y are set equal to 0 and TZ is set equal to $TH/2$, where TZ is the foil thickness in the beam direction. Equation 2.25 is then

$$F_3 \left\{ \frac{TZ}{2} \right\} = D \quad (2.29)$$

Once the constant, D , on the right hand side of the surface normal

equation is known, Eqn. 2.25 can be re-arranged to solve for z , the foil surface height

$$z = \frac{\pi Z}{2} - \frac{F_1 x + F_2 y}{F_3} \quad (2.30)$$

The starting point for any column can now be found by selecting any $x_0 y_0$ point in the image plane and solving Eqn. 2.30 for z_0 . Subsequent column segment coordinates are then x_0 , y_0 , and $z_0 - \Delta z$ where $\Delta z = t/80$.

Once the coordinates for any column segment have been determined, the distance to the dislocation line must be calculated.

To compute \bar{r} , both a plane perpendicular to the dislocation line and passing through the origin and a line parallel to the dislocation must be determined. The vector \bar{r} can then be drawn from the origin to the intersection of the plane and the line. From the definition of the coordinate system, the z component of the dislocation line is zero. Therefore, the equations of a line parallel to the dislocation and a plane perpendicular to the dislocation are

$$u_z y - u_y z = C \quad (\text{line equation}) \quad (2.31)$$

$$u_y y + u_z z = 0 \quad (\text{plane equation}) \quad (2.32)$$

Equations 2.31 and 2.32 can be solved simultaneously to yield finally

$$z = -u_y C = -u_y (u_z y - u_y z) \quad (2.33)$$

$$y = u_z C = u_z (u_z y - u_y z)$$

The vector \bar{r} is of the form:

$$\bar{r} = (x - x_0)\bar{i} + (y - y_0)\bar{j} + (z - z_0)\bar{k} \quad (2.34)$$

but since it is drawn from the origin, the three components of \bar{r} are

$$r_x = x \quad (2.35)$$

$$r_y = u_z(u_2y - u_yz)$$

$$r_z = -u_y(u_2y - u_yz)$$

Now, the general solution for a dislocation of mixed Burgers vector is (Hirth and Loethe, 1968)

$$\bar{R} = \frac{1}{2\pi} \left\{ \bar{b}\theta + \bar{b}_e \frac{\sin 2\theta}{4(1-\nu)} + \bar{b} \times \bar{u} \left(\frac{1-2\nu}{2(1-\nu)} \ln|r| + \frac{\cos 2\theta}{4(1-\nu)} \right) \right\} \quad (2.36)$$

where

\bar{b}_e = the edge component of the Burgers vector normal to \bar{u}

θ = an angle between \bar{r} and the slip plane of the dislocation

ν = Poisson's ratio.

As shown in Fig. 2.13, θ can be found by taking the dot product between \bar{r} and a vector lying at the intersection of the slip plane and the plane normal to the dislocation. The intersection vector is defined as

$$\bar{v} = \frac{\bar{u} \times \bar{b} \times \bar{u}}{|\bar{v}|} \quad (2.37)$$

Thus,

$$\cos\theta = \frac{\bar{v} \cdot \bar{r}}{|\bar{r}|} \quad \text{and} \quad \bar{b}_e = (\bar{b} \cdot \bar{v})\bar{v} \quad (2.38)$$

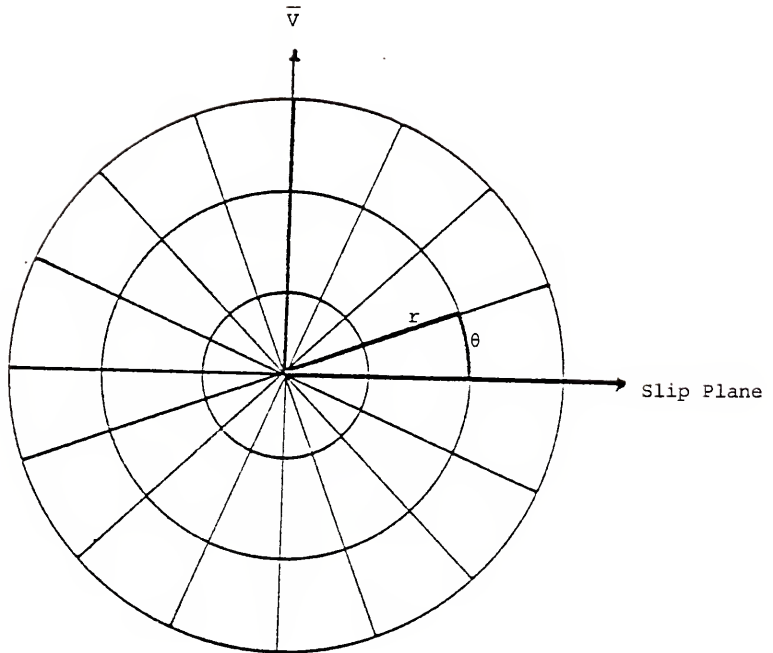


Figure 2.13 Radial coordinate system used for the calculation of \bar{R} at point defined by r and θ . The angle θ is always measured from the slip plane and varies 0 to 2π .

where \bar{V} is a unit vector. Examination of Fig. 2.13, however, shows that θ , computed from Eqn. 2.37, could result from an \bar{r} lying either above or below the slip plane. An additional test to determine the correct direction of \bar{r} is performed by computing the unit vector

$$\bar{P} = \frac{\bar{V} \times \bar{u}}{|\bar{P}|} \quad (2.39)$$

and then again computing the angle between \bar{P} and \bar{r}

$$\cos\delta = \bar{P} \cdot \bar{r} / |\bar{r}| \quad (2.40)$$

By examining the two-dimensional coordinate system formed by \bar{P} and \bar{V} , it is seen that if the true position of \bar{r} is in quadrant I, both $\cos\theta$ and $\cos\delta$ will be positive. If \bar{r} lies in quadrant IV, $\cos\theta$ will be positive, but δ is now more than 90° and $\cos\delta$ will be negative. If a similar test is applied for an \bar{r} lying in each quadrant, it is found that Eqn. 2.37 gives the proper value for θ only when $\cos\delta$ is positive. The computer program calculates both θ and δ and changes θ to $2\pi + \theta$, if $\cos\delta$ is negative. Then the "sense" of θ is always correct, regardless of the position of \bar{r} . \bar{R} can now be computed for every element in the column by the method discussed before.

It is noteworthy that the linear distance between each precomputed matrix element for \bar{R} will vary slightly according to the distance from the dislocation core as shown in Fig. 3.13. This is simply a consequence of defining \bar{R} in terms of polar coordinates. Such a choice is convenient for the column calculation, because the r, θ matrix elements are packed most densely at the dislocation core,

which is precisely where \bar{R} varies most rapidly and the greatest accuracy is needed in the column calculation. With \bar{R} chosen, the effective Bragg deviation for each segment, β , is now calculated

$$\beta = \frac{d}{dz} (\bar{g} \cdot \bar{R}) = \frac{\bar{g} \cdot (\bar{R}_{\text{top}} - \bar{R}_{\text{bottom}})}{\Delta z} \quad \text{where } \Delta z = \frac{TZ}{80} \quad (2.41)$$

As discussed by Thörlén, since the A matrix depends only on w , it is far more efficient in terms of computer time to calculate \bar{a} for incremental values of w and store the results. Since $|w|$ values higher than 3.5 imply such a large lattice distortion that the two-beam condition is no longer valid, the A matrix is calculated for a range of $-3.5 < w < 3.5$ in increments of .005 giving a total of 1401 2×2 matrices that must be stored and used as a "library" when any column is computed. Once the effective Bragg deviation is calculated, it can be converted to an integer by the formula

$$B = \left(\frac{\beta}{.005} \right) \times 700 \quad (2.42)$$

and the integer (from 1 to 80) is used to select the appropriate matrix for a particular slab. The sequence of the column calculation is then

$$\begin{pmatrix} T \\ S \end{pmatrix} = \bar{a}_1 \bar{a}_2 \dots \bar{a}_n \begin{pmatrix} 1 \\ 0 \end{pmatrix} \quad (2.43)$$

where 1, 2...n represents a sequence of 80 integers corresponding to each of the 80 column segments.

Once computed and divided by the background intensity, $|T|^2$ is compared to a series of 11 decimal values between 0 and 1 that comprise

the grey scale used in printing the picture. The value closest to $|T|^2$ is used by the program to select one of 11 symbols that represent a particular shade of grey. This symbol is then printed by an IBM high speed printer to represent the intensity in the micrograph corresponding to a particular column in the specimen. If an image is not desired, ratios of $|S|^2/|T|^2$ for any regular array of columns spaced along the dislocation can also be computed.

In this work, experimental studies concentrated on extrinsic stacking faults in silicon. For this case, the displacement vector is confined to the plane of the stacking fault and does not vary with distance as for the dislocation. For this case, $\bar{R} = \frac{1}{3}\langle 111 \rangle$ and is normal to the stacking fault which always lies on $\{111\}$ -type planes.

It is shown by Whelan and Hirsch (1957) that the fault can be considered as a planar boundary separating two perfect crystals. The S wave must be adjusted by a phase factor $\exp(i\alpha)$ as it passes through the fault while the T wave remains unchanged.

The phase angle is computed by the equation:

$$\alpha = 2\pi \bar{g} \cdot \bar{R} \quad (2.44)$$

Therefore, a stacking fault is added to the program simply by locating its height in the specimen for a particular column and adjusting the amplitude of S at that particular point.

Modification of either dislocation or stacking fault images for the effects of beam convergence in STEM is done in the program by adding a value Δw (computed by $\Delta w = |g| \xi_g \alpha_1$) to the Bragg deviation, w , and then completing the column calculation as before. For

greatest accuracy, Δw must be divided into several segments and the column computation performed for a series of $(w + \frac{\Delta w}{n})$ quantities. All of the $|T|^2$ values for each $\frac{\Delta w}{n}$ segment are then summed together to produce the total intensity for a particular column.

CHAPTER 3
MICRODIFFRACTION METHODS

3.1 A Review of the Effect of Inelastic Scattering
on the Diffraction Pattern

In addition to the dynamic effects on diffraction spot intensities, convergent beam radiation also affects inelastic scattering which is the cause Kikuchi lines and transmission channeling patterns. Both of these phenomena can be understood by examining the surface formed by all vectors that are at an angle of θ_B with the reflecting plane. This surface is a cone whose central axis is normal to the plane.

For diffraction resulting from a perfectly collimated beam, only one vector lying on the surface of the cone is necessary to describe the diffraction direction, and, although the actual diameter of the incident and exiting beams may be several microns in diameter, the beam can be focused to a point to form the diffraction pattern in the back focal plane of the objective lens. If the beam is highly convergent, this is no longer the case. Now, only the part of the incident and reflected rays lay on the reflecting cone surface that defines the exact Bragg angle. The extent of the segment of the convergent beam that intersects the reflecting cone is shown in Fig. 3.1 to be

$$D = 2L\alpha_i \quad (3.1)$$

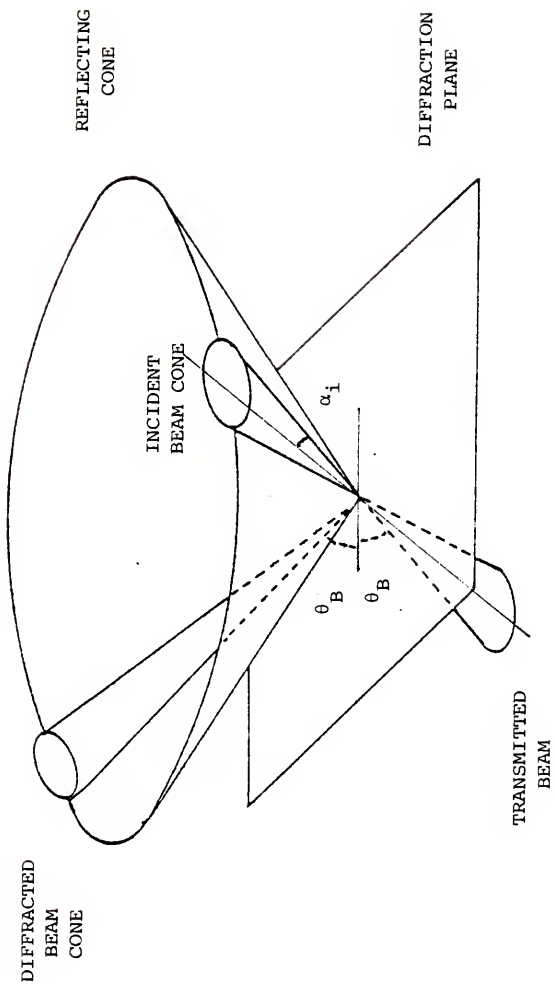


Figure 3.1 Angular relationship of the incident and diffraction beams for convergent beam diffraction. The intersection of the large reflecting cone with the Ewald sphere (not shown) defines the position of the Kikuchi or Kossel-Mollenstedt line.

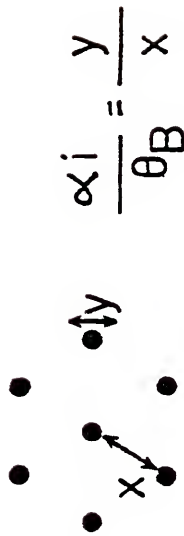
where α_i is the semi-angle of the incident beam and L is the effective camera length.

The convergent beam diffraction pattern, as diagrammed in Fig. 3.2, now consists of an array of discs whose diameter, y , is proportional to $2\alpha_i$. Only those electrons in the incident beam that strike the reflecting plane at exactly θ_B form the part of the disc with zero Bragg deviation. It is obvious that if $2\alpha_i$ is increased sufficiently, this line of "zero Bragg deviation" can extend across several orders of reciprocal lattice spots.

Calculation of α_i from the convergent beam diffraction pattern is easily accomplished (Thompson, 1977). In Fig. 3.2, the convergent beam which subtends an angle of $2\alpha_i$ strikes the specimen and produces a main beam and several diffracted rays that are focused as discs in the back focal plane of the objective lens. Bragg's law shows that the distance between the main beam and any of the diffracted beams is proportional to $2\theta_B$. Also, it is evident that the width of the disc in the convergent beam diffraction pattern is proportional to the convergence angle of the incident beam. The law of similar triangles shows that the radius of one of the diffracted spots divided by the distance between the main beam and the diffracted beam is equal to convergence angle of the incident beam divided by the Bragg angle

$$\frac{x}{y} = \frac{2\theta_B}{\alpha_i} \quad \frac{y}{x} = \frac{\alpha_i}{\theta_B} \quad (3.2)$$

Since x and y are easily measured on the diffraction pattern and $2\theta_B$ is known, the degree of collimation of the beam, α_i , can now be computed from Eqn. 3.2. Note that as α_i increases, the discs in the



calculation of
 beam convergence from
 convergent beam diffraction
 pattern

Figure 3.2 Beam convergence, defined by α_i , can be calculated by measuring the disc radius, y , and the distance between diffraction disc centers, x .

diffraction pattern increase in size until they begin to overlap as shown in Fig. 3.3a.

The camera length, which controls the size of the diffraction pattern, can be changed by adjusting the magnification lenses in the usual manner. The amount of spot overlap can be changed only by adjusting the size of the condenser aperture or the strength of the condenser lenses.

Although their method of formation is different, both Kikuchi and transmission channeling lines that are observed in electron diffraction patterns obey the geometrical relations described above. Kikuchi lines, formed by elastically scattered electrons that previously have undergone one or more inelastic collisions, are familiar in metallurgical electron microscopy and are often used as an aid to determine the exact orientation of the specimen with respect to the beam. Kikuchi lines can result even from a perfectly collimated beam; the inelastic scattering of the beam (once it enters the specimen) causes it to diverge through an appreciable solid angle.

The formation of these Kikuchi line patterns can be analyzed geometrically in Fig. 3.4. Figure 3.4a shows the scattering distribution for electrons that were inelastically scattered near the top of the specimen. Most of the electrons are deflected only slightly from the original path, and decreasingly fewer in number are scattered at greater angular deviations. Since the actual energy loss involved in a few 100 eV (Edington, 1975), some of these electrons will have been inelastically scattered in the proper direction for additional elastic Bragg scattering to occur. Such a scattering event for a

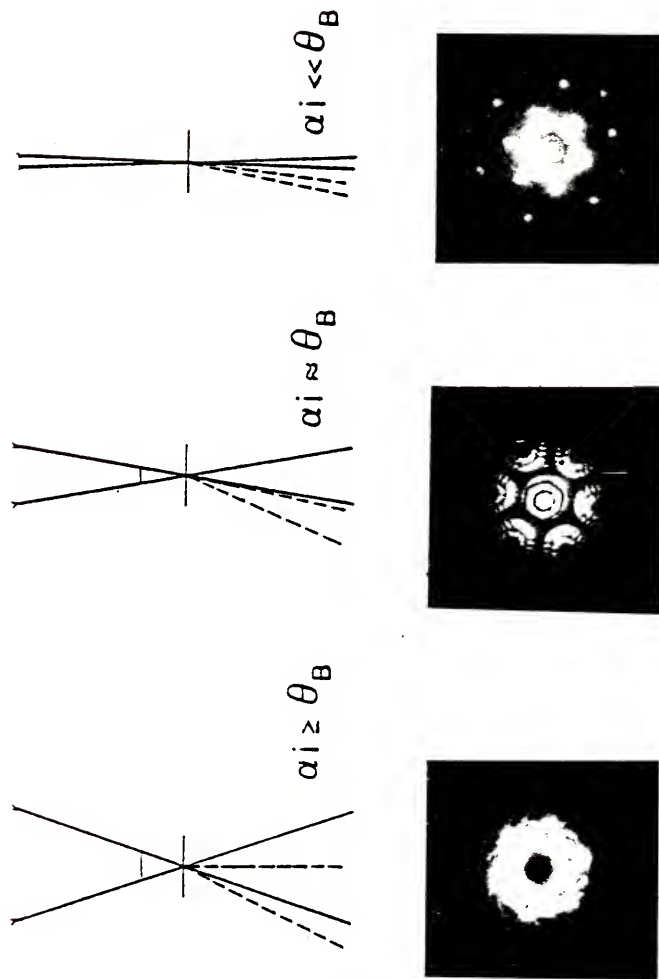


Figure 3.3 Diffraction patterns in silicon for the [111] pole. In (a), $\alpha_i \approx 10^{-2}$; (b), $\alpha_i \approx 3 \times 10^{-3}$; (c), $\alpha_i \approx 1 \times 10^{-3}$.

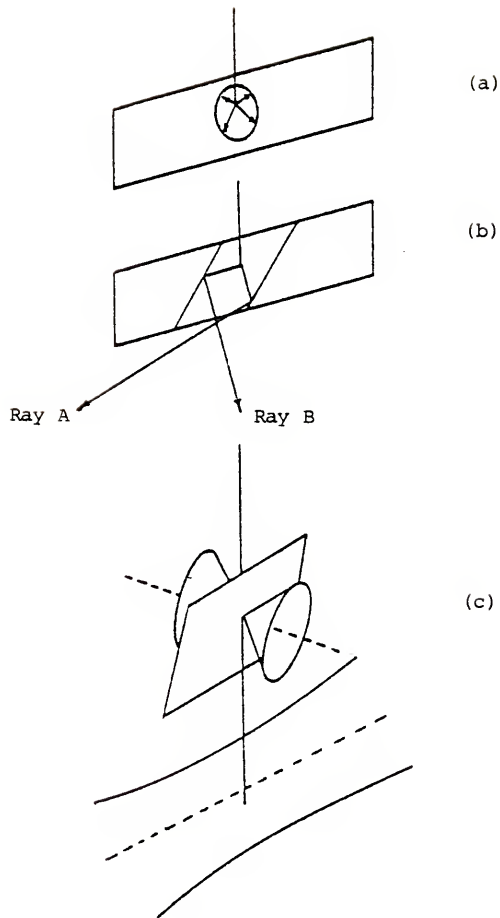


Figure 3.4 The formation mechanism and the geometrical construction for a Kikuchi line pattern. Fewer electrons are scattered along Ray B than Ray A. In three dimensions, Ray A forms the "excess" line (intensity higher than background) while Ray B forms the "deficit" line.

particular set of planes is shown in Fig. 3.4b. By referring to the intensity scattering distribution in Fig. 3.4a, it is apparent that more electrons will be scattered along ray A than along ray B. In three dimensions, Fig. 3.4c shows that each reflected plane will produce two cones of scattered electrons. Due to the shape of the scattering distribution, one cone will have a higher intensity than the diffuse background radiation, while the other cone will have an intensity lower than background. These two cones intersect the Ewald sphere to produce hyperbolae. The radius of the Ewald sphere is large enough that they appear in the diffraction pattern plane as straight lines. The importance of Kikuchi lines in determining specimen orientation can be seen by examining the effect of the rotation of the specimen on both the diffracted spots and the Kikuchi lines. For example, in Fig. 2.2a, it can be seen that a small rotation of the sample may not change the spot pattern at all if the rel-rods are of a length normally produced by a crystal of average thickness. The reciprocal lattice is simply rotated about its origin in the same angular direction as the crystal. No new intersections between the Ewald sphere and rel-rods are formed after the tilt and the spot pattern remains unchanged. However, Fig. 3.4c shows that the same tilt would result in the pair of Kikuchi lines being shifted to the new position represented by the dotted rays. Such small shifts are easily detectable in experimental situations and the relation between the incident beam direction and the specimen can be calculated by methods described in Chapter IV.

The form of transmission channeling patterns as shown in Fig. 3.5, appears geometrically quite similar to a Kikuchi pattern for the same beam direction. This similarity is no accident, as the angular relationship between the elastically scattered electrons and the reflecting planes must be exactly the same for both cases. For channeling, however, the angular range of the incident beam is produced by the focusing action of the condenser lenses and no inelastic scattering need occur to produce the channel pattern.

The rather simple kinematical models given here to describe the intensities and relative contrast present in these patterns are only an approximation and a precise description of the line intensities must make use of the dynamic theory discussed in Chapter II. The need for the dynamic theory is obvious when it is realized that the scattered beams, regardless of their position on the reflecting cone, can undergo multiple Bragg scattering and interact with the portion of the incident beam parallel to the scattering direction, as shown previously in Fig. 2.4.

A semi-quantitative theory developed by Thomas (1972) describes an n-beam solution for Kikuchi patterns simply by summing many-beam rocking curves for particular Bragg reflections. Although the effect of thickness on the rocking curve was ignored, the computer solution was able to correctly predict the relative intensities and widths of the excess-deficit Kikuchi line pairs. A more rigorous procedure (C. R. Hall, 1970) used the dynamical two-beam equations to show that contrast reversals could occur in a Kikuchi band as thicker areas of the crystal were examined.

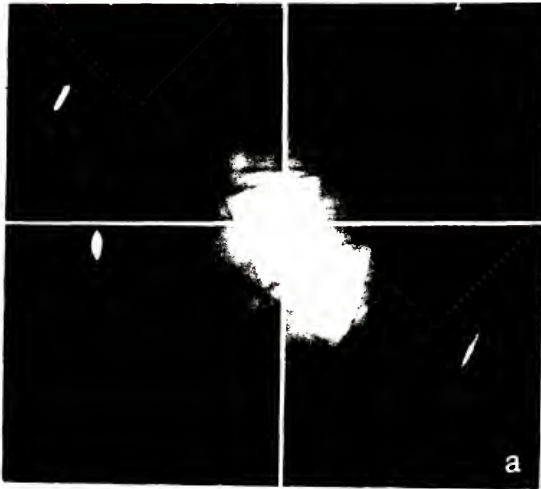


Figure 3.5 Comparison of Kikuchi patterns and transmission channeling patterns from silicon. The degree of beam convergence is different in (b) and (c).

Although image simulation techniques for channeling or Kikuchi patterns could be further developed, there seems no obvious advantage in using such a method for the examination of distorted crystals or defect strain fields. Any dynamic information in the channeling patterns resulting from defect-beam interactions should also be available in the convergent beam diffraction disc pattern in a more easily interpretable form. In addition, the use of diffraction information from either convergent beam radiation or inelastically scattered electrons implies that a larger volume of crystal is irradiated than would be the case for a STEM probe with a semi-angle less than 10^{-3} rad. As shown in the review paper by Goldstein and Williams (1977), inelastic scattering in thin foils results in x-ray production from a volume with an average diameter much larger than the original diameter of the probe. Thus, a Kikuchi pattern produced from a small STEM probe probably arises from a significantly greater volume than the region that gives rise to the dynamic bright-field intensity of the diffraction discs themselves. This follows from the fact that the bright-field intensity is restricted to elastic scattering and electrons suffering high angle collisions should not directly contribute the $|T|^2$ value of the diffraction disc, itself.

For these reasons, only the geometrical information present in Kikuchi or channeling microdiffraction patterns can be used for examination of distorted foils. Even with this limitation, analysis of the line patterns can yield considerable information as long as $\bar{g} \cdot \bar{R}$ does not vary in the local volume illuminated by the electron beam.

As a first example, an approach described by Cowley and Smith (1971) is used to determine the state of curvature of a small area of a foil. In Cowley and Smith's paper, a convergent beam was used to produce a channeling pattern such as the ones shown in Fig. 3.5. Cowley and Smith discovered that by de-focusing the convergent beam such that the cross-over does not coincide with the specimen plane, each excess and deficit channel line pair can be split into two distinct lines, where the width of the splitting is governed by the amount of defocus. Examples of the line splitting effect for a particular channel line pair are marked by arrows in Fig. 3.5b and c. The explanation for the effect is shown in Figs. 3.6 and 3.7, which have been reproduced from Cowley and Smith's paper.

Consider the incident and diffracted rays from opposite sides of the convergent cone for perfect crystal (Fig. 3.6). For this case, the incident rays that lie at the proper angle for Bragg diffraction are parallel to the scattered rays produced by the rays on the opposite of the cone. For the case of a bent crystal, shown in Fig. 3.7, this is no longer true. Now the transmitted rays deviate by angle θ' is radius of specimen curvature. From the figure, it can be shown that

$$x_1 = 2\theta_B L \quad (3.3)$$

$$y_2 = \theta' L$$

where

x_L = the separation between a particular transmitted and scattered ray

x_2 = width of line split in the diffraction pattern

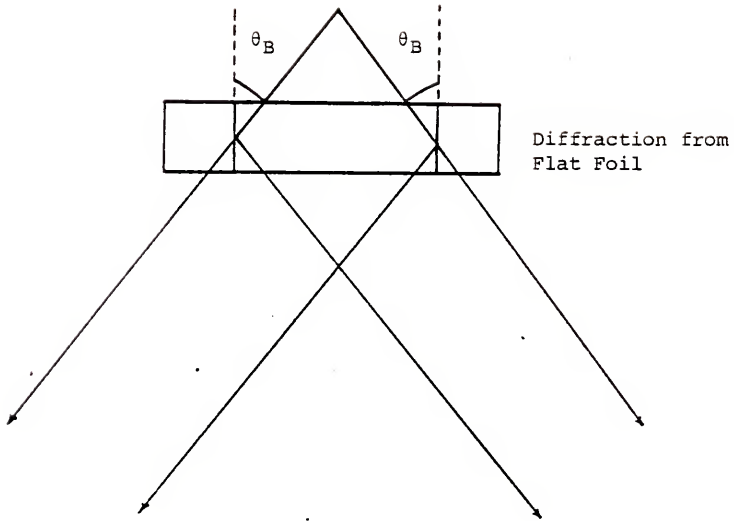


Figure 3.6 Cowley diagram for diffraction from a flat crystal.
Cowley and Smith (1971)

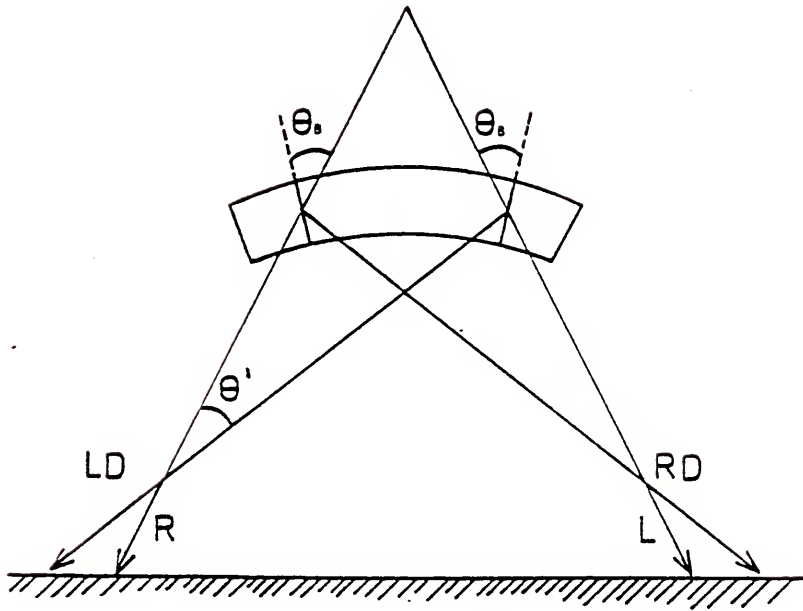


Figure 3.7 Cowley diagram for diffraction from a bent crystal.
Cowley and Smith (1971)

L = camera length

Manipulation of Eqns. 3.2 and 3.3 shows that the radius of curvature of the foil is

$$r = \frac{z(x_1 - x_2)}{x_2} \quad (3.4)$$

where z is the amount of defocus, or the distance of the cross-over from the specimen.

Since the effect is dependent upon a defocused probe, Cowley and Smith's method is not a true microdiffraction technique but it does provide an explanation for much of the fine detail seen in the channeling pattern.

3.2 The Use of Channeling Patterns to Characterize Polycrystalline Specimens

A method of analysis of more general utility than Cowley and Smith's, using geometrical information from either Kikuchi patterns or channel patterns resulting from a focused probe, is developed below.

Consider the case where a fine-grained polycrystalline foil is to be analyzed by microdiffraction. It is desired to characterize the crystalline structure by determining the difference in crystal orientation between grain 1 and 2, shown schematically in Fig. 3.8. If the microdiffraction pattern is recorded from each grain, the direction of the beam (Helfmeier and Feller-Kniepmeier, 1977) is

$$\overline{BM} = \frac{\overline{z}}{|\overline{z}|} - L_1 f_1 \frac{\overline{g_1}}{|g_1|} - L_2 f_2 \frac{\overline{g_2}}{|f|} \quad (3.5)$$

where $Z = \overline{g_1} \times \overline{g_2}$ = the approximate beam direction.

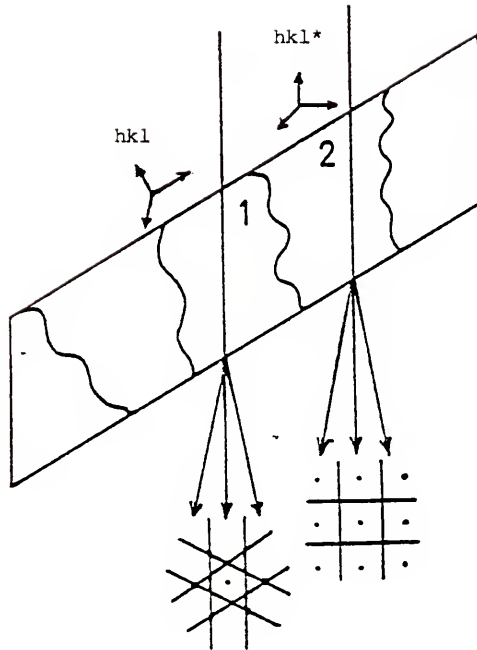


Figure 3.8 If Kikuchi or channeling patterns are recorded for two adjacent grains, the orientation of the two grains can be determined from measuring the local beam direction for each grain for two different specimen tilts.

L_1 , f_1 , L_2 , and f_2 are measured from the diffraction pattern. A fuller discussion describing computation of the exact beam direction is discussed in Section 4.2. Let a superscript (*) designate the beam direction from grain 2 and a prime (') show the beam directions for both grains after the foil is tilted to a new position.

For position 1, the relation between the two grains for any cubic crystalline structure is

$$BM_i = l_{ij} BM_j^* \quad (3.6)$$

Similarly, for position 2

$$BM_i' = l_{ij} BM_j^{*'} \quad (3.7)$$

where l_{ij} is the 3 x 3 direction cosine array describing the orientation difference between the two grains. If each set of equations is expanded, the ones involving BM_1 are

$$BM_1 = l_{11} BM_1^* + l_{12} BM_2^* + l_{13} BM_3^* \quad (3.8)$$

$$BM_1' = l_{11} BM_1^{*'} + l_{12} BM_2^{*'} + l_{13} BM_3^{*'}$$

and, it can be shown that

$$1 = l_{11}^2 + l_{12}^2 + l_{13}^2 \quad (3.9)$$

This is a set of three equations in three unknowns, l_{11} , l_{12} , and l_{13} . Using the equations involving BM_2 , a similar set of equations can be solved for l_{21} , l_{22} , and l_{23} . The final three direction

cosines are then determined with

$$\begin{aligned} l_{11} \underline{l_{31}} + l_{12} l_{32} + l_{13} l_{33} &= 0 \\ l_{21} l_{31} + l_{22} \underline{l_{32}} + l_{23} l_{33} &= 0 \\ l_{31}^2 + l_{32}^2 + \underline{l_{33}^2} &= 1 \end{aligned} \tag{3.10}$$

where the underlined components are the remaining unknowns.

This method can be used to describe the orientational relations between two adjacent areas of a distorted sample, low angle grain boundary, or two different grains of the same crystal phase. Similar sets of equations can be used to solve the orientation between two phases of different crystal structure. It is important to note that this method can be used regardless of the orientation of the specimen with respect to the beam and is dependent only on an accurate computation of the beam direction using either Kikuchi or transmission channeling patterns. While this method is also applicable to standard selected area diffraction techniques, it can be used to the fullest extent only with microdiffraction techniques. Many structural features in metals are much less than 1 μm in extent, and some, such as grain boundaries and stacking faults, are only a few atomic layers in thickness. For example, only a very narrow probe could be positioned close enough to an end-on grain boundary to produce useful information about its local orientation and strain field.

3.3 A Review of Ray Optics for Convergent Beam Diffraction

In the Philips 301, a strongly demagnifying upper objective lens field makes it possible to form a much smaller focused spot than was possible in earlier electron microscopes. However, the incident on the specimen is now much more convergent than before. For the TEM mode in the Philips 301, the two condenser lenses and the upper half of the objective lens field are used to illuminate the specimen, while the lower half of the objective, diffraction, intermediate and projector lenses are used to form a magnified image on the phosphor screen.

In Fig. 3.9, the filament image formed slightly below the electron gun assembly is demagnified by the first condenser lens (C1 - not shown), and both the second condenser lens (C2) and the upper half of the objective lens are used to further demagnify the image on the specimen plane. Although the objective polepiece used for both TEM and STEM imaging strongly demagnifies the C2 cross-over, its excitation value is coupled to the lower objective polepiece and must be set to a certain value for a focused image.

For the imaging mode, the C2 lens is adjusted so that its cross-over lies close to the upper focal plane of the upper objective polepiece (Fig. 3.9a). The cross-over then acts as a pseudo-point source which the upper objective lens field converts to a relatively well-collimated beam that illuminates the specimen.

One advantage of the imaging mode in the TEM (mode) with the Philips 301 is that the C2 aperture can be focused on the sample in

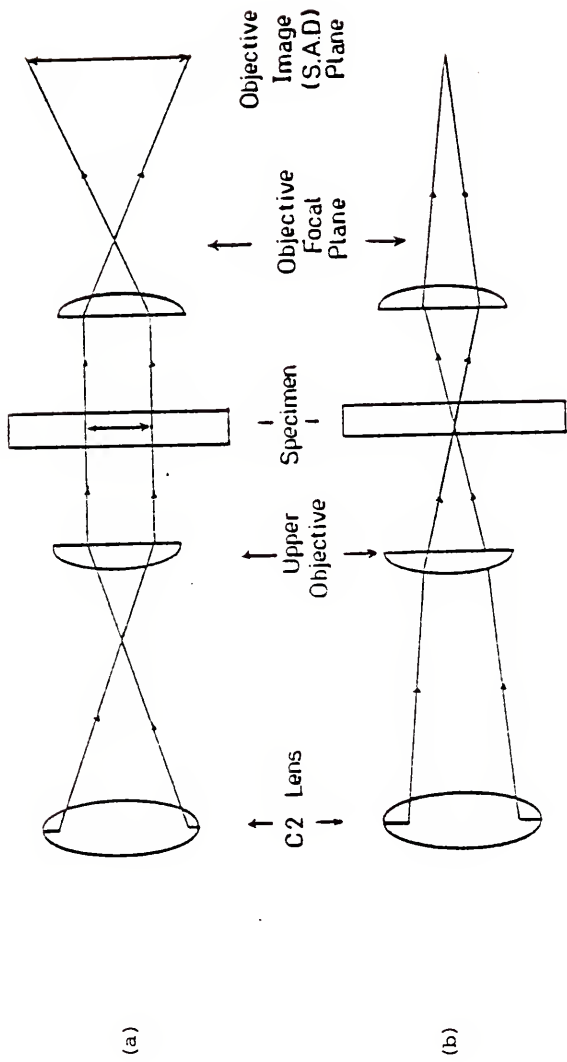


Figure 3.9 TEM ray Optics for imaging (a) and focused spot (b) modes in the Philips 301.

exactly the same way that the selected area diffraction aperture above the diffraction lens can be focused on the lower objective image plane.

Consider Fig. 3.10, which shows the physical arrangement of the objective polepieces and the specimen as well as the ray diagram for a perfectly collimated beam. The specimen lies in the middle of the polepiece gap, near the center of the magnetic field formed by the polepieces. The actual magnetic field in the polepiece gap is great enough that it cannot be treated as a "thin" lens and the standard ray tracing rules used in geometrical ray optics do not apply.

The specimen, of course, is a real object, and only the portion of the lens field to the right of the specimen can be used to produce a magnified specimen image (Hall, 1966). Useful information from ray tracing can still be obtained if the objective lens field is considered to be formed from two thin lenses, and this construction is used in the ray diagrams supplied by the manufacturer.

Using this assumption, the objective lens field is treated as two thin lenses, and it can be seen from Fig. 3.11 that the upper objective lens forms a demagnified image of the C2 aperture at (a), while the lower objective lens forms a magnified image of the specimen at (b). The method of selected area diffraction developed by Poole (1947), involves placing an aperture at (b), so that only the central part of the image is used to form the diffraction pattern at (c). By tracing the rays from (d) to (b), it can be seen that the selected area aperture allows only rays from the part of the specimen (e-e) to form the diffraction pattern that is recorded photographically.

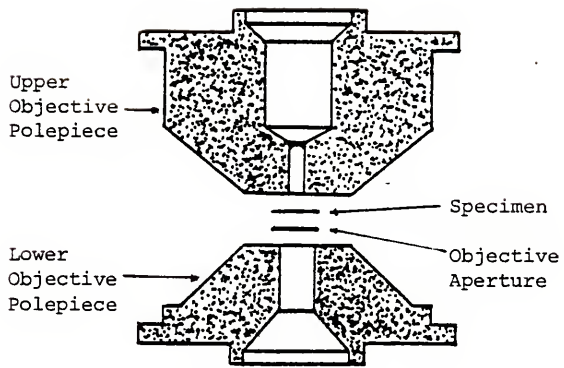


Figure 3.10 Dimensions of the Objective Polepieces for the STEM Modification of the Philips 301.

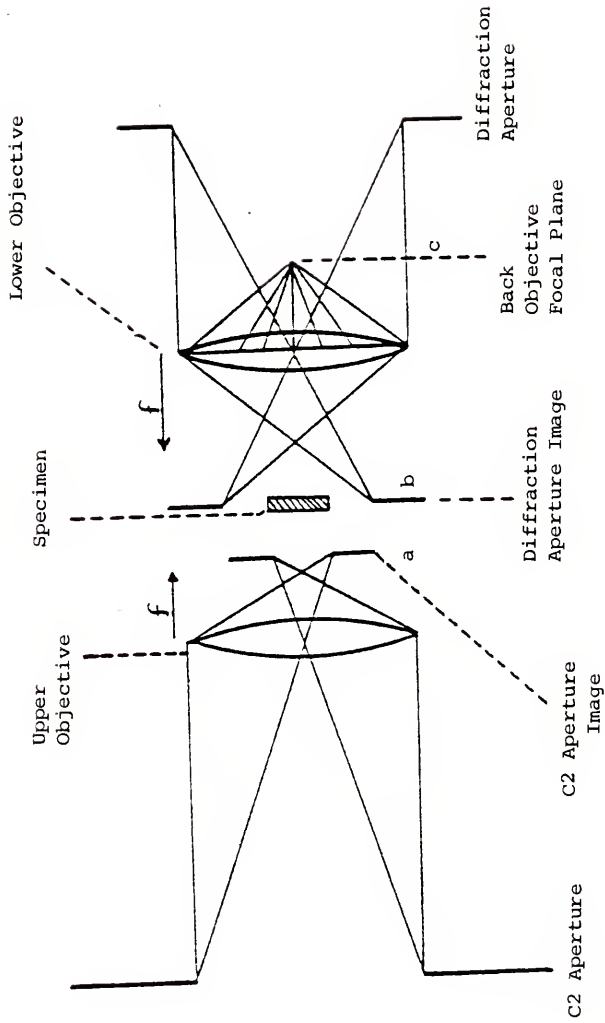


Figure 3.11 Ray diagram for focused C2 aperture microdiffraction and the standard method of selected area diffraction. In both cases, the aperture image and the specimen must coincide.

However, if the specimen is raised to a non-eucentric position to coincide with the image of the condenser aperture, a "selected area" diffraction pattern will again be formed. In this case, the condenser aperture permits only a small area of the sample to be illuminated, and it is this area alone that forms the pattern. For the Philips 301 STEM polepiece, the condenser aperture is demagnified 38 times, while the selected area diffraction aperture is demagnified 14 times at the specimen plane.

Because of spherical aberration, the utility of the focused condenser aperture method is even more favorable than suggested by these demagnification ratios. This point is explored further in the discussion on lens aberrations.

To produce the convergent beam diffraction pattern, the strength of the C2 lens is reduced such that its cross-over would lie below the specimen if the objective lens were turned off (Fig. 3.9b). At the proper excitation strength the objective lens now acts to increase the convergence of the beam and focuses the rays to produce a cross-over at the specimen plane. The objective lens is always kept at the same excitation, so calculations involving spot size or convergence angle changes can be accomplished by considering the lens strength and the aperture sizes of the C1 and C2 condenser lenses alone (Fig. 3.12).

Consider Fig. 3.13, where the distance from the gun cross-over to the C1 lens, O , is fixed, but the lens to cross-over distance, I , depends on the strength of the C1 lens. Since the refractive index

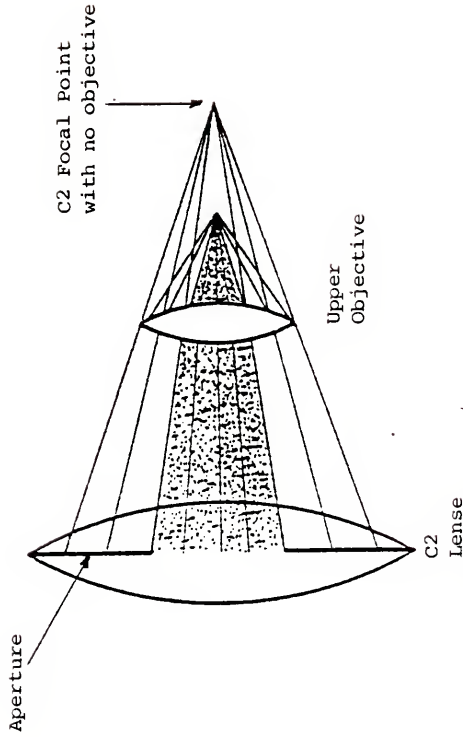


Figure 3.12 Details of the TEM focused spot mode of microdiffraction. The C2 lens produces moderately convergent radiation which is focused to crossover by the upper objective lens field. Since the strengths of the C2 and objective lens remain fixed for a particular spot size, only the C2 aperture can control convergence. Note that the stippled area is more collimated than would be the case if the C2 aperture were removed.

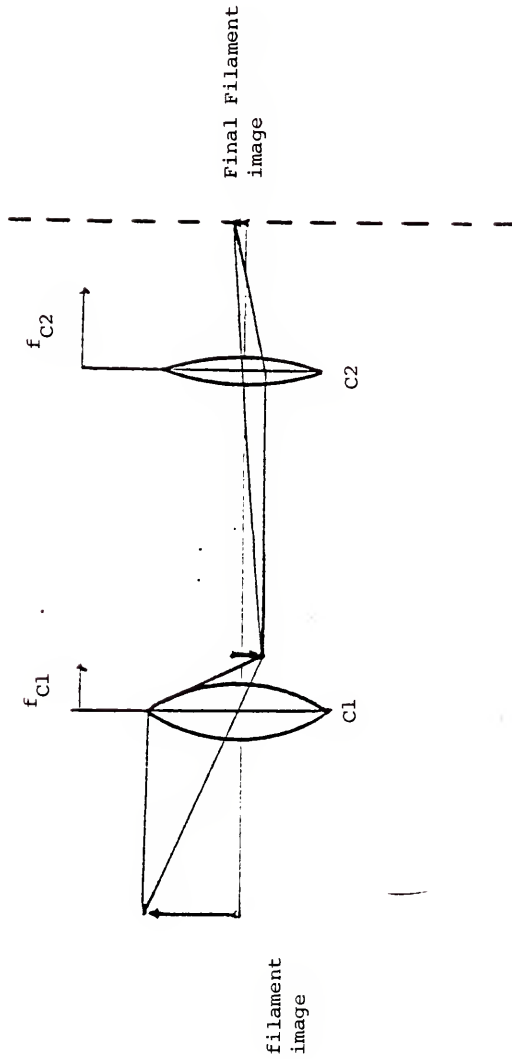


Figure 3.13 Both the C1 and C2 lens de-magnify the gun assembly crossover. However, the stronger C1 lens serves primarily to de-magnify the spot and the C2 lens focuses the spot at the specimen plane so convergence is fixed except for aperture changes.

of electrons is the same on both sides of the C1 lens, $f_1 = f_2 = f$ and the thin lens equation is

$$\frac{1}{O} + \frac{1}{I} = \frac{1}{f} \quad (3.11)$$

As the C1 lens is increased in excitation the focal length must decrease and since O is fixed, I must decrease proportionally. The demagnification of the spot is given by the ratio

$$M = \frac{I}{O} \quad (3.12)$$

It can be seen that by increasing the C1 lens strength, the cross-over is brought closer to the right-hand side of the lens and the filament image is demagnified, thus forming a smaller spot. Once the spot size has been selected by a particular C1 lens excitation, only one possible setting for the C2 lens and the objective lens can be used if a focused spot is to be produced in the specimen plane. Thus, a specific C1 setting determines not only the spot size, but the convergence, α_1 , of the incident beam. The C2 lens can be used to alter α_1 , but at the expense of forming a defocused spot on the specimen plane. However, the convergence of the beam may still be increased by changing the size of the aperture used with the C2 lens. As was shown in Fig. 3.12, substituting a smaller aperture in C2 reduces α_1 while leaving the spot size essentially unchanged since all three lens excitations remain the same.

It is important to see that angular resolution in the diffraction pattern and the current density of the focused spot (and thus the intensity of the diffraction pattern) are inversely proportional.

It has been shown (Broers, 1969), that the intensity of the beam at the specimen, j_i , in amperes/cm² is proportional to the intensity at the gun, j_o , by

$$j_i = j_o \frac{eV \sin^2 \alpha_i}{KT \sin^2 \alpha_k} \quad (3.13)$$

But both α_i and α_k , and thus the intensity of the microdiffraction pattern, are controlled directly by the C2 aperture diameter.

STEM microdiffraction methods differ from TEM convergent methods in that the specimen is still illuminated by a focused probe, but the image is formed sequentially as the probe is rastered over a rectangular area of the sample. To form a microdiffraction pattern from a specific region, all that is required is to stop the rastering motion produced by the deflection coils situated between the objective and C2 lenses, and manually adjust the deflection controls to place the probe over the desired area by watching the STEM image on the CRT. Regardless of the position of the probe, the microdiffraction patterns will be formed in the back focal plane of the lower half of the objective lens.

Ray optics in STEM are described in Fig. 3.14. As in TEM, spot size can be varied by altering the C1 lens strength, but in STEM the C2 lens is turned completely off. The average convergence for a given probe size is now an order of magnitude greater than the TEM mode, but the spot sizes can be decreased proportionately. For example, the smallest spot size attainable with the standard hairpin filament is 400 Å with the C2 lens on (TEM convergent beam mode),

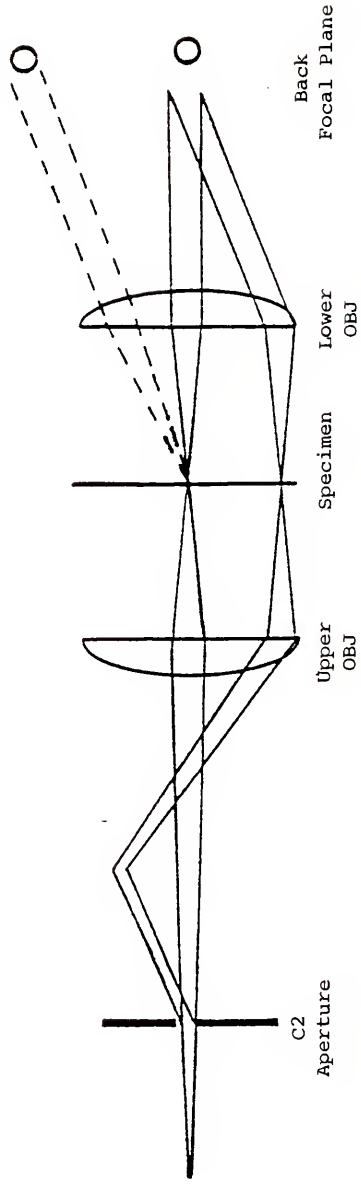


Figure 3.14 STEM ray optics. The upper objective lens both focuses the probe and aligns the deflected beam parallel to the optic axis. Convergence is controlled by the C2 aperture alone and the diffraction pattern is first formed in the back focal plane of the lower objective lens just as for TEM.

but 40 \AA with it off. As shown in the inset in Fig. 3.14, α_1 is now controlled only by the C2 aperture. If the distances between the condenser lenses and the distance from the C2 aperture to the upper focal plane of the objective lens are known, α_1 can be easily calculated. However, actual diameters of commercially available apertures may vary as much as 20% from the specification and it is more accurate to calculate convergence directly from the microdiffraction pattern as is done in Chapter IV.

Once the C1 setting and C2 aperture size are chosen to select a particular spot size and current density, the STEM image is formed by using the wobbler coils to twice deflect the beam below the C2 aperture such that the beam pivots in the upper focal plane of the objective lens. As shown in Fig. 3.14, the upper objective field lens not only focuses the beam to a probe but converts the angular beam deflection to a deflection that remains parallel to the optic axis. Trimming potentiometers used to adjust the height of this pivot point must be carefully adjusted if the probe is to remain parallel to the optic axis over the entire raster scan. If this condition is not met, the Bragg deviation for any given hkl plane will vary over different parts of the scanned area and the image contrast will not be comparable to that for a collimated beam used in TEM imaging.

Once the probe passes through the specimen the diffraction pattern is formed in the back focal plane of the lower objective lens, just as it is in the standard TEM modes. The probe still remains parallel to the optic axis after passing through the specimen

solid rays in 3.14) and it always converges to the same spot in the back focal plane after being focused by the lower objective lens regardless of its position in the scan. In the same fashion, diffracted rays (dotted rays) scattered through the same Bragg angle at different points of the scan are all focused to another point, forming a diffraction spot for a particular set of hkl planes.

The remaining lenses below the objective lens, diffraction and projector lenses, only magnify the size of the microdiffraction pattern such that the diffraction discs subtend approximately the same angle as the solid state detector at the base of the column. The diffraction lens must be set at a fixed value so it can be focused on the back focal plane of the objective lens, so only the projector can be varied to adjust the camera length, or the size of the pattern appearing in the detector plane. By varying the projector lens strength, the size of the diffraction discs can be adjusted so that only the central portion of a disc strikes the detector, thus giving indirect control of α_0 , the exit angle of the electron beam leaving the specimen. Therefore the degree of coherence of the electron beam used to form the STEM image can be controlled by selecting only the central portion of the diffraction disc just as a selected area diffraction pattern is formed from only a portion of the bright- or dark-field image.

3.4 The Effect of Lens Aberrations

The advantages of obtaining diffraction patterns from small areas are obvious. The region of interest, whether a small second

phase particle or a localized strain field from a dislocation, is small in volume compared to the surrounding matrix. The smaller the total volume which is examined by diffraction, the greater the particle-matrix volume ratio and the better the signal to noise ratio in the diffraction pattern. What is not so obvious is why microdiffraction patterns cannot be obtained with standard selected area diffraction techniques where very small apertures are used to select a correspondingly small portion of the image. The answer lies in the nature of the aberration errors common to any electro-magnetic lens.

The most important of these lens defects is spherical aberration which results from electrons passing through the outer portion of a lens being focused more strongly than those electrons passing closer to the optic axis. The ray bundle cannot be brought to focus in a single focal plane, and an image of a point appears as a disc with a radius equal to

$$r = C_s \beta^3 \quad (3.14)$$

where C_s , the spherical aberration constant equals 6 mm for the Philips 301 STEM polepiece and, β , the lens aperture angle is controlled by the size of the objective aperture. Reducing the size of the objective aperture thus decreases β and the disc of confusion, r , but the process cannot be carried too far, or resolution again begins to decrease due to the diffraction effects caused by a very small aperture.

For the TEM diffraction mode, the objective aperture must be removed. Now the diameter of the selected area diffraction aperture is the factor that limits the effectiveness of selected area diffraction. Consider the formation of the selected area diffraction pattern shown in Fig. 3.15. The diffraction pattern from the entire area illuminated by the incident beam is formed in the back focal plane of the objective lens and the (000) beam is magnified to form the bright-field image. If the selected area aperture above the diffraction lens is placed such that it is in focus with the image, tracing the rays back to the specimen plane shows that the diffraction pattern appearing on the phosphor screen results only from the portion of the image within the selected area diffraction aperture. This is true even though the diffraction pattern from the entire illuminated area is still present in the back focal plane of the objective lens.

Diffracted beams, however, pass through the lower objective lens inclined at an angle $2\theta_b$ from the optic axis and are subject to spherical aberration. The diffracted beam that would be focused on a flat focal plane by a perfect lens is brought to focus on a spherical surface. By examining the image plane it can be seen that the image formed by the main beam and the diffracted beam do not coincide and this lack of coincidence increases as $2\theta_b$ increases. Thus, it is apparent that the diffraction spots in the selected area diffraction pattern are not formed from the same area of the specimen as the main beam. The extent of the error is described by the equation

$$x = C_S (2\theta_b)^3 \quad (3.15)$$

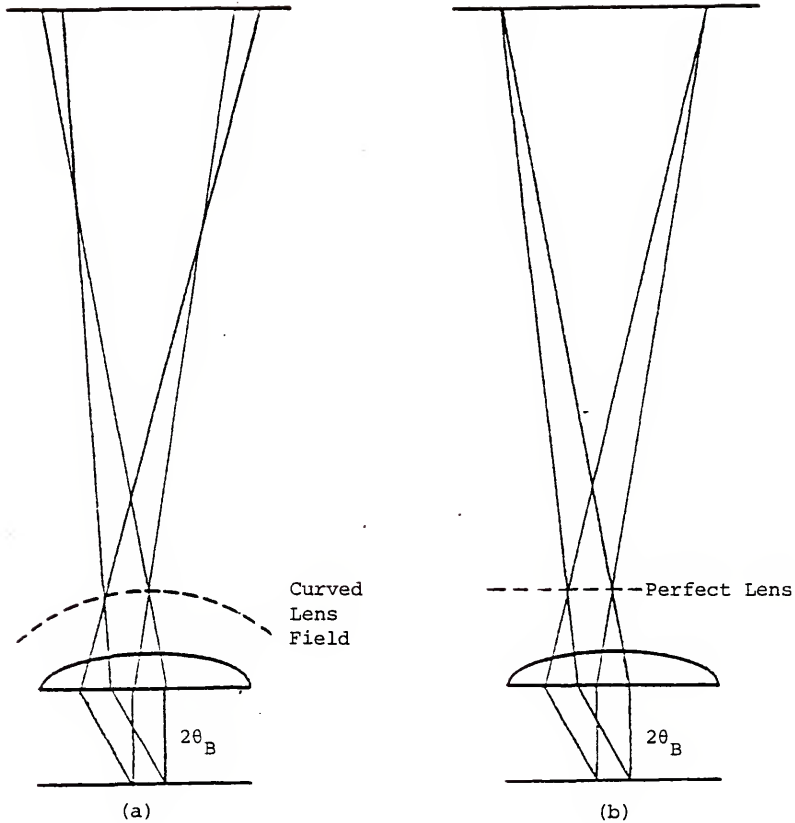


Figure 3.15 The spherical aberration of the objective lens forms a curved focal plane as shown in (a). For a perfect lens (b) the focal plane remains flat.

where x is the distance on the image between the centers of the origin of the main beam and the diffracted beams. As the selected area at the specimen plane decreases in size below $0.5 \mu\text{m}$, the main and diffracted beam areas do not even overlap and the selected area technique is of little utility.

With a STEM polepiece, the strongly de-magnifying upper objective lens field allows the C2 aperture to be imaged on the specimen plane itself. For this method only a small portion of the sample is illuminated and only this part of the sample can produce the pattern. Thus the focused C2 aperture technique permits a quick and effective way to produce microdiffraction patterns from areas as small as 2000 \AA in diameter. The limitation in aperture diameter due to spherical aberration when the diffraction aperture is used no longer applies. Only standard TEM optics are required, and the angular resolution in the diffraction pattern is equal to the older selected area method. The role of spherical aberration is confined to a slight distortion of the diffraction pattern, shown in exaggerated form in Fig. 3.16. According to Hirsch (1972), the distortion increases for higher order reflection (as these rays are deflected further from the optic axis) but is only about 1% for the 3rd order diffraction spots.

3.5 A Review of the Rocking Beam Microdiffraction Method

A method that circumvents the contamination and angular resolution problems common to convergent beam techniques is the rocking beam microdiffraction method. As developed by Van Oostrum (1973)

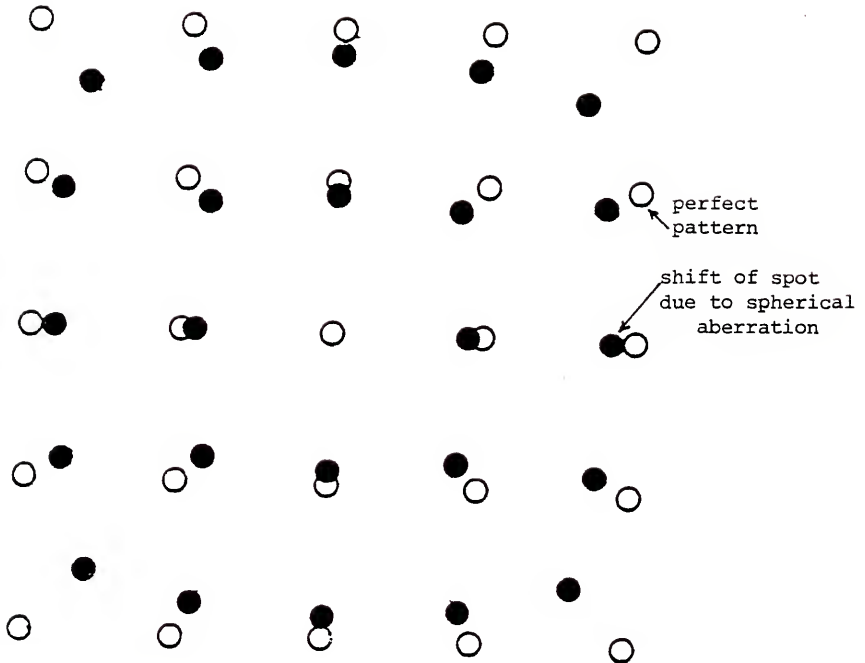


Figure 3.16 Barrel distortion in the diffraction pattern resulting from spherical aberration of the objective lens. This aberration is present for both the focused C2 aperture and the standard selected area diffraction techniques.

and Geiss (1975), the rocking beam method makes use of the scanning coils to pivot the incident beam over the specimen surface in such a manner that the bright-field and dark-field images are swept across the detector at the base of the column in the Philips 301. The detector, of course, can sense nothing about the character of the images that momentarily appear on the phosphor screen-it simply detects an increase in current density as each dark-field image comes in view. As the pivoting of the beam is repeated in a regular fashion, the increase in electrons striking the detector result in a momentary increase in the signal sent to the STEM unit electronics, forming a diffraction "spot" each time the incident beam is tilted at the appropriate angle. In spite of its unique method of formation, the rocking beam diffraction pattern closely resembles the patterns produced by selected area diffraction methods, and shows both dynamic and kinematic effects.

The ray diagram for rocking beam diffraction is shown in Fig. 3.17. Consider the effect of the upper objective lens field on the imaging of the second condenser aperture. As discussed in the Section 3.3, the distance of the second condenser aperture is such that the upper objective lens forms a strongly demagnified image of the aperture in its back focal plane. Using the principles of ray tracing, it is apparent that any ray, regardless of its initial direction, that emanates from the aperture plane must still strike the same point in the plane to the right of the lens where the aperture image is formed.

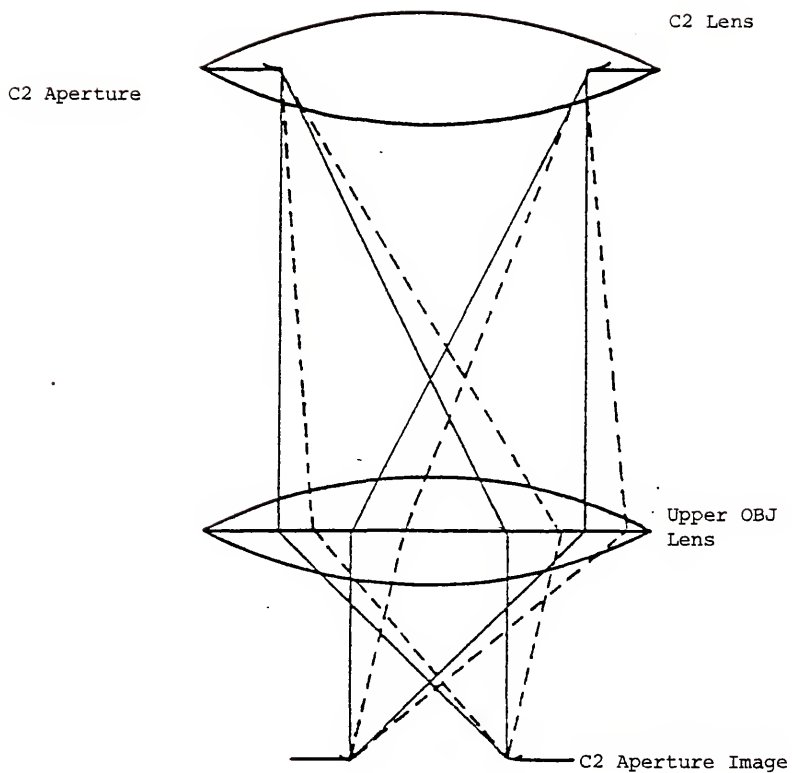


Figure 3.17 Ray optics for rocking beam microdiffraction. Any ray emanating from the edge of the C2 aperture must converge to the equivalent point of the C2 aperture image.

A well-collimated beam used to form a normal TEM image can then be regularly deflected with the scanning coils such that the pivot point is co-planar with the aperture. As long as this condition is satisfied, the aperture image will remain stationary in the image plane, regardless of the angular direction of the beam. When the specimen height is adjusted to coincide with the aperture image plane, the requirements for rocking beam diffraction are satisfied. Now, the same area of the sample remains illuminated during the beam rocking process.

Although the specimen must be placed in a slightly non-eucentric position to coincide with the aperture image, the lens settings for the rocking beam method are the same as the focused condenser aperture method discussed in Section 3.3. The deflection of the beam produced by the scanning is no different from the deflection that occurs when a dark-field image is formed by manually tilting the incident beam to a specific position.

The angular extent of the rocking beam pattern formed on the CRT is controlled by the angular deflection of the beam, and the deflection itself is controlled by the magnification control on the STEM panel. Because the STEM imaging mode increases magnification by decreasing the scanned area, it follows that adjustment of the same control when in the rocking beam mode simply reduces the angle of rock.

It is important to see that the rocking beam pattern is formed from only the portion of the image that strikes the detector. In standard selected area diffraction methods, the portion of the image that forms the diffraction pattern is chosen with the size of the

diffraction aperture. In the rocking beam method, it is the diameter of the solid state detector that determines the portion of the image chosen. Thus, by increasing the magnification an increasingly smaller image segment is permitted to strike the detector and form the microdiffraction pattern. The detector diameter can also be reduced by masking it with an aperture (Geiss, 1975) if even smaller portions of the image used to form the pattern are desired.

For the Philips 301, the diameter of the detector is 4 mm and the maximum magnification at the detector height is 130,000X, so the minimum selected area is

$$A = \frac{D}{M} \frac{4 \text{ mm}}{130,000} = 308 \text{ \AA}^2 \quad (3.16)$$

Geiss (1975) has reduced the diameter of the detector down to 1.0 mm and has obtained single crystal diffraction pattern from vapor deposited gold islands less than 100 \AA in diameter. Signal strength decreases as the active detector area is reduced or sample thickness is increased. A more practical limit for obtaining microdiffraction patterns with a reasonable signal to noise ratio from typical metallurgical thin foil specimens is 500 \AA^2 .

Angular resolution of the diffraction discs in the rocking beam pattern is controlled by the size of the objective aperture. A μm objective aperture results in a pattern with resolution comparable to standard selected area diffraction, while removing the aperture entirely produces a rocking beam channeling pattern quite similar to the focused beam channeling patterns discussed previously. Patterns from a 2000 \AA^2 area in silicon for 4 different objective aperture sizes are shown in Fig. 3.18.

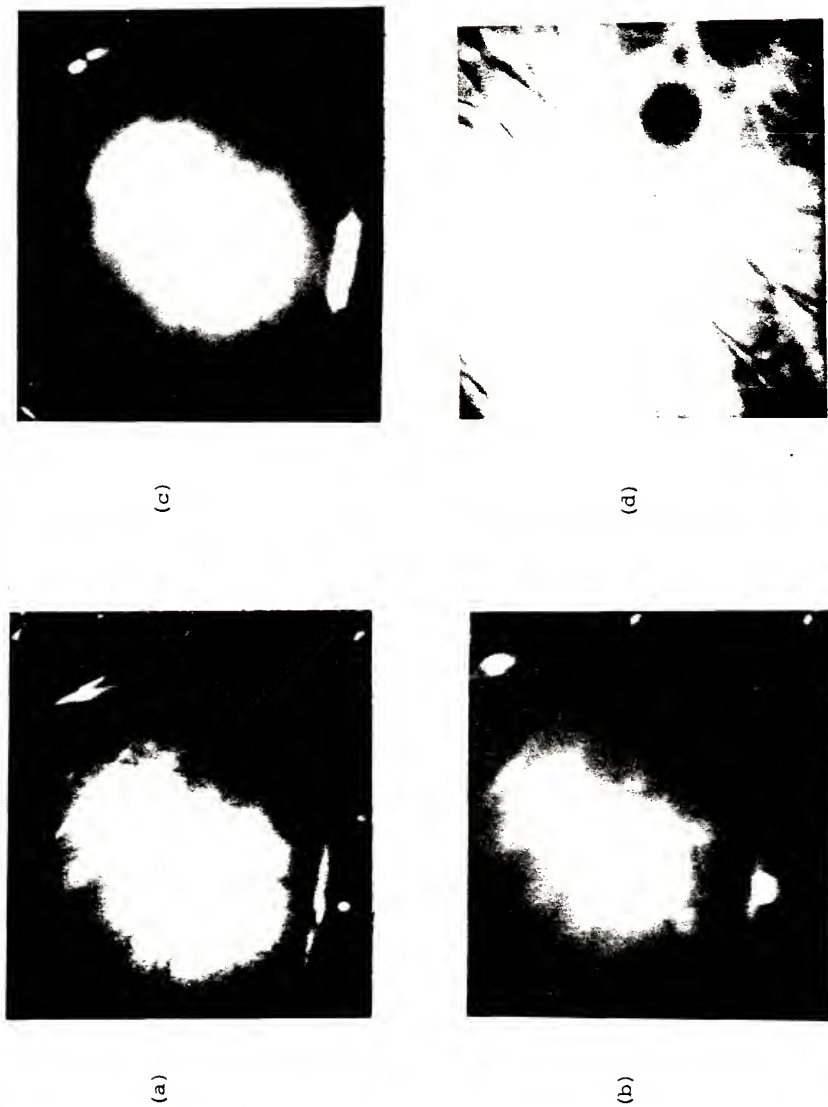


Figure 3.18 Rocking beam microdiffraction and transmission channeling patterns of $\langle 111 \rangle$ pole in silicon for 4 different objective aperture sizes.

These results are explained by Fig. 3.19, which shows that the diffraction pattern in the back focal plane of the objective lens must be swept across the objective aperture just as the image is swept over the detector. The objective aperture diameter d , limits the divergence of the rays in any diffracted beam. Thus, the maximum angular divergence is found by the ratio of the focal length of the objective lens and the objective aperture diameter:

$$\rho = d/f \quad (3.17)$$

For the Philips 301, $f = 3.7$ mm, so an objective aperture of $5 \mu\text{m}$ (the smallest practical size) gives a maximum angular resolution of $\rho = 1.35 \times 10^{-3}$ rad. Thus, the angular resolution for rocking beam compares favorably with other microdiffraction techniques.

3.6 Transmission Channeling Patterns by the Rocking Beam Method

In Fig. 3.18d, it is seen that completely removing the objective aperture produces a transmission channeling pattern similar to the channeling patterns described in Section 3.1. These patterns, however, have been formed with a well collimated beam. The explanation is shown by Fig. 3.19, where a completely collimated beam is rocked through the necessary solid angles such that the Bragg angle for a particular diffracting plane is satisfied at opposite sides of the optic axis. Since the rocking occurs in three dimensions the cone that is formed is similar in angular extent to the incident beam cone shown in Fig. 3.1.

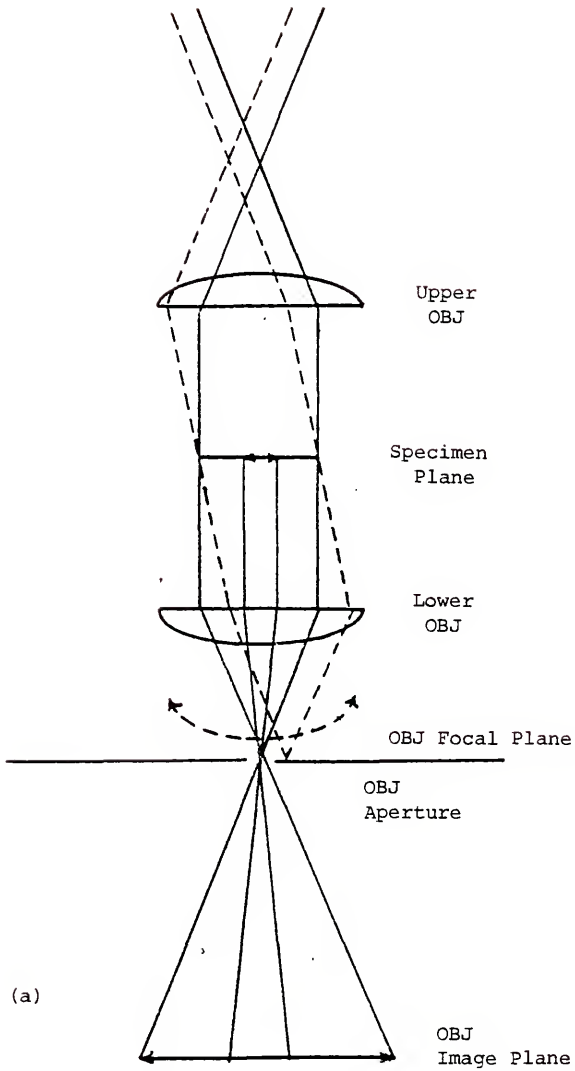


Figure 3.19 Rocking beam ray diagram showing how the objective aperture controls angular resolution.

Both cases produce exactly the same channeling line pair in the back focal plane of the objective lens. For the convergent beam case, the pattern is formed all at one time since different segments of the beam form different angles with the diffracting planes. For a rocking beam, the pattern is formed sequentially in time, and a well-collimated beam is now positioned by the scanning coils at precisely the right angle to form one segment of the channel line seen in the diffraction pattern.

Channeling patterns formed from solid samples with the scanning electron microscope have been studied for several years (Coates, 1970) and can be formed either by backscattered electrons or specimen current. These SEM channeling patterns are limited to solid samples. In addition, the longer focal lengths of the final probe forming lenses typical of commercial SEMs results in much greater spherical aberration than the corresponding STEM lens, and the minimum specimen area that can be studied is only about 2 μm in diameter (Van Essen and Schulson). Transmission channeling patterns were first produced by Fujimoto *et al.* (1972) using JEOL 100B STEM but no experimental images were shown and the minimum area that could be used to form a pattern was not described. Aside from the paper by Fujimoto, transmission channeling patterns produced by rocking beam methods have not been discussed in the scientific literature.

The spherical aberration of both the upper and lower objective lens fields determines the minimum area that can be used to form the rocking beam microdiffraction pattern. For the rocking beam method, spherical aberration effects must be considered any time the beam has

been rocked to a position non-parallel to the optic axis (dotted lines in Fig. 3.19).

For the upper objective lens, Geiss has shown that spherical aberration causes the image of the C2 aperture on the specimen plane to shift a linear distance:

$$x = M C_s \theta^3 \quad (3.18)$$

where M is the demagnification of the C2 aperture, C_s is the coefficient of spherical aberration for the objective lens and θ is the angle of rock. M is computed in Chapter 5 to be 1/38X, C_s is 6.3 mm and the maximum angle of rock is approximately 1° . At this angle, the shift of the C2 aperture image would be approximately 90 \AA which causes no problem during the rocking beam process as the illuminated area defined by the C2 aperture is several microns in diameter.

However, the same equation can be used to determine the shift of the specimen image itself. This shift is much more crucial since it causes the specimen image to sweep across the detector, thus limiting the minimum area from which the pattern can be obtained. While the upper objective lens field reduces the shift of the illuminated area by 38X, the lower objective lens field increases the shift of the specimen image by 14X.

For a 1° rocking angle:

$$x = 14 (6.7 \text{ mm}) (.017 \text{ rad})^3 \quad (3.19)$$

$$x = 5000 \text{ \AA}$$

Thus, the minimum usable area needed for a transmission rocking beam

channeling pattern is approximately $1 \mu\text{m}$. However, note that the shift is much reduced at smaller rocking angles. If the maximum angle of rock is limited to 0.5° , λ is reduced to 620 \AA . Thus, channeling patterns out to about the second order diffraction spots can be produced with a very high level of accuracy.

An example of the shift of the image resulting from spherical aberration is shown in Fig. 3.20. It is important to realize that since transmission channeling patterns are found with the objective aperture removed, the current density striking the detector is much higher. Thus, the signal to noise ratio is much higher than any other type of microdiffraction pattern. If it were not for the effect of spherical aberration, transmission channeling would be a very powerful tool for extracting diffraction information from the specimen.

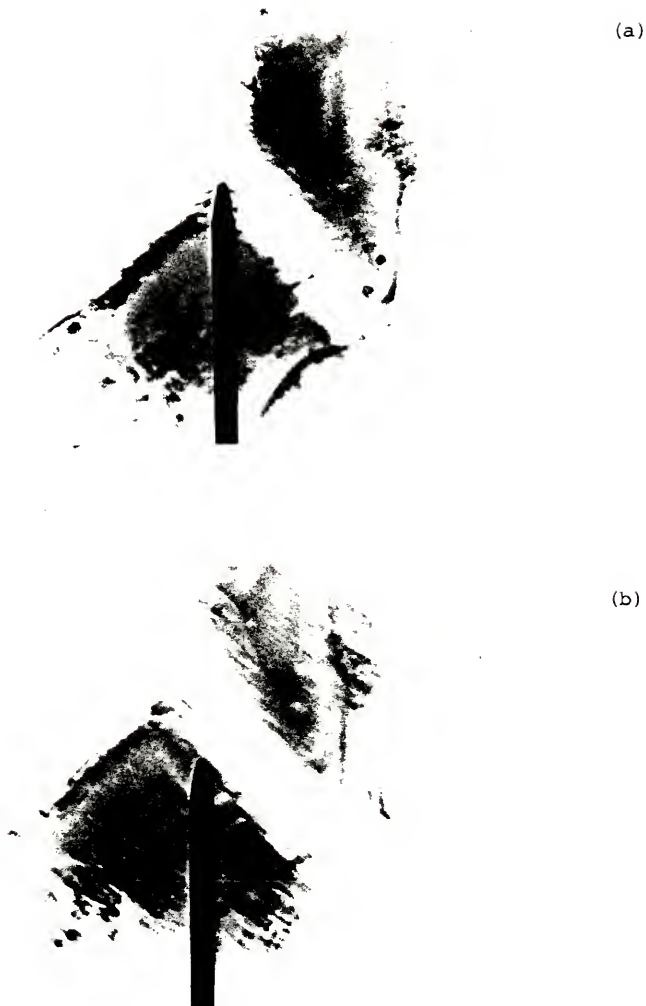


Figure 3.20 Image shift for rocking beam optics. At 40,000, sample image shifted approximately 3500 \AA , for a 1° angle of rock.

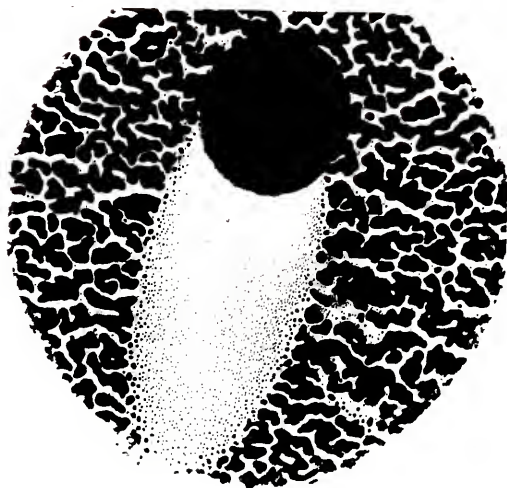
CHAPTER 4
EXPERIMENTAL PROCEDURES AND MATERIALS

4.1 Ray Optics and Computations

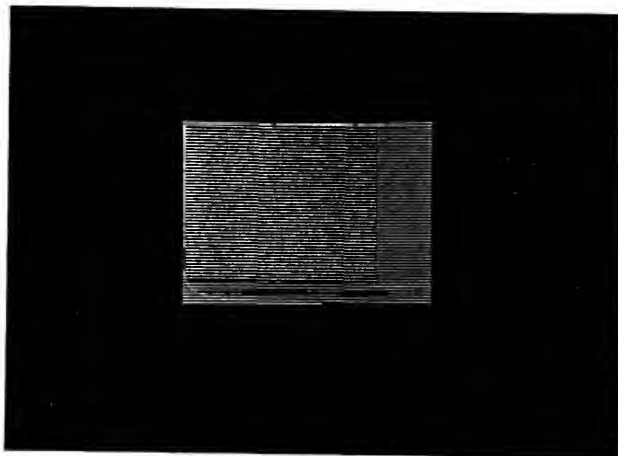
Since electron beam spot size and beam convergence determine the volume of the crystal producing the microdiffraction pattern, an experimental means of spot size measurement is of importance. Such a measurement may be performed directly in the Philips 301 by using the following procedure.

An easily observed sample is imaged at high magnification in the standard TEM mode and objects of appropriate size, such as the small gold particles in the interior of the shadowed region in Fig. 4.1a, are recorded photographically. Then, with the sample in place, the microscope is switched to standard STEM conditions. With the stationary STEM diffraction pattern in view, the diffraction lens strength is now changed such that a raster pattern formed by the flying spot is imaged on the TEM phosphor screen as shown in Fig. 4.1b. By adjusting the specimen height, both sample image and raster pattern can be brought into sharp focus and observed simultaneously. The spot size can now be measured by stopping the scan, removing the specimen, and comparing the spot image diameter to gold particle size.

When the intermediate lens is set at zero strength for the STEM mode, the magnification reading on the microscope panel is



(a)



(b)

Figure 4.1 Images taken with Philips 301 plate camera of 0.25 μm latex balls shadowed with gold (a) and the STEM raster pattern (b). The gold islands in the interior of the shadow range from 20 to 100 \AA in diameter.

incorrect, and the spot size can only be determined by comparison to the sample image. It is thus quite important that the beam cross-over and specimen are at the same height in the column, or errors in measurement will result.

Once this comparison is made, spot sizes, controlled by the first condenser (C1) lens, can be recorded for several C1 settings as shown in Fig. 4.2. Measured spot sizes are plotted versus the C1 lens current in Fig. 4.3 and the results compare closely to data published in the Philips STEM manual.

It is interesting to show how spot size measurements can be used to determine the characteristics of various lenses in the microscope column. Because spot size is controlled by the C1 lens alone in the STEM mode, increasing the lens current to reduce spot size must also reduce the C1 lens focal length. Since the object distance, O (in this case, the distance from the C1 lens to the gun cross-over), is fixed, only the image distance, I , changes with the C1 lens strength. The formula for magnification for a simple, "thin" lens is

$$M = \frac{I}{O} \quad (4.1)$$

Now, the thin lens formula relating focal length, f , to the object and image distance, O and I , is

$$\frac{1}{O} + \frac{1}{I} = \frac{1}{f}$$

By rearranging terms and substituting M can be defined in terms of the object distance and the focal length

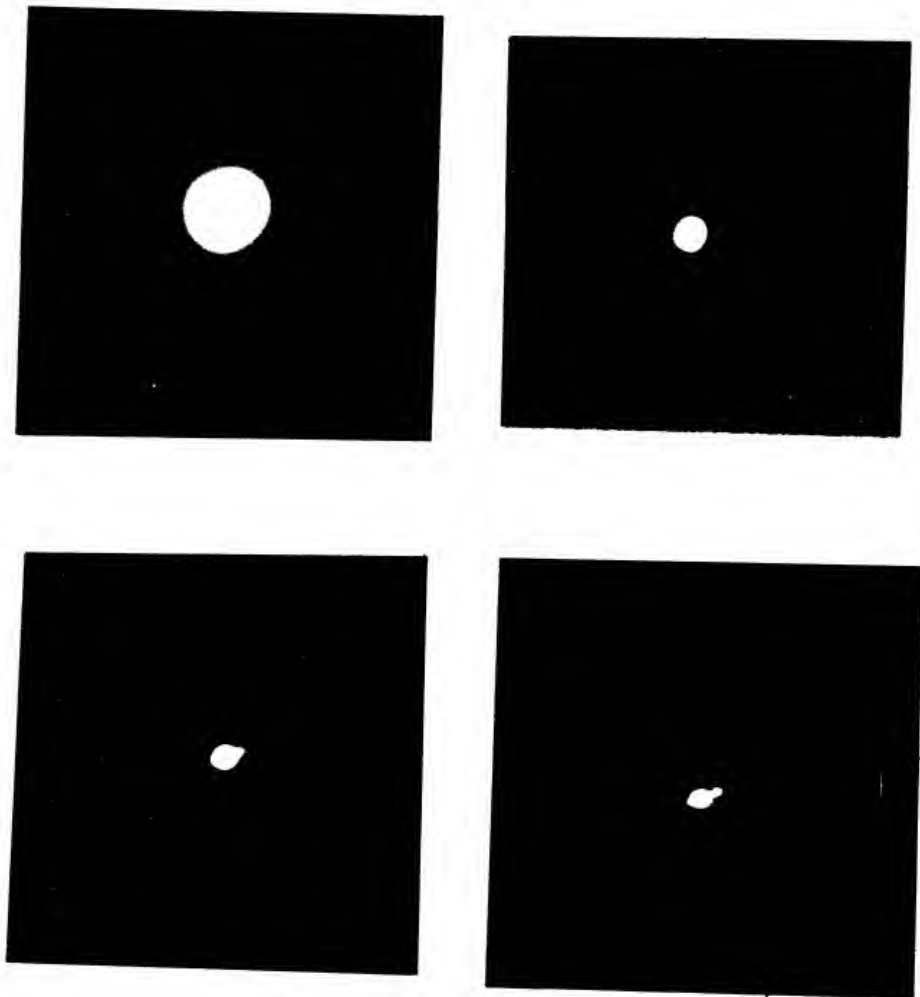


Figure 4.2 Plate camera images of the stationary STEM probe for four different settings of Cl, the first condenser lens. Magnification is 1,000,000X.

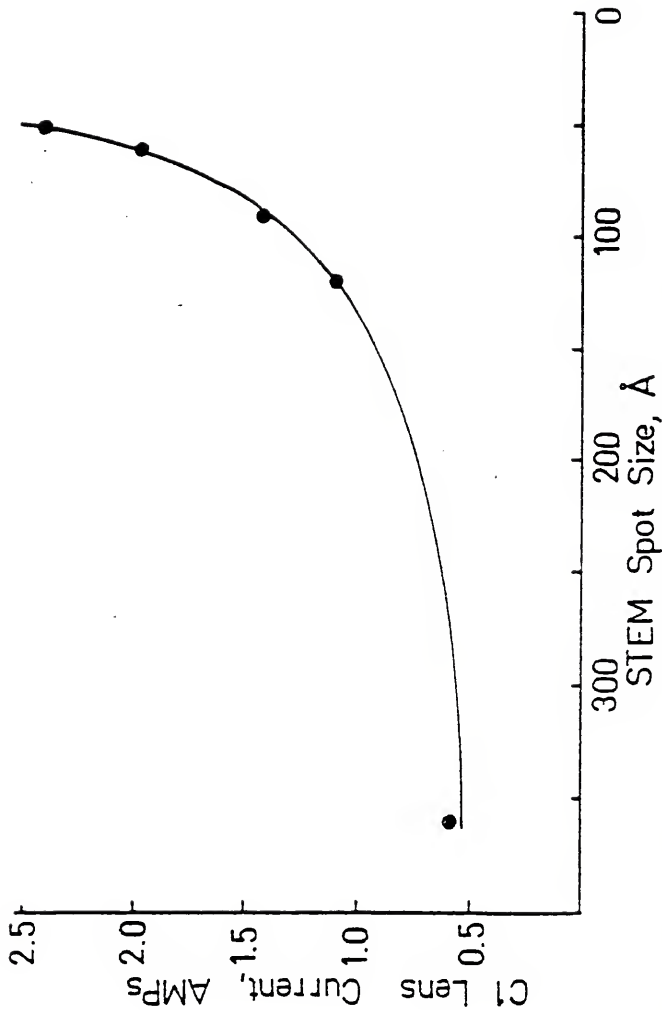


Figure 4.3 STEM spot size is determined by the de-magnification factors of the C1 and the upper objective lens. The experimental values obey a parabolic relationship described by Eqn. 4.6.

(4.3)

$$M = \frac{f}{f-0}$$

In the STEM mode with the C2 lens turned off, the spot size (ignoring aberrations) at the specimen plane is found by multiplying the demagnification factors of the C1 and objective (OBJ) lens times the original spot size, d_0 , of the gun cross-over:

(4.4)

$$d = M \times M_{\text{OBJ}} \times d_0$$

Except for minor focusing corrections, M_{OBJ} remains fixed for any spot size. Also, the C1 lens, being of relatively long focal length, can be considered thin and the focal length of C1 can be related to the lens current (Lifshin, 1969):

(4.5)

$$f = K \frac{V}{(NI)^2}$$

where K is a constant, V the accelerating voltage, and NI the number of ampere turns. By substituting Eqns. 4.5 and 4.3 into 4.4, an equation relating the spot size to C1 lens current can be obtained:

(4.6)

$$d = \left[1 - \frac{0(NI)^2}{KV} \right] M_{\text{OBJ}} d_0$$

Since M_{OBJ} is known (see Chapter 3), the spot size can be computed and compared to the experimental values in Fig. 4.3.

As discussed in Chapter 3, the beam convergence angle, or the incident semi-angle, α_1 , directly controls the angular resolution of the microdiffraction pattern. For both TEM and STEM convergent beam diffraction modes, α_1 is determined by the ratio of the diffraction

disc diameter to the Bragg angle as derived in Chapter 3:

$$\alpha_i = \frac{\theta_B y}{x} \quad (4.7)$$

For STEM, α_i is determined solely by the second condenser (C2) aperture size and can be computed by measuring x and y from diffraction patterns such as those shown in Fig. 4.4. The convergence angle is linearly proportional to the C2 aperture diameter so a plot of α_i versus aperture size should be linear as shown in Fig. 4.5. Errors can result both from measurement of diffraction disc diameters as well as from actual aperture diameters that differ by as much as 20% from the stated size. When high accuracy is needed, the best method is to measure the aperture in a scanning electron microscope. For the range of aperture sizes shown, a 10 μm diameter was found to present the best compromise between a highly collimated probe and enough current density to portray a diffraction contrast image on the STEM CRT with an acceptable signal-to-noise ratio. The 10 μm aperture, with $\alpha_i \approx 10^{-3}$ rad, easily satisfies Maher and Joy's criterion for Δw , and thus produces a STEM image very similar to a TEM image formed with a well-collimated beam.

For the TEM convergent beam mode, where the C2 lens remains on, calculation of α_i remains exactly the same as for STEM, but control of convergence is accomplished by changing either the C2 aperture size or the C2 lens strength. For this case, convergence is controlled by using the C2 lens to place the beam cross-over above or below the upper focal plane of the upper objective lens. When the C2 cross-over is set exactly at the upper focal plane of the objective lens,

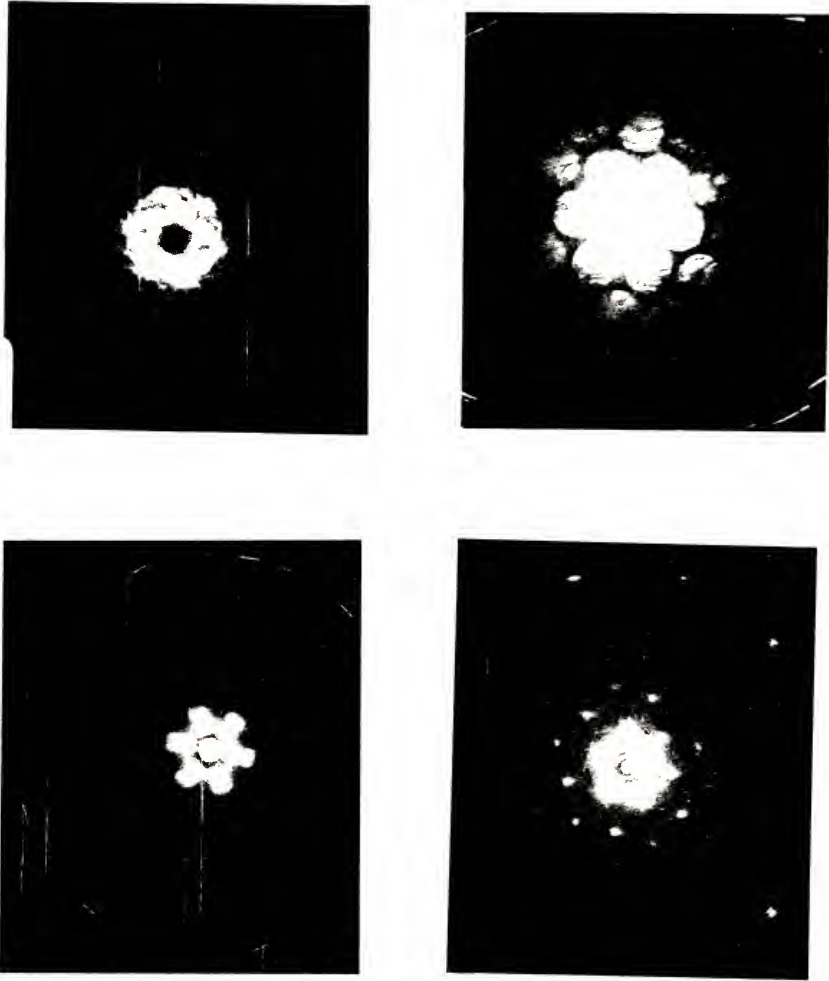


Figure 4.4 Convergent beam diffraction patterns (STEM mode) for the $\langle 111 \rangle$ direction in silicon. As the C2 (second condenser) aperture size decreases in diameter, the angular resolution of the diffraction pattern improves in linear proportion.

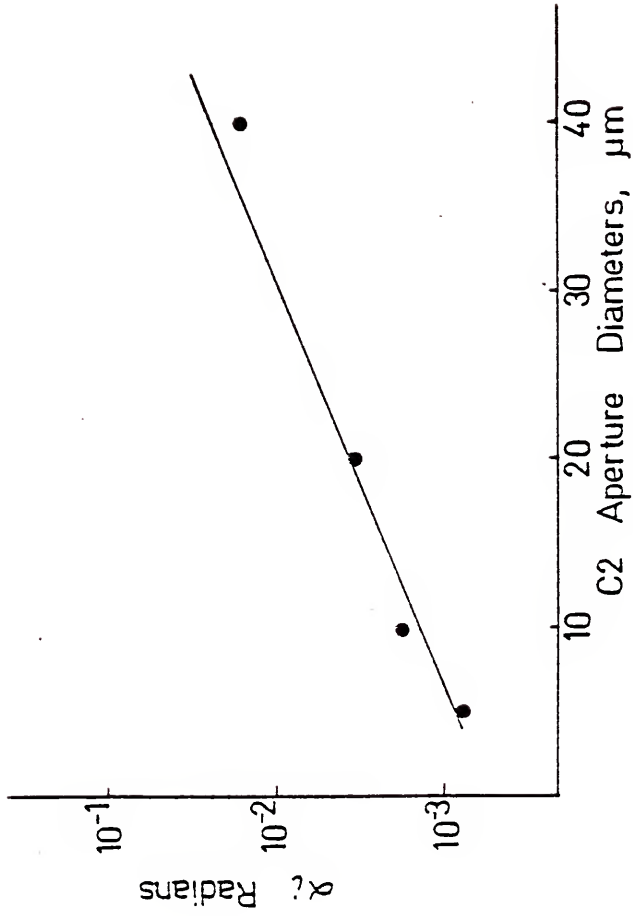


Figure 4.5 The semi-angle of the incident beam, α_i , can be calculated from Eqn. 4.7 and is linearly proportional to the C2 aperture diameter.

a large area of the specimen is illuminated with a well-collimated beam. However, if C2 is now defocused sufficiently that the crossover would lie before the plane of the upper objective lens, a ray path such as that shown in Fig. 3.9b occurs, producing a focused spot at the specimen plane. Thus, once C2 has been used to focus the spot for microdiffraction, α_i is fixed and can be adjusted only changing the C2 aperture size as is done in the STEM mode.

These principles are illustrated in Fig. 4.6. Twelve microdiffraction patterns were taken with the same series of C2 lens settings for three different aperture sizes. Then, the calculated convergence was plotted versus C2 lens current. Although the C2 lens control can be used to vary α_i , only one setting corresponds to the focused spot. If the angular resolution in the diffraction pattern is insufficient for a given C2 lens strength, the only remaining alternative is to use a smaller C2 aperture.

As discussed in the last chapter, resolution for the rocking beam microdiffraction pattern is controlled by the diameter of the objective aperture. Using the formula of Geiss, the angular resolution is

$$\rho = d/f_{\text{OBJ}} \quad (4.8)$$

For the STEM polepiece, $f_{\text{OBJ}} = 3.7$ mm and the objective aperture size, d , can range from 5 to 50 μm . Fig. 3.18 shows rocking beam patterns for objective sizes of 5, 20, 50, and no aperture, respectively. The angular resolution of the pattern is directly proportional to the size of the diffraction disc formed on the CRT and

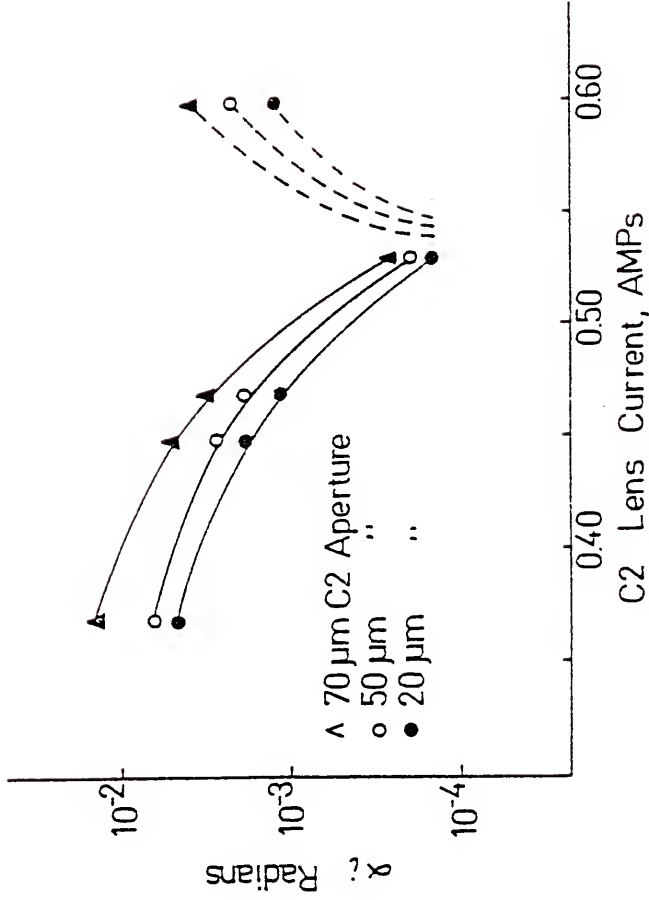


Figure 4.6 For the TEM mode, α_1 reaches a minimum when the C2 cross-over is set at the front focal plane of the objective lens. For any given C2 current setting, substitution of a smaller C2 aperture will always reduce α_1 .

Eqn. 4.7 can be used to find ρ . Plotted values of ρ versus objective aperture diameter are shown in Fig. 4.7, and the diffraction disc diameter can also be plotted versus diameter on the same graph. If the objective aperture diameters are precise, the slope of the curves should be the same.

4.2 Sample Preparation

The equipment needed to produce stacking faults in silicon consists of a standard metallurgical tube furnace and the accompanying apparatus necessary to force steam over the samples at a controlled rate. As shown in Fig. 4.8, a "steam bubbler" was constructed by connecting a 500 ml Erlenmeyer flask to a Vycor tube lying in the furnace cavity. Distilled water in the flask was then maintained at 99°C and heating tape was used to prevent any condensation in the coupling between the flask and the furnace tube. A Teflon boiling chip placed in the bottom of the flask aided bubble formation and encouraged the steam to flow through the hot zone at an essentially constant rate. For a typical temperature of 1100°C, the steam bubbler consumed approximately 100 ml of water per hour.

Since the growth rate of the standing faults is quite temperature sensitive, samples were placed on a Vycor spatula that was carefully set in exactly the same position in the furnace tube to insure reproducibility from one run to another. Both temperature and time could be checked by noting the color of the oxide film found on the silicon sample at the completion of the run. It has been shown (Runyan, 1965) that the oxide color is the result of

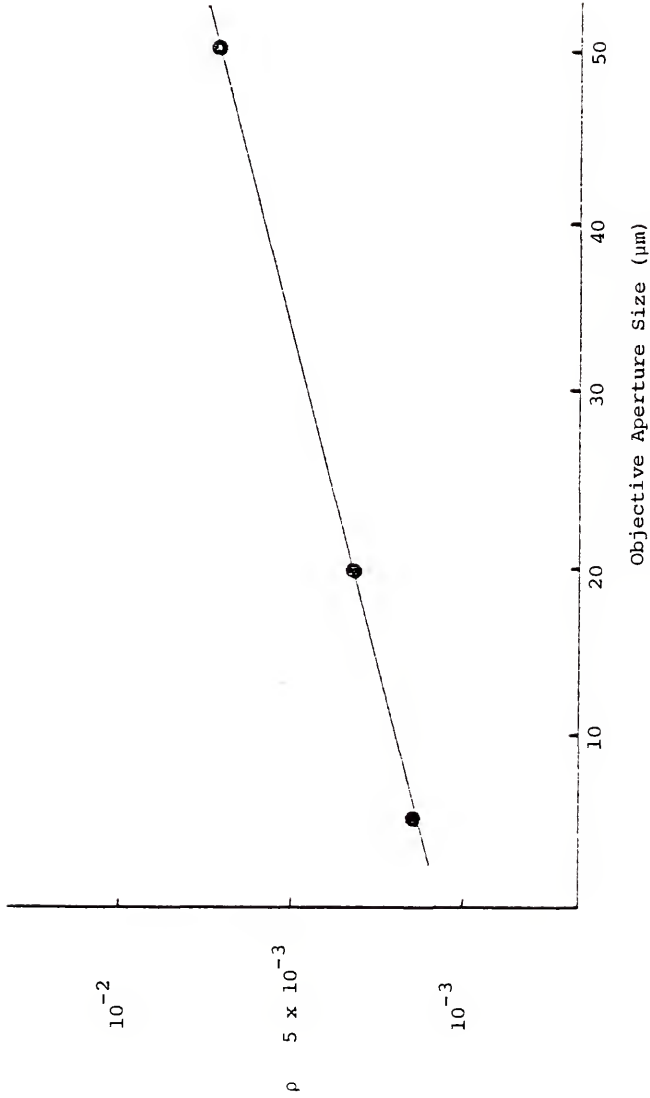


Figure 4.7 The angular resolution in the rocking beam diffraction pattern, P , is calculated from Eqn. 4.8. Angular resolution is proportional to the objective aperture diameter just as α_i for the convergent beam modes is proportional to the C2 lens strength and the C2 aperture diameter.

optical interference, and that the color is an accurate indication of the oxide thickness. Runyan's results show that a bright green film at 1100°C should be equivalent to a 5000 Å layer. Forty-five minute annealing times were found to consistently produce a green oxide layer, and, if the sample was first abraded with diamond paste, generous numbers of stacking faults.

Starting material for the oxidation experiments consisted of silicon wafers that were mechanically polished on one side to a mirror finish. Undoped, or intrinsic, material was supplied by the Ventron Corporation, while 1 Ω -cm n-type material was obtained from the Wacker Chemical Corporation. All wafers were scored with a diamond cutter and then broken into 3 mm squares, a size that fits conveniently in the Philips 301 double-tilt holder. To insure that all contaminants were removed before heat treatment, the individual squares were washed in sulfuric and nitric acids, methanol, and finally rinsed in deionized water.

The polishing procedure used for electron microscopy must produce a thin region less than 0.5 μ m below this surface. This is accomplished with a chemical polishing procedure that removes material from the back side of the sample while the polished side is protected with a wax mask.

The appearance of the sample cross-section is diagrammed in Fig. 4.9. First, the oxide layer is removed by placing the sample in hydrofluoric acid for five minutes and the sample is rinsed in deionized water. The sample is then placed polished side down on a 5 mm square glass cover slide, and both glass and specimen are

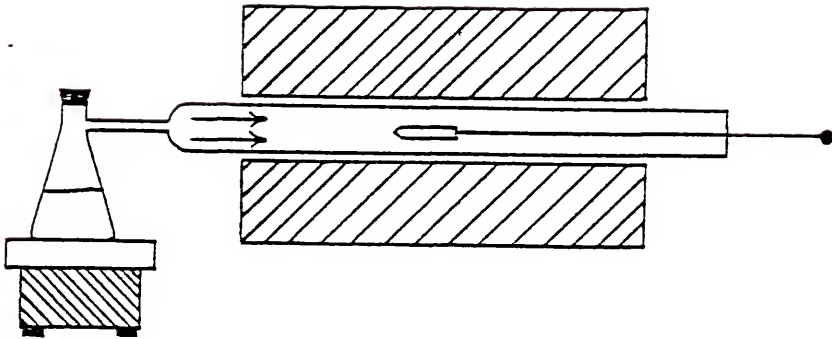


Figure 4.8 Apparatus used to grow extrinsic stacking faults in silicon.

completely coated with liquid beeswax and allowed to cool until the wax has hardened. The wax is then scraped away from the center of the nonpolished specimen side such that about one-third of the area is exposed.

This assembly is then placed in a plastic beaker containing 10 ml of solution of 3 HF:5 HNO₃:3 HAC. Only the HNO₃ actually attacks the silicon surface, but it must be used in combination with HF, which attacks the SiO₂ layer that would otherwise reform and halt the polishing process. HAC, or acetic acid, plays no active role in polishing but acts as a buffering agent to control the pH of the solution (Booker and Stickler, 1962).

After approximately five minutes of chemical etching a polished depression that extends approximately one-third of the way into the sample appears. Although the step could be allowed to proceed to completion, it was found that this formed a hole with sides so steep that the thin area varied rapidly in thickness and was too small to be of use for electron imaging. If, however, additional wax was scraped away such that two-thirds of the sample surface is exposed after the first depression was made, and the sample was reimmersed in the polishing solution, the depression had much shallower sides. The electron-transparent region in the center was often 0.5 mm across and was of nearly constant thickness.

The exact point at which to stop the process is of crucial importance. If carried on too long, the thinnest area is consumed before the solution can be rinsed away. If stopped too soon, the process cannot be restarted without clouding the mirror surface of

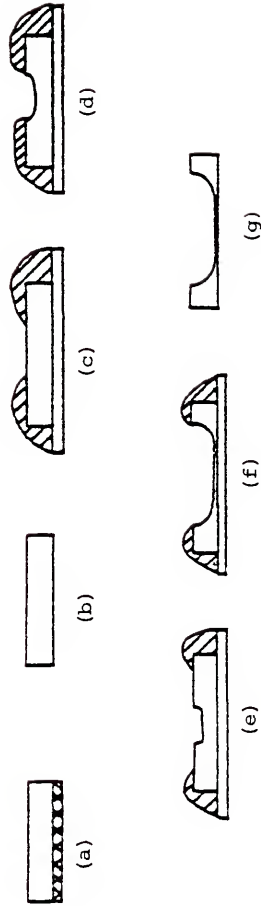


Figure 4.9 Cross section of silicon sample during preparation of thinned region for electron microscopy. The stages are: (a) grow oxide film in furnace; (b) remove oxide in HF; (c) apply protective wax coating; (d) etch away central depression; (e) remove additional wax to expose more surface area; (f) thin to electron transparency; and (g) remove wax and clean.

the polished region, as it takes several seconds for equilibrium polishing conditions to be re-established. However, as noted by Booker and Stickler (1962), silicon sections thinner than 0.5 μm are optically transparent and appear pale yellow in transmitted light. Such a thickness is easily penetrated by 100 KV electrons. Thus, the final stage of polishing was completed by placing the beaker containing the waxed sample over a piece of frosted glass and observing it through a microscope with transmitted light. As the sample is thinned, it becomes transparent in the center, changing in hue from deep red to pale yellow. At the appropriate instant, the polishing process was stopped by quenching the entire contents of the beaker into 1000 ml of distilled water.

The wax was then dissolved in warm trichlorethylene and the sample cleaned in several rinses of absolute methanol and deionized water. Finally, the sample was glued in the Philips double-tilt holder with a colloidal graphite solution.

4.3 The Character of the Dislocations Introduced

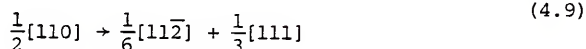
Crystal defects introduced into silicon by the methods of the preceding section have been widely studied, and a consensus has begun to emerge on how nucleation, growth, and annihilation of these defects occur. The primary kinds of defects, extrinsic stacking faults surrounded by partial dislocations of Burger's vector $\frac{1}{3} \langle 111 \rangle$, are shown in Fig. 4.10. The stacking faults apparently form at stress concentrations near scratches in the original abraded specimen surface and grow in front of the SiO_2 -Si interface that gradually advances into the silicon matrix during oxidation.



Figure 4.10 Extrinsic stacking faults in silicon grown from a polished surface abraded with diamond paste. The specimen is approximately $0.7 \mu\text{m}$ thick. The curved partial dislocation surrounding the fault is pure edge in character and does not intersect the bottom surface of the foil.

The actual nucleation method of the partial is in dispute.

One possible mechanism is the dissociation of a perfect dislocation into a Shockley and a Frank partial (Booker and Tunstall, 1966):



where the Frank partial would be free to undergo climb and create the extrinsic stacking fault. However, the reaction is not energetically favorable and it is doubtful that it actually occurs. A more probable nucleation mechanism (Mahajan, 1976) involves the diffusion of oxygen atoms supplied by the SiO_2 oxide layer to form Si-O complexes on $\{111\}$ planes which compress the adjoining lattice along the $\langle 111 \rangle$ directions. The silicon atoms displaced by the oxygen can now "plate out" to form an additional (111) plane that forms an extrinsic stacking fault bounded by a $\frac{1}{3}[111]$ dislocation. As this process continues, additional interstitials diffuse to the core of the bounding partial dislocation, and the stacking fault increases in area by climb of the bounding partial. This method explains how a perfect, single atomic plane of SiO_2 could be created in the diamond cubic silicon lattice. Further evidence in support of this model is supplied by Ravi (1974), who showed that stacking faults in wafers with surfaces normal to $\langle 112 \rangle$ preferentially nucleated on the $(11\bar{1})$ and $(1\bar{1}1)$ plane. Both of these planes lie at an angle of 62° to the surface, and have the greatest resolved shear stress of the $\{111\}$ -type planes. On the other hand, when the wafer surface is not abraded, faults preferentially grow on (111) planes that are at the shallowest angle to the

surface since it is the closest to the oxide-matrix interface, the source of excess interstitials necessary for growth. In the specimens used in this study, with a [111] surface normal, the $(11\bar{1})-(1\bar{1}1)-(11\bar{1})$ planes all make equal angles with the surface, and the density of faults is the same.

The growth rates of individual faults was found to obey an Arrhenius relationship (Murarka, 1976):

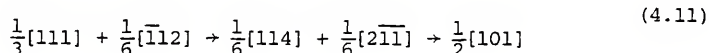
$$L = At^n \exp(-Q/KT) \quad (4.10)$$

where $n = .85$ eV and $Q = 2.55$ eV. This equation was found to hold in both n-type and p-type materials. However, the density of faults was on an order of magnitude higher in n-type material.

Once the faults reach a length of several microns, additional annealing in vacuum or extended oxidation treatments (Ravi, 1974) result in the annihilation of the stacking faults and the formation of perfect $\frac{1}{2}\langle 110 \rangle$ dislocations.

In this mechanism, the faults shrink by an exact reversal of the process discussed for fault growth. Here, oxygen could diffuse away from the fault plane, leaving vacancies with the silicon lattice to interact with the partial dislocation core and shrink the extra plane by positive climb.

Faults can also be destroyed by dislocation reactions, such as a process involving the nucleation and passage of two Shockley partials over the extra fault to remove the faulted layer. A possible reaction is



This reaction leaves the remains of a perfect dislocation. Only this unfauling reaction leads to the formation of perfect $\frac{1}{2}\langle 110 \rangle$ dislocations. The strong tendency of the perfect dislocations to lie along $\langle 110 \rangle$ directions is caused by the large Peierls force in diamond cubic materials (Hirth and Loethe, 1968). The Peierls force is the tendency of dislocations to minimize their line energy by lying along certain preferred directions in the crystal lattice.

In summary, defects produced by the annealing treatments discussed above result in extrinsic stacking faults bounded by partial edge dislocations with a Burgers vector $\bar{b} = \frac{1}{3}\langle 111 \rangle$. These directions are sessile and move only by climb. Upon much longer anneal times, an unfauling reaction results in a reduction in fault density and the formation of numerous perfect dislocations where the Burgers vector is either parallel to, or lies at a 60° angle from, the dislocation line.

4.4 Determination of Crystal Directions by Diffraction Patterns

Identification of crystal defects can proceed only when the orientation between defect, diffracting plane, and electron beam has been precisely determined. In particular, the dislocation line direction, specimen foil normal, and electron beam direction must be repeatedly calculated for every two-beam condition. To proceed, a series of diffraction experiments is performed as in Fig. 4.11, where a two-beam image of a defect is shown with its associated selected area diffraction pattern. The exact beam direction, expressed in hkl coordinates, can be found by measuring the relative positions



Figure 4.11 Extrinsic stacking fault in silicon and selected area diffraction pattern from surrounding area. After correction for rotation of the image due to the lenses, the \bar{g} vector ($\bar{g} = \langle 111 \rangle$ for the $\langle 112 \rangle$ pole) can be drawn on the image as shown. The angle between the partial dislocation direction, \bar{u} , and \bar{g} can then be measured directly on the photograph.

of Kikuchi line pairs on the diffraction pattern. Once the exact beam direction for a particular two-beam condition is found, the projection of the defect line direction in the image plane (i.e., the actual dislocation image, seen in Fig. 4.11a is used in conjunction with the beam direction and the \bar{g} vector to compute the actual defect line direction and the specimen foil normal.

The beam direction will be needed in subsequent calculations and must be computed first. Consider the orientation shown in Fig. 4.12 between \bar{g} , the two-beam diffraction vector, \bar{B} , the true beam direction defined as anti-parallel to the electron beam, and \bar{A} , the low-index pole direction that is determined by inspection from the diffraction pattern. It can be seen that \bar{B} must be perpendicular to \bar{g} , and that \bar{A} and \bar{B} must be separated by δ , the angle of tilt necessary to produce the two-beam condition. Since the center of the Kikuchi pattern can be thought of as rigidly attached to the crystal, δ is proportional to the linear distance from the main beam position to the Kikuchi pattern center. Since the distance between each Kikuchi pair is proportional to $2\theta_B$, δ is proportional to $X/2\theta_B$ where X is the distance drawn from the main beam to the Kikuchi pattern center.

The vectors \bar{A} , \bar{g} , and $\bar{g} \times \bar{A}$ form a right-handed coordinate system. Since \bar{B} is perpendicular to \bar{g} , it must lie in the plane formed by \bar{A} and $\bar{g} \times \bar{A}$ at δ degrees away from \bar{A} . If \bar{A} and $(\bar{g} \times \bar{A})$ are assigned unit lengths, we can thus write the equation for the true beam direction as

$$\bar{B} = |\cos \alpha| \bar{A} + |\cos(90^\circ - \alpha)| \bar{g} \times \bar{A} \quad (4.12)$$

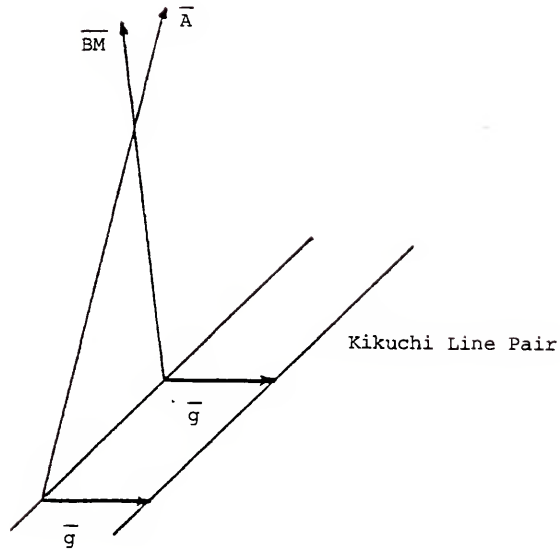


Figure 4.12 Angular relation between the two-beam direction, \bar{BM} (determined from measurement of Kikuchi line pairs), and \bar{A} , the low index pole direction. Both \bar{BM} and \bar{A} are assumed perpendicular to the \bar{g} vector.

With \bar{B} computed for two different two-beam images, we then use Fig. 4.13 to compute the defect line direction, \bar{u} . For both of the two-beam images, the projected directions, \bar{u} and \bar{p} , are co-planar with the \bar{g} vector used in each case. If the acute angle between \bar{p} and \bar{g} is measured and a coordinate system of \bar{B} , \bar{g} , and $\bar{g} \times \bar{B}$ is formed, then \bar{p} is

$$\bar{p} = |\cos \beta| \bar{g} + |\cos(90^\circ - \beta)| (\bar{g} \times \bar{B}) \quad (4.13)$$

As shown in Fig. 4.13, each \bar{p} and its associated beam direction, \bar{B} , forms a plane. The normals to each of the planes are

$$\begin{aligned} \bar{n} &= \bar{p} \times \bar{B} \\ n' &= \bar{p}' \times \bar{B}' \end{aligned} \quad (4.14)$$

Now, the interactions of the planes must be the dislocation line directions, so \bar{u} is the cross product of the two normals.

$$\bar{u} = (\bar{p} \times \bar{B}) \times (\bar{p}' \times \bar{B}') \quad (4.15)$$

The foil normal computation is an extension of the computation for the line direction. To proceed, the directions of two lines drawn from mid-point to mid-point of three conveniently spaced dislocations are computed by the preceding methods. This forms a triangle whose surface is perpendicular to the foil normal. If two edges of the triangle are labeled \bar{C} and \bar{D} , then the foil normal is again found by computing the cross product:

$$\bar{F} = \bar{C} \times \bar{D} \quad (4.16)$$

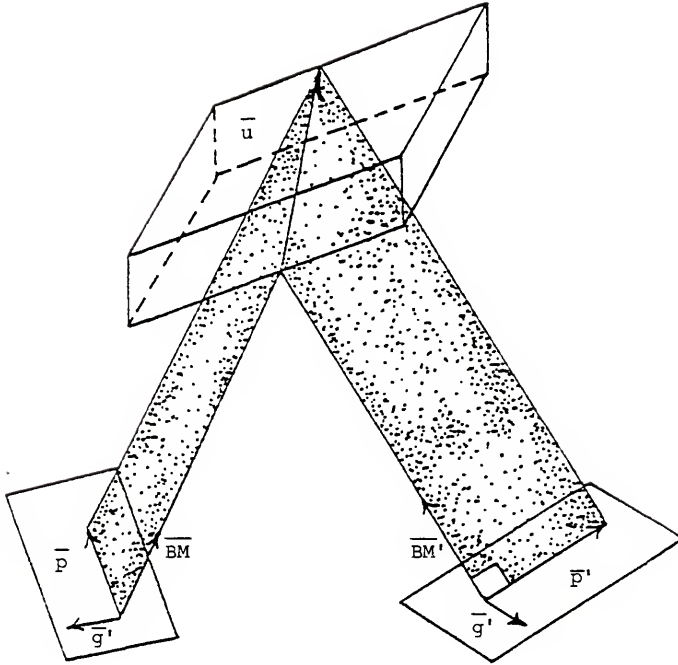


Figure 4.13 The dislocation image, as recorded by the plate camera on the STEM CRT, is a projection along the beam direction to a plane containing the \bar{g} vector. The projected directions \bar{p} and \bar{p}' form planes with their associated beam direction that intersect at \bar{u} , the actual dislocation line direction.

CHAPTER 5
EXPERIMENTAL RESULTS

5.1 A Comparison of the Microdiffraction Methods

It should be apparent that there is considerable overlap among the various microdiffraction techniques and there are often several possible choices to extract information from a crystalline specimen. The methods themselves can be roughly categorized according to ray optics. In the table below, the four basic methods are compared to standard selected area diffraction techniques.

Table 5.1
Microdiffraction Methods

Method	Ray Optics	Angular Resolution	Minimum Area from Which Diffraction Pattern is Formed
Selected Area Diffraction	Std. TEM conditions	$\approx 5 \times 10^{-4}$ rad	2 μm
Focused C2 Aperture	Std. TEM conditions	$\approx 5 \times 10^{-4}$ rad	1320 \AA
STEM	C2 and INT lenses turned OFF	10^{-3} to 10^{-2}	50 \AA
Focused TEM Spot	All lenses ON, focus spot with C2	10^{-3} to 10^{-2}	400 \AA
Rocking Beam	Std. TEM conditions except beam rocked over sample	5×10^{-4} to 10^{-2}	$\sim 400 \text{\AA}$

It would seem all of the methods are capable of producing patterns from very small areas with a reasonable degree of angular resolution. In addition, the rocking beam and all focused spot techniques are capable of producing high quality transmission channeling patterns from an area approximately 2000 \AA in diameter.

Nevertheless, the quality of the results obtained by the different methods can vary widely, particularly with regard to the signal-to-noise ratio in the pattern, sample damage, and time spent in obtaining acceptable results. The following examples in this section are used to demonstrate the advantages and disadvantages of the methods listed in the table.

Certainly the easiest method of obtaining microdiffraction patterns is the focused C2 aperture technique. Illumination of the sample is the same as the imaging mode and the condenser lenses do not have to be adjusted to obtain the pattern. Although the minimum area is rather larger than the other methods, angular resolution is just as good as selected area diffraction and the contamination problems of the focused spot techniques are avoided.

One drawback of the focused C2 aperture approach is that the sample must be raised for both the image and the aperture edge to be sharply in focus. The specimen position is then non-eucentric, that is, it cannot be tilted with the goniometer stage without the image sweeping rapidly out of the field of view. For the STEM polepiece with the Philips 301, however, the focusing points for specimen and aperture nearly coincide and diffraction patterns can be obtained

from the eucentric position if one is willing to allow a slight fuzziness in the shadow image of the C2 aperture.

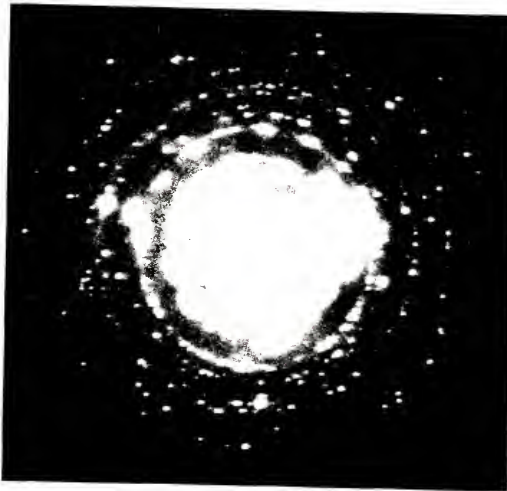
Examples of microdiffraction patterns produced by this technique are shown in Figs. 5.1 to 5.3 which compare patterns taken with Selected Area Diffraction (SAD) techniques to the focused C2 aperture method. In Fig. 5.1, a polycrystalline gold foil with an average grain size of $0.5 \mu\text{m}$ was imaged (Fig. 5.1a) and the pattern recorded for a $20 \mu\text{m}$ SAD aperture. Diffraction patterns using an aperture less than $20 \mu\text{m}$ in diameter would be useless due to spherical aberration, so standard techniques were not sufficient to produce single crystal diffraction patterns (Fig. 5.1b).

The size of the $20 \mu\text{m}$ in the SAD position was recorded with the plate camera (Fig. 5.2). The same aperture was then transferred to the C2 aperture position and the image again recorded. By comparing the diameters of the aperture in the two positions with the plate magnification it was found that the objective lens pre-field de-magnified the aperture by a factor of 38, while the lower half of the objective lens magnified by a factor of 14. The illuminated specimen area was thus 5200 \AA for the $20 \mu\text{m}$ C2 aperture and single crystal diffraction patterns were easily recorded.

Although the pattern is crisp with good angular resolution (Fig. 5.3a), note that Kikuchi lines are very difficult to distinguish. This effect, characteristic of high atomic materials, means that the crystal structure can be identified but the exact electron beam specimen orientation cannot be determined. This problem can be overcome only by using one of the focused spot microdiffraction techniques.



(a)



(b)

Figure 5.1 Image of polycrystalline gold foil and a selected area diffraction pattern obtained from a 20 μm aperture in the SAD position.

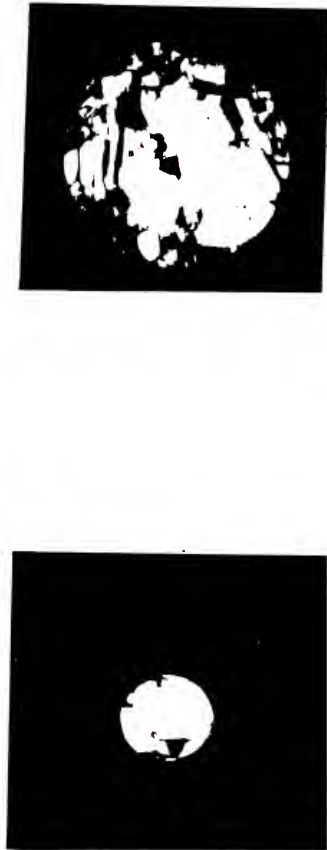


Figure 5.2 Size of the focused images of the C2 aperture and the diffraction aperture at the specimen plane. Aperture diameter is 20 μm for each case.



(a)

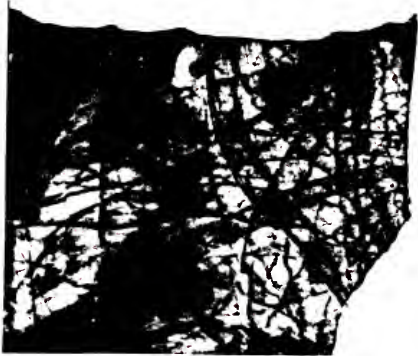


(b)

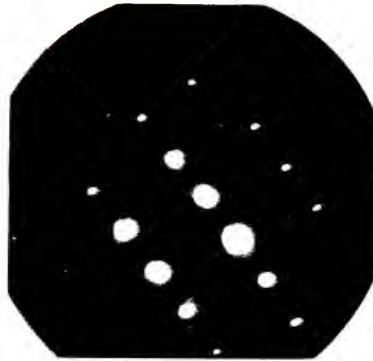
Figure 5.3 Microdiffraction patterns from polycrystalline gold foil with a focused 20 μm C2 aperture (a) and the focused TEM spot convergent beam (b) where the probe diameter was 200 \AA .



Figure 5.4 Transmission channeling pictures from polycrystalline gold foil. Spot size was 400 \AA and the C2 aperture diameter was $300 \text{ }\mu\text{m}$.



(a)



(b)



(c)

Figure 5.5 Polycrystalline molybdenum is imaged in (a). As is characteristic of high atomic number materials, the SAD patterns show few Kikuchi lines.

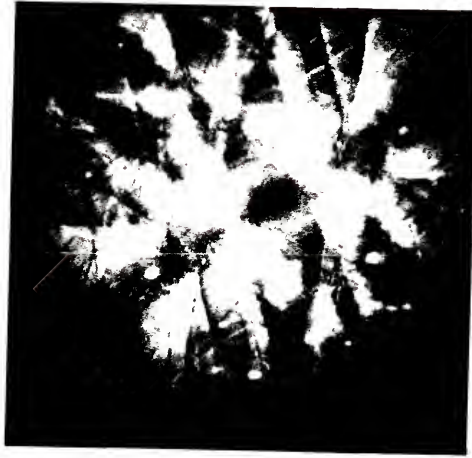
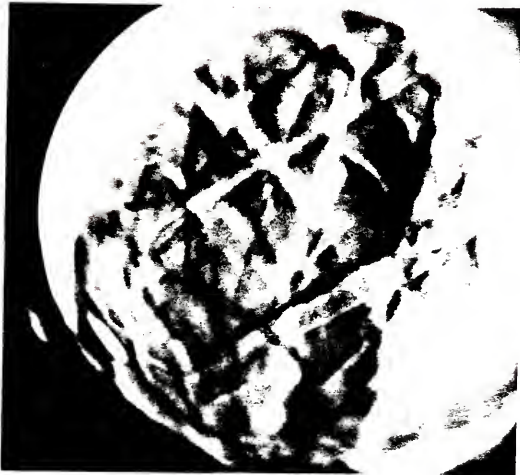
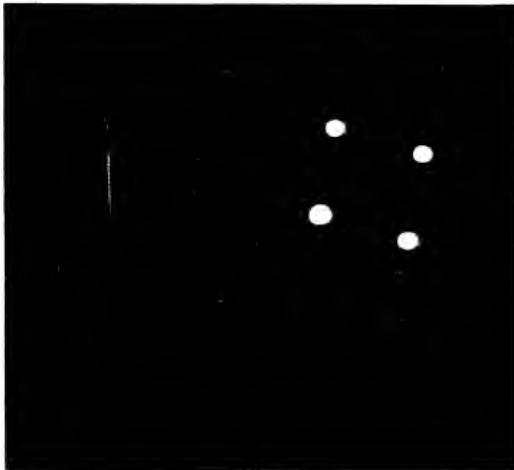


Figure 5.6 Double exposure of molybdenum transmission channeling patterns and selected area diffraction patterns shown on previous page.



(a)



(b)

Figure 5.7 Channeling pattern produced by rocking beam compared with a rocking beam microdiffraction pattern from the same area. No aperture was used for (a) while a 20 μm aperture was used for (b).

In Fig. 5.3b, for example, C1 is adjusted to reduce the spot size to approximately 1000 \AA and channeling lines begin to appear. The low index pole position can now be computed (using the methods of Chapter IV) with precision. If α_i is increased with a larger C2 aperture the complete transmission channeling pattern appears as shown in Fig. 5.4. Since α_i is now much greater, the channeling pictures are produced at the expense of much greater spherical aberration which distorts the edges of the image. Nevertheless, spherical aberration is still sufficiently low that channeling patterns from single grains less than 0.5 \mu m areas are achievable.

One interesting modification of focused spot TEM microdiffraction is to record a diffraction spot pattern using either focused spot or SAD methods, and then directly compare it with channeling information by making a double exposure from two separate negatives.

This method was used for a molybdenum foil, where it is again difficult to produce Kikuchi lines (Fig. 5.5). The exact beam direction for diffraction patterns with as little as 3 or 4 excited reflections can now easily be determined with the aid of the channeling lines (Fig. 5.6).

The results for molybdenum can be duplicated with the rocking beam procedure for approximately the same areas needed to produce a pattern. In Fig. 5.7, two rocking beam patterns were taken with a 10 \mu m objective aperture (Fig. 5.7b) and the objective aperture removed (Fig. 5.7a). The images are noisier than those obtained from

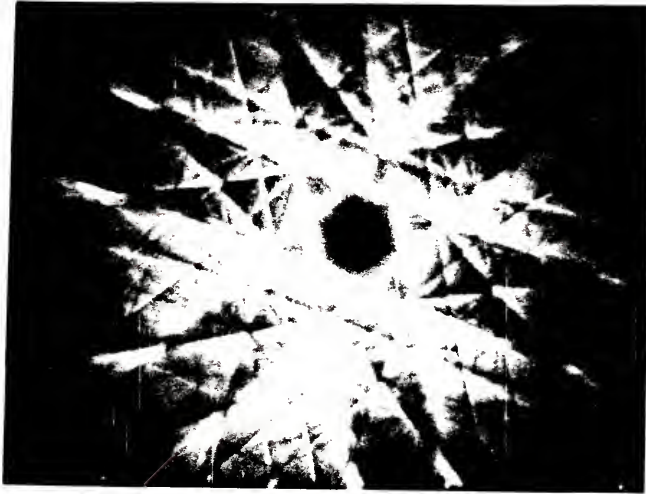
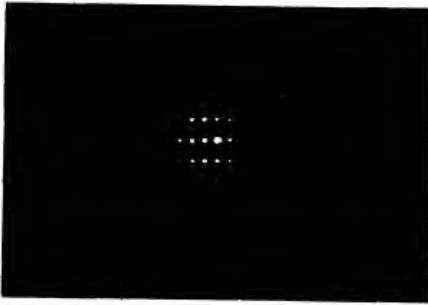
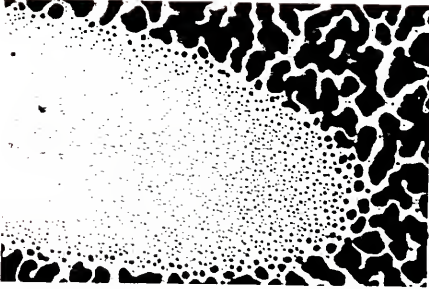
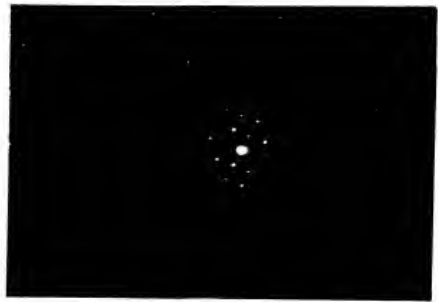


Figure 5.8 Transmission channeling patterns from (111) direction in silicon produced by rocking beam technique with objective aperture removed.

<013>



<112>



<011>

Figure 5.9 STEM microdiffraction patterns from gold islands ~ 200 Å in diameter.

the focused spot procedure but contamination was minimal since the beam remains defocused for rocking beam. The "noisiness" of the image formed on the CRT is a constant problem with this method, but high quality results (Fig. 5.8) can still be obtained for thin sections or low atomic materials such as silicon that are more transparent to the electron beam.

If diffraction patterns from areas less than 400 \AA must be obtained, STEM methods that form the image on the CRT and record the microdiffraction pattern with the plate camera is the only possibility. With the STEM polepiece, spot sizes as small as 30 \AA can be used and, since beam spreading should involve only inelastically scattered electrons, diffraction patterns from a column of crystal of approximately the same diameter can be recorded. Although angular resolution can be quite high if a C2 aperture of 10 \mu m diameter is used, the intensity of the pattern may be quite low. High beam current densities, fast emulsions, and long exposure times may help to overcome these limitations but contamination and drift of the probe due to electronic instabilities are continuing problems.

Probably the best aid to good results is using a very short camera length so that the entire diffraction pattern is concentrated in the center of the negative. With this procedure, exposure times for a 50 \AA STEM probe can be less than 1 second, much reducing probe drift and specimen contamination. Three excellent examples are shown in Fig. 5.9, where easily recognizable $\langle 011 \rangle$, $\langle 112 \rangle$, and $\langle 103 \rangle$ patterns were produced from gold islands formed by vapor deposition on a formvar film. The quality of these images compare favorably to rocking beam patterns done by Geiss (1976) using a similar sample.

A second example (Fig. 5.10) shows that STEM microdiffraction methods can often reduce the complexity of solving complicated orientation problems with its ability to spatially resolve areas only a few hundred Angstroms apart. Here, two 100 \AA microdiffraction patterns from adjacent twins in an ordered Ti-Al alloy can be analyzed much more easily than the typical SAD pattern taken from a much larger area. Several pairs of such patterns should allow the major twinning directions to be easily determined.

5.2 Identification of Crystal Defects by Microdiffraction

Complete characterization of dislocations or stacking faults by using microdiffraction patterns alone was not achieved. Nevertheless, it can be shown very clearly that it is possible in principle to carry out such an experiment. The primary limitations with the equipment, probe instabilities and high contamination rates, may be possibly overcome by new generation electron microscopes in a short time. For example, the successor to the Philips EM 301, the EM 400, has a vacuum of 10^{-7} torr as opposed to 10^{-5} torr for the 301 and a guaranteed maximum drift rate of less than $10 \text{ \AA}/5$ minutes.

Even with the 301, it is relatively easy to demonstrate the sort of microdiffraction conditions required for patterns that could be adapted to the computer simulation approach. Ideally, a defect identification procedure using microdiffraction should contain the following steps:

- 1) In the STEM mode, image a defect such as the stacking fault image seen in Fig. 5.11, preferably under n-beam conditions.



(a)



(b)



Figure 5.10 An ordered Ti-Al alloy shows a heavily twinned structure and a complex SAD diffraction pattern. STEM microdiffraction patterns from adjacent twins show single crystal patterns that are much more easily analyzed. Probe diameter = 100Å.

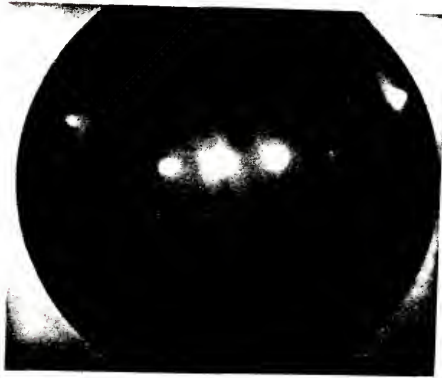
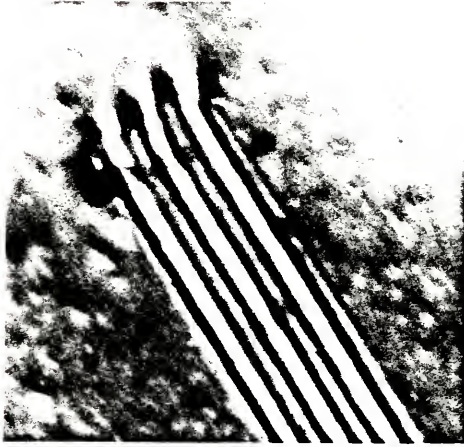


Figure 5.11 Silicon stacking fault imaged for N-beam conditions and its associated SAD diffraction pattern from a 20 μm aperture.

- 2) Stop the scanning motion, and position the probe along several positions close to the dislocation core. Record the microdiffraction pattern with the plate camera and the position of each probe position with respect to the ends of the dislocation.
- 3) Compute the $\frac{|S|^2}{|T|^2}$ value using the methods discussed in Chapter II and compare them to the experimental values obtained by a densitometer directly from the microdiffraction patterns.

As the core of the dislocation may be displaced a significant amount from the position implied by the center of the diffraction contrast image, it is probable that the computer simulated column would have to be "moved" several times to obtain a good fit with the experimental data. However, only one column need be computed for each test and, even with the increase in computation time required for n-beam conditions, it would seem that many possible Burgers vectors could be eliminated without resorting to computing the entire computed simulated defect image. It should be emphasized that microdiffraction could probably never completely supplant the image simulation approach--the information it provides is the same but the area of sample from which it comes must be determined with an extremely high degree of accuracy.

STEM microdiffraction patterns that could be used for defect identification are shown for a stacking fault in silicon with n-beam conditions. Once the fault image was displayed on the CRT the raster was stopped and an 80 Å diameter probe was slowly moved across the

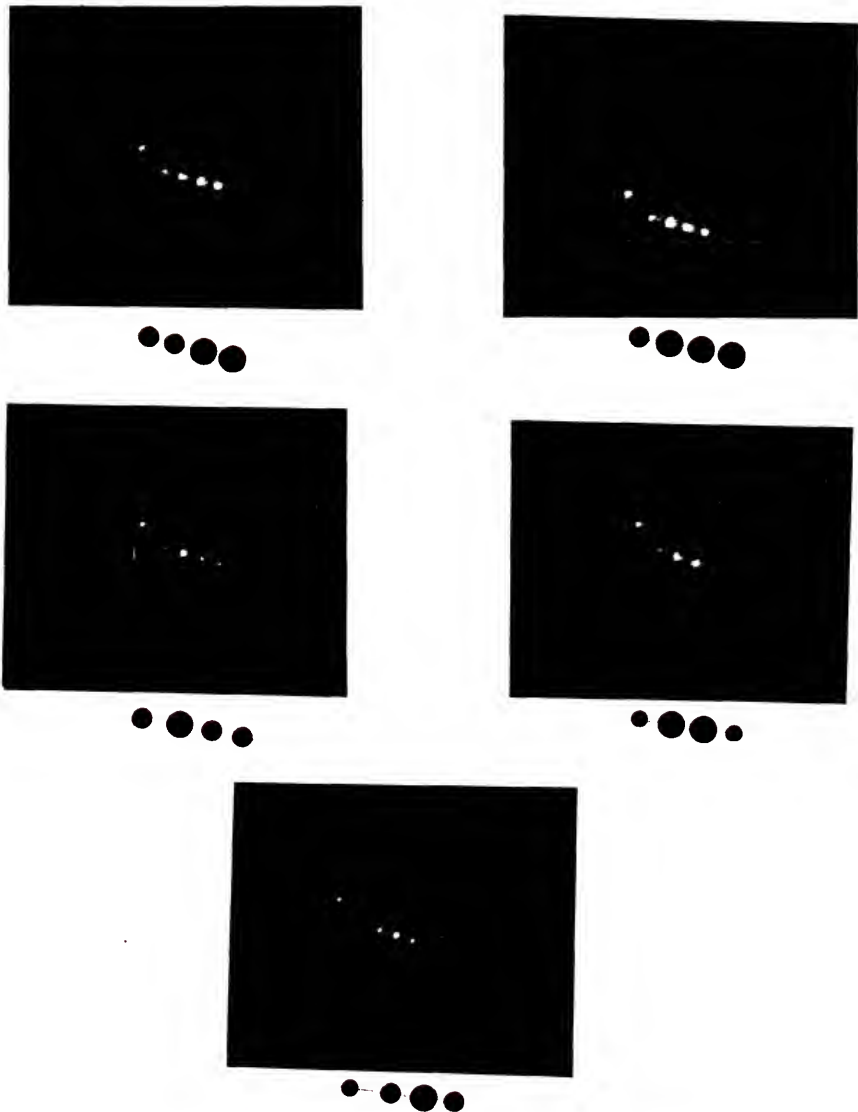


Figure 5.12 STEM microdiffraction patterns from areas spaced roughly 100 Å apart over the stacking fault fringes shown in the previous figure. The relative intensities of the spots are diagrammed next to each pattern.

stacking fault fringes in the direction shown in Fig. 5.11. Each time an intensity change was visually detected the pattern was recorded with the plate camera. The results shown in Fig. 5.12 show clearly that several intensity changes can be seen even with a relatively "simple" contrast image such as fringes produced by a stacking fault. It is also important to note that there is more information in an n-beam microdiffraction pattern than the equivalent point on the bright-field image. This is because the bright-field intensity, $|T|^2$, is

$$|T|^2 = 1 - |S_1|^2 - |S_2|^2 \dots |S_n|^2 \quad (5.1)$$

The intensities for the scattered beams could be obtained from their dark-field images only one at a time but they are all available directly in a single microdiffraction pattern.

An estimate of the number of microdiffraction experiments necessary to identify a defect is shown in Fig. 5.13. Here, computer simulations of six dislocations with different Burgers vectors are imaged for exactly the diffraction conditions. If microdiffraction patterns were taken from the positions marked by the four circles (roughly 70 \AA in diameter) on each of the six dislocations, the dark areas of the image would indicate a high $|S|^2$ value and the lighter areas a high $|T|^2$ value. For a rough comparison, then, let a $|S|^2/|T|^2$ ratio be symbolized by a "+" for a dark area and a "0" for a lighter one. For each of the 4 circled areas, the six dislocations have the values:

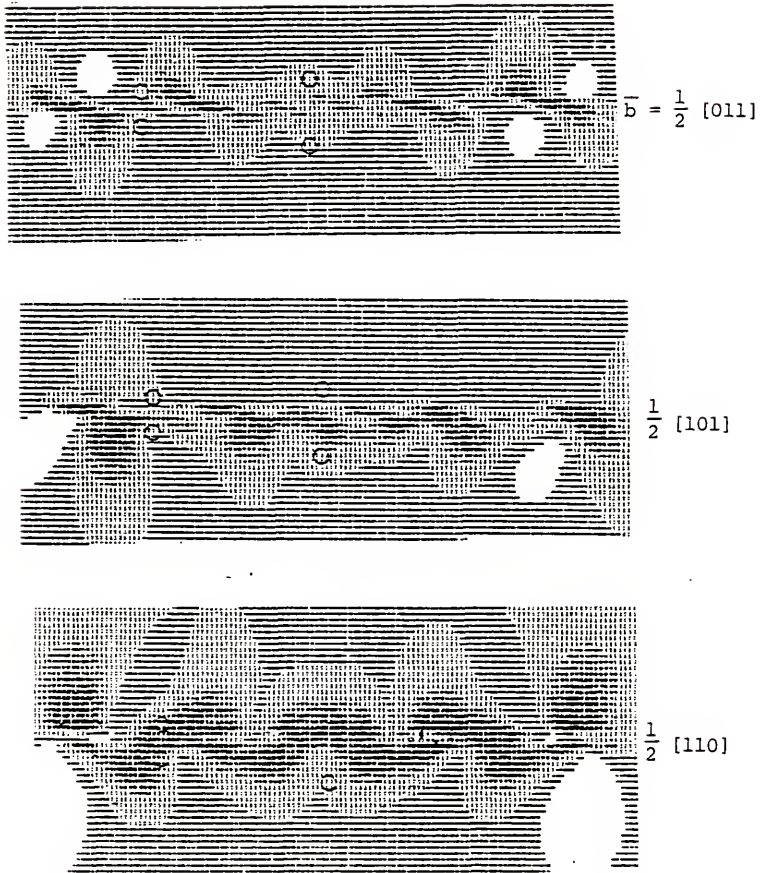


Figure 5.13 Computer simulated two-beam images of dislocations in silicon. The beam and foil normal are (112) , $g = (1\ 1\ 1)$, and $s = 0.0$. Images are shown for six different Burgers vectors.

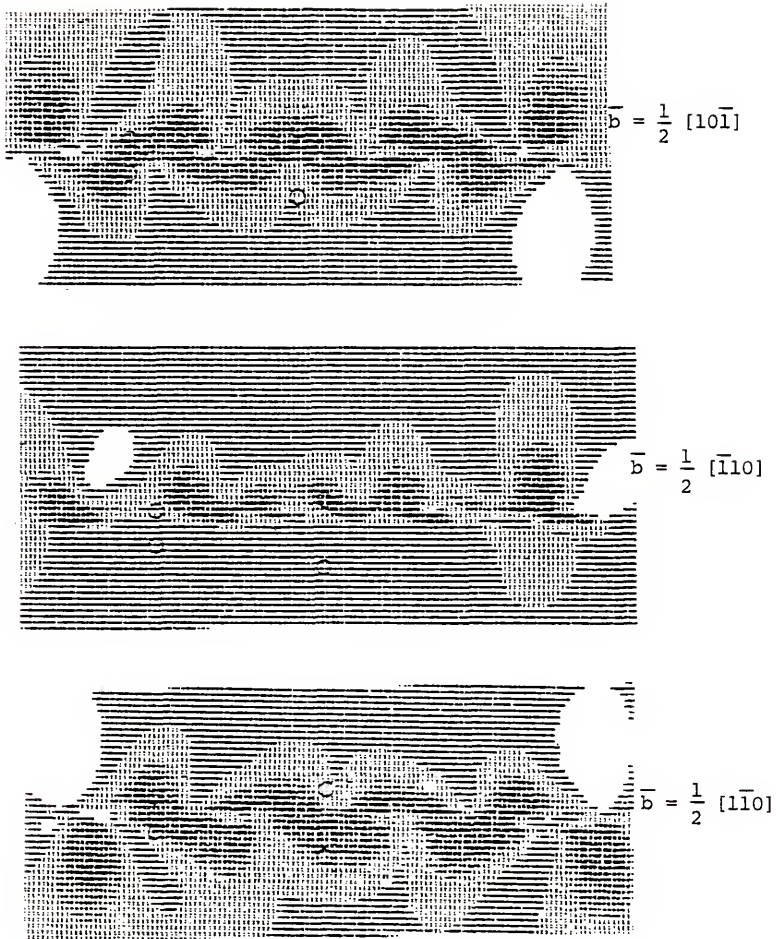


Figure 5.13 Computer simulated two-beam images of dislocations in silicon. The beam and foil normal are (112) , $g = (1\ 1\ 1)$, and $s = 0.0$. Images are shown for six different Burgers vectors.

Table 5.2

Dislocation Identification					
	b	1	2	3	4
A	$1/2(011)$	0	0	0	0
B	$1/2(101)$	0	0	0	0
C	$1/2(110)$	+	+	0	+
D	$1/2(10\bar{1})$	+	+	0	+
E	$1/2(\bar{1}10)$	+	0	0	+
F	$1/2(1\bar{1}0)$	0	+	0	0

It can be seen from the table that the dislocations A and B could probably not be distinguished and also dislocations C and D. Nevertheless, for any given image, the number of possibilities could be reduced from 6 to 2 and only after calculating 4 columns rather than the several thousand needed for form the image. Microdiffraction could thus be used as a "sorting procedure" to eliminate all but the most likely cases. The costs of the computer simulation method could then be greatly reduced as only a few images need be computed verification at the end of the sorting process.

5.3 Computer Simulation of STEM Crystal Defect Images

The programs developed in Chapter II were used to simulate two-beam images of stacking faults in silicon for both TEM and STEM conditions. Initially, the proper form of the STEM correction to the Bragg deviation had to be determined by using the programs to plot $|T|^2$ versus thickness for various values the Bragg deviation. The

results (Fig. 5.14 to 5.17), show contrast variations similar to the thickness fringes seen experimentally in a wedge-shaped foil.

As discussed in Chapter II, the STEM modification is of the form:

$$W_{\text{STEM}} = W \pm \Delta W \quad (5.2)$$

where

$$\Delta W = |g| \xi_g \alpha_i$$

The correction factor represents a range of values between 0 and ΔW where each value is weighted appropriately. Thus, a STEM calculation for a column consists of several matrix multiplication sequences, each with a different value of ΔW . The results for each set of multiplications is then added together to get the final result:

$$|T|_{\text{total}}^2 = |T_1|^2 + |T_2|^2 + \dots + |T_n|^2 \quad (5.3)$$

Where the initial amplitude of T_n is: $T_{\text{total}} \sqrt{1/N}$

If $W = 0.5$, for example, and the ΔW range was divided into 3 equal segments, then 4 curves would be plotted with ΔW values equal to -0.5 , $-0.5/6$, $+0.5/6$ and $+0.5$. Intensity curves ($|T|^2$) versus thickness curves were plotted for as many as 6 ΔW values (Fig. 5.14). In general, modifications to the curve were quite minor if more than 4 ΔW values were used and, for reasons of economy, all STEM image simulations were plotted with a 4 ΔW value average.

The effect of the STEM modification is shown in Figures 5.15, 5.16 and 5.17, where a value of $\alpha_i = 5 \times 10^{-3}$ rad, is added to $|T|^2$ versus thickness curves for $W = -0.5$, 0.0 and $+0.5$. In each case,

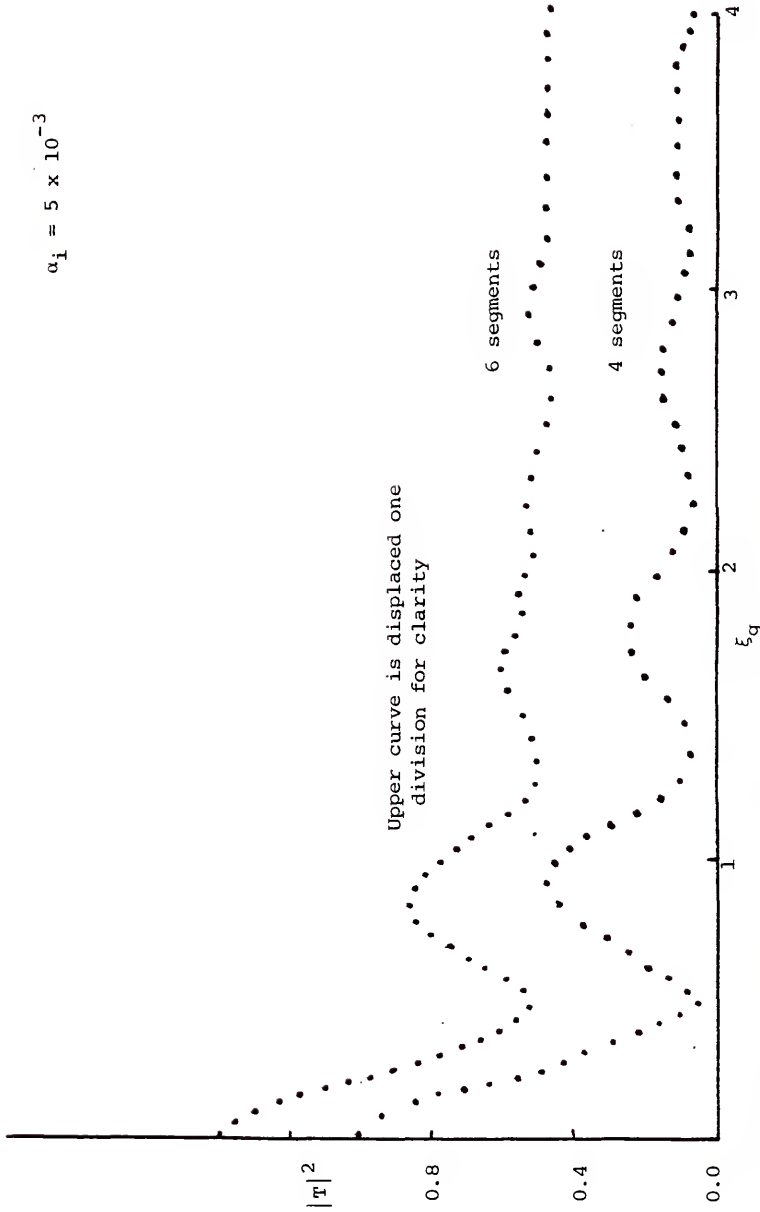


Figure 5.14 The effect of STEM on the intensity curve is shown above for $\Delta w = 4$ and 6 segments. The upper curve has been shifted 1 division upward, on the graph for clarity. These two curves should be compared with the curve for $w = 0$ and no STEM correction shown in Fig. 5.16.

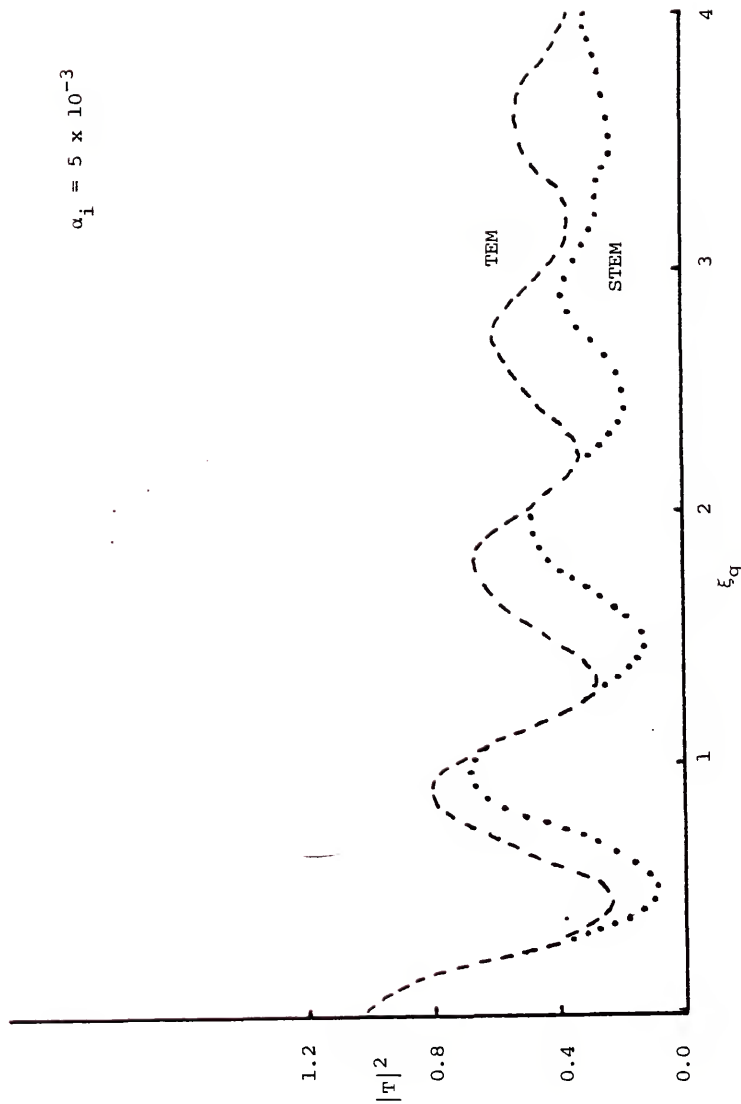


Figure 5.15 Comparison of TEM and STEM Intensity curves for a Bragg deviation of 0.5.

$$\alpha_1 = 5 \times 10^{-3}$$

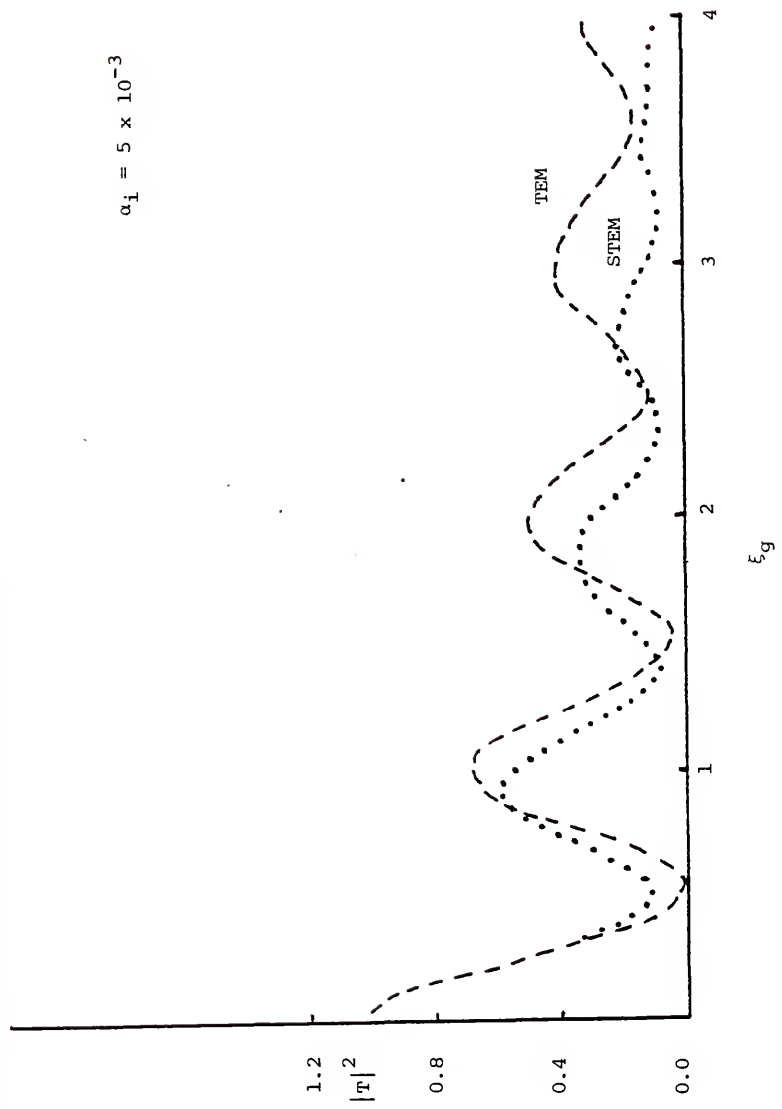


Figure 5.16 Comparison of TEM and STEM Intensity Curves for 0.0 Bragg deviation.

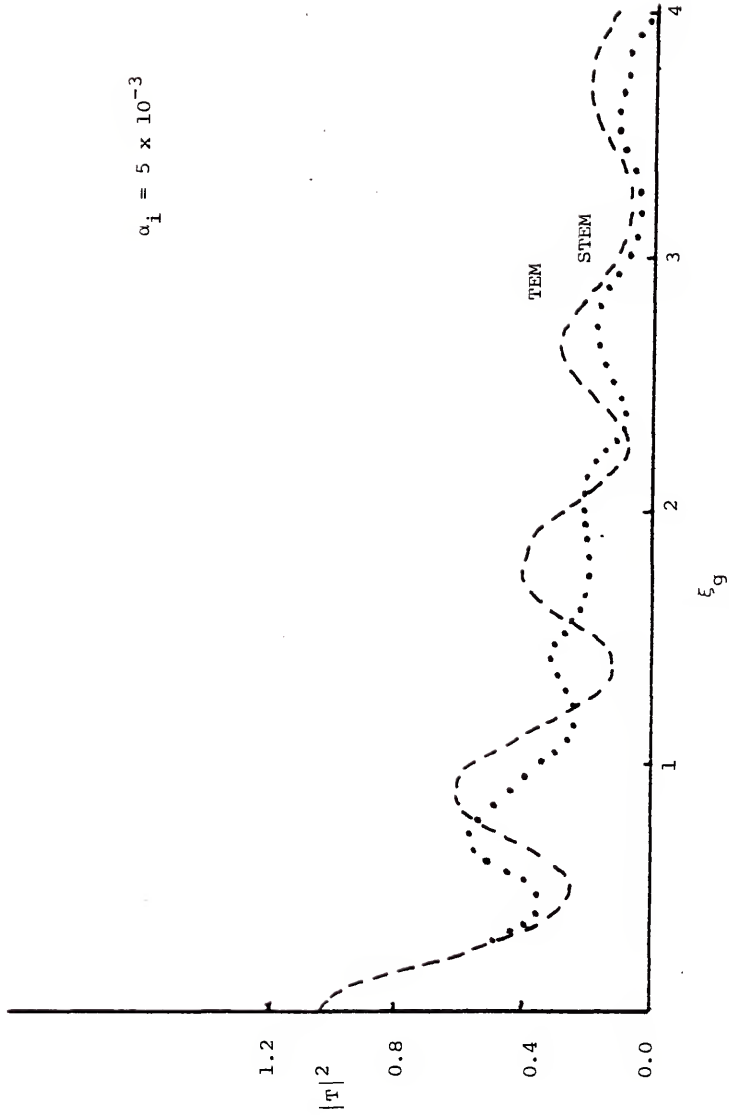


Figure 5.17 Comparison of TEM and STEM intensity curves for Bragg deviation of -0.5 .

the STEM modification damps-out the oscillations in $|T|^2$ and lowers the average height of the curve. This implies that an image of thickness fringes in a wedge-shaped foil would exhibit reduced contrast, as well as a lower absolute intensity than would be the case for TEM conditions.

This result must be interpreted with care. At certain thicknesses and Bragg deviations the $|T|^2$ value for STEM may be increased over the TEM value. This is true in Fig. 5.17 for $t = 3/2 \xi_g$ where $|T|_{STEM}^2 = 0.3$ and $|T|_{TEM}^2 = 0.15$. In Figs. 5.15 and 5.16, where $W > 0.0$, this occurs less frequently. It is clear that the STEM correction changes the wavelength of the $|T|^2$ curve, particularly when $W < 0$. This implies that the width of extinction fringes in a wedge-shaped foil will vary with the magnitude of α_1 . The extent of the variation should be greatest for negative Bragg deviations.

In Figs. 5.18, 5.19 and 5.20, extrinsic stacking faults silicon, where $\bar{R} = 1/3 \langle 111 \rangle$, are imaged for 3 different \bar{g} vectors. Here the decrease in intensity from STEM is of minor importance, since the gain control can be used to increase the strength of the overall signal on the CRT. Contrast does decrease as before, but it is noteworthy that modification of the image is most severe in the central regions of the stacking fault. As predicted by Joy and Maher (1975), defect images with the shorter extinction distances such as the $g = \langle 111 \rangle$ image (Fig. 5.18) show the least amount of modification from the STEM correction, while those with higher g values such as $\bar{g} = [311]$ show strong changes even for low α_1 values. For example, in image (b)

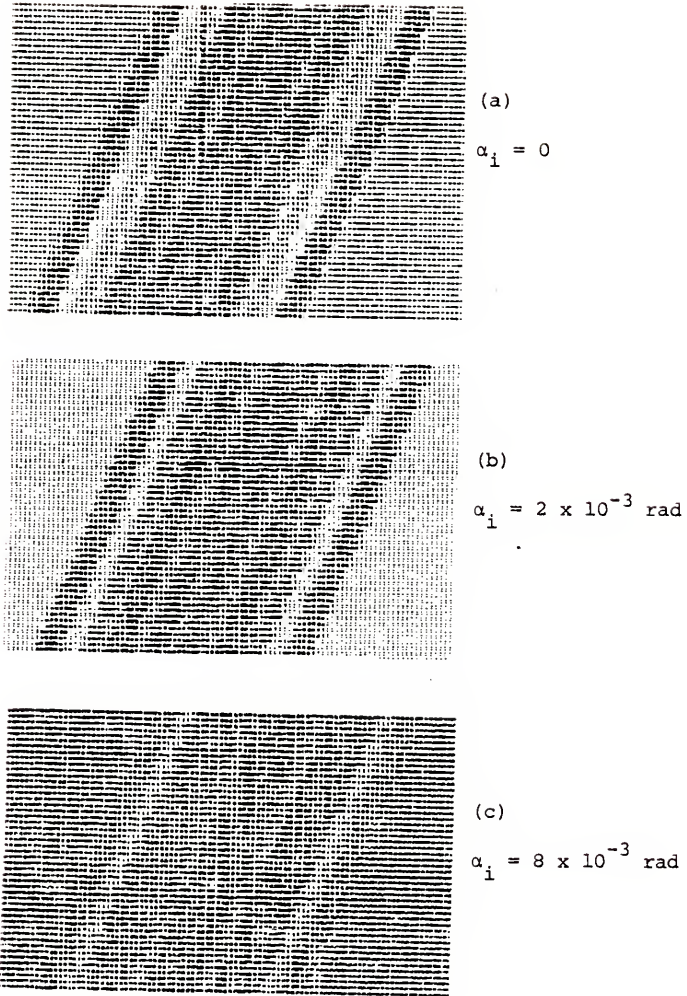
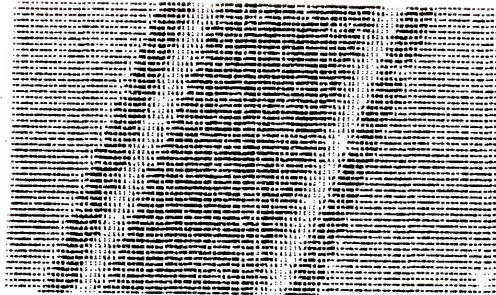
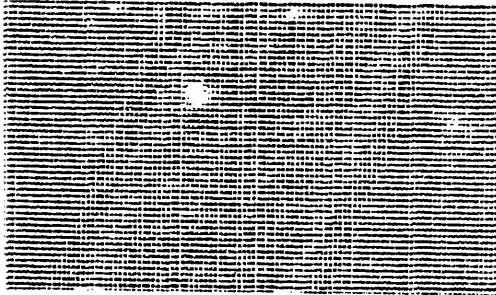


Figure 5.18 TEM and STEM simulations of stacking fault in silicon.
 BM = (112), FN = (112), $g = (111)$, zero Bragg deviation.



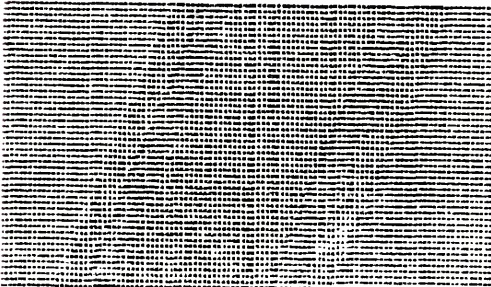
(a)

$$\alpha_i = 0$$



(b)

$$\alpha_i = 2 \times 10^{-3} \text{ rad}$$



(c)

$$\alpha_i = 8 \times 10^{-3} \text{ rad}$$

Figure 5.19 TEM and STEM simulations of fault shown in Fig. 5.18. g vector changed to (311).

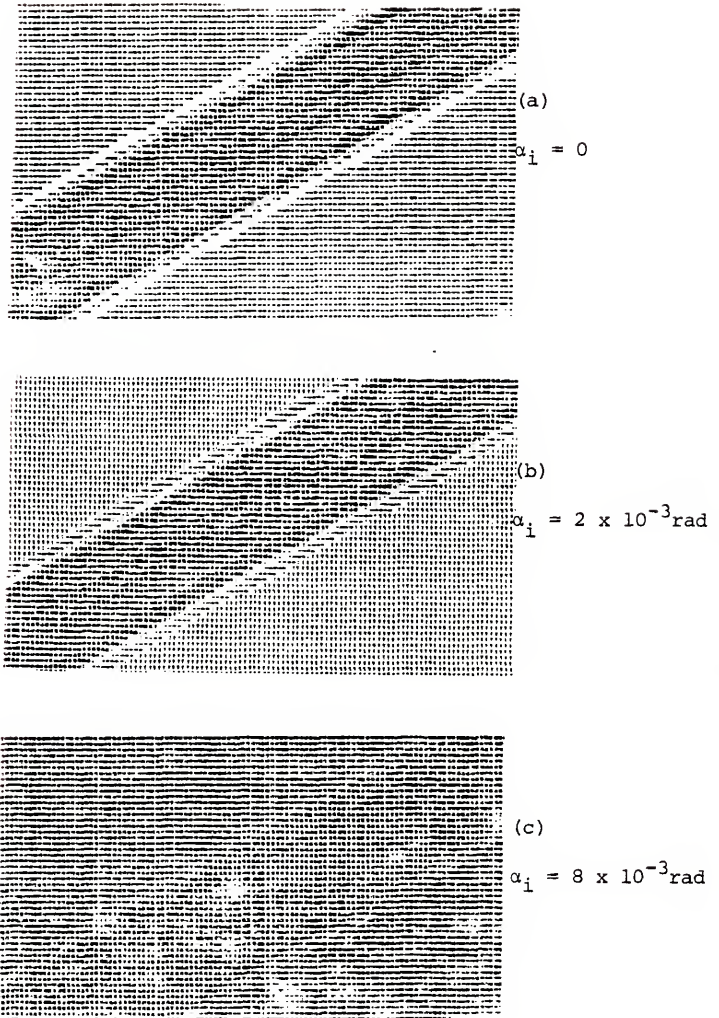


Figure 5.20 TEM and STEM simulations of fault shown in Fig. 5.18. g vector changed to (220) and BM and FN changed to (111).

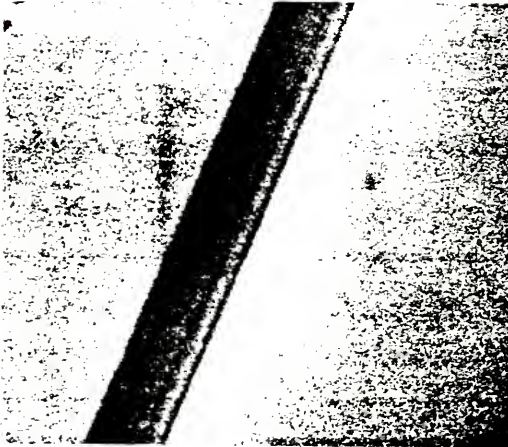
of Figs. 5.18, 5.19 and 5.20, ($\alpha_i = 2 \times 10^{-3}$ rad) only the $g = \langle 311 \rangle$ image undergoes significant modification.

The STEM simulations are compared to experimental TEM and STEM images in Fig. 5.21. Here, $\bar{g} = \langle 311 \rangle$ and $\alpha_i = 5 \times 10^{-4}$ rad for TEM (a), and 8×10^{-3} rad for STEM (b). In the STEM image, the central fault fringes exhibit reduced contrast as was predicted by the computer simulation in Fig. 5.20.

A final point concerning the effect of convergence or diffraction contrast imaging is shown in Fig. 5.22. Here, the TEM plate camera was used to record two-beam fault images for two widely different values of α_i . Although α_i is changed by a factor of 50 the images appear identical. The reason is that the fault itself for the highly convergent beam does not lie in the specimen plane. The convergence angle of any portion of the beam that forms a particular point on the image is much smaller than the convergence angle of the entire beam. This is not the case for STEM imaging, where the probe cross-over lies at the specimen plane. Thus, the actual distance of the focal point of the electron beam from the specimen as well as the convergence angle must be considered to correctly determine the extent of image modification by convergent beam radiation.

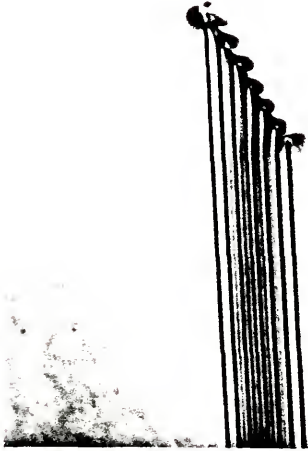


TEM



STEM

Figure 5.21 Comparison of STEM and TEM two-beam fault images for $g = (311)$



(a)



(b)

Figure 5.22 Two-beam image of fault with $g = (220)$ and $\alpha_i = 10^{-2}$ (a) and $\alpha_i = 5 \times 10^{-4}$ (b). The images are nearly identical.

5.4 Determination of Grain Orientation of a Fine-Grained Superalloy Using Focused Condenser Aperture Microdiffraction

A good example of the use of focused C2 aperture microdiffraction is the analysis of intergranular orientation of the nickel superalloy shown in Fig. 5.23. The image shows many grains less than $1\mu\text{m}$ in diameter, less than the minimum size that allows normal selected area diffraction methods to produce single crystal diffraction patterns. However, focusing the demagnified image of a $10\mu\text{m}$ C2 aperture at the specimen plane allows microdiffraction patterns to be formed from areas only 2600 \AA in diameter. Now, single crystal patterns can be obtained as shown in Fig. 5.24 and 5.25.

These patterns can be used to determine the orientation of adjacent grains using the method described in Section 3.2. To proceed, microdiffraction patterns from each of the two grains in the center of the image were recorded for two different tilts of the goniometer stage. For this alloy, the Kikuchi lines were sufficiently sharp to allow the electron beam direction, with respect to each grain, to be determined to an accuracy of about $1/2^\circ$. If this had not been the case, channeling lines, produced either by the focused spot or the rocking beam methods, could have been used for the same purpose.

In Fig. 5.24 and 5.25, two prominent pairs of Kikuchi lines are diagrammed along with the first-order spots for each of the four diffraction patterns. The linear distance between the Kikuchi pattern center and the zero-order beam can now be used to compute α , the angle through which the major pole direction must be tilted to form

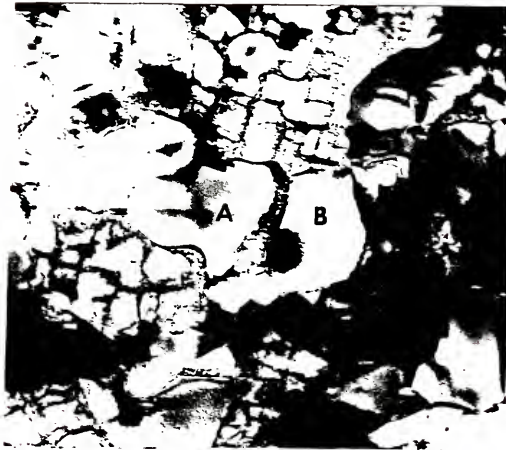


Figure 5.23 TEM image of Ni₃Al(Mo) alloy showing fine grain structure and intergranular precipitates. Many of the grains are less than 1 μ m in diameter. The two grains used for the analysis are marked A and B.

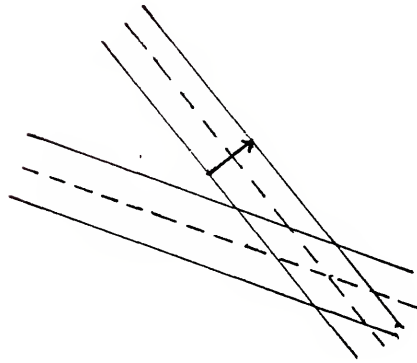
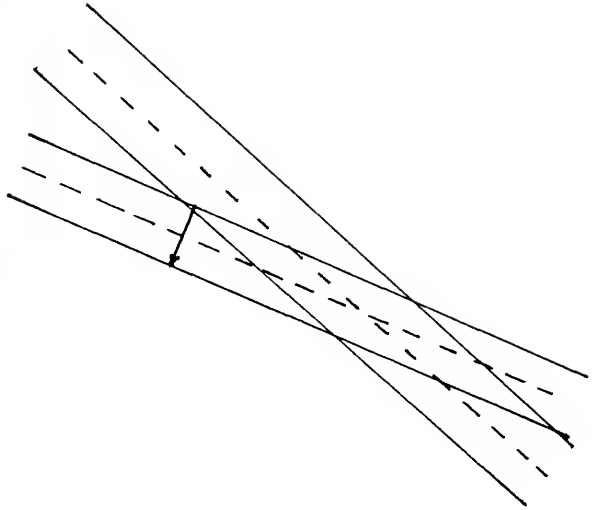
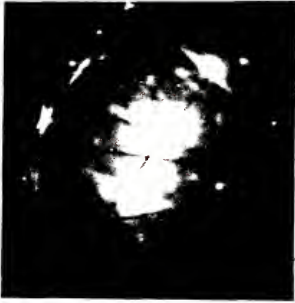


Figure 5.24 Focused C2 aperture microdiffraction patterns for grain "A." Kikuchi lines pairs used to determine exact beam direction are diagrammed beside the diffraction patterns. Tilt angle between patterns is 26° .

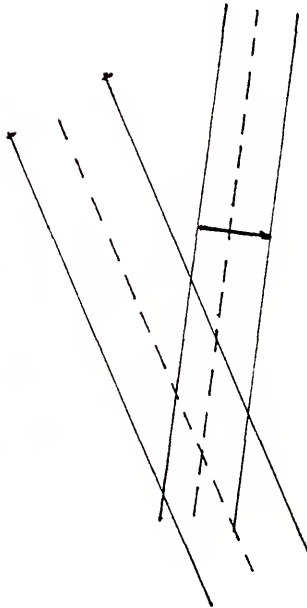
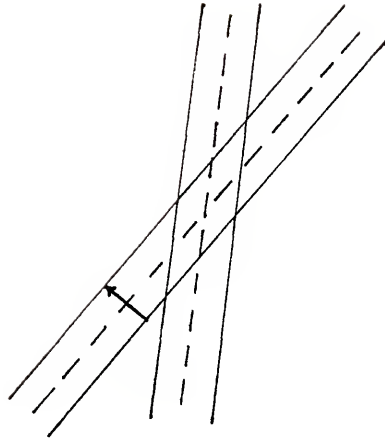


Figure 5.25 Microdiffraction patterns for grain "B" taken at same goniometer tilts as Figure 5.24.

the diffraction pattern. Using Eqn. 4.12, the exact beam direction is calculated for each microdiffraction pattern and listed below.

Table 5.3
Exact Beam Directions

	Grain #1		Grain #2	
	Fig. 5.24a	Fig. 5.24b	Fig. 5.25a	Fig. 5.25b
h	0.78	0.43	0.43	0.57
k	0.42	0.43	0.43	0.00
l	0.47	0.79	0.79	0.82

The exact beam directions listed in Table 5.3 is the only information necessary to calculate the orientation difference between the two grains. The misorientation is defined by a 3 x 3 direction cosine array. The relation between the beam directions for the two grains for any particular goniometer position was defined in Section 3.2 as

$$BM_i = l_{ij} BM_j^* \quad (5.4)$$

As was shown, l_{ij} is determined by expanding and solving for three of the l_{ij} components at one time. From Table 5.3 and Eqn. 5.4, one obtains:

$$\begin{aligned} .78l_{11} + .42l_{12} + .47l_{13} &= .43 \\ .43l_{11} + .43l_{12} + .79l_{13} &= .57 \\ l_{11}^2 + l_{12}^2 + l_{13}^2 &= 1 \end{aligned} \quad (5.5)$$

The form of the equations is

$$\begin{aligned}
 ax + by + cz &= d \\
 ex + fy + gz &= h \\
 x^2 + y^2 + z^2 &= 1
 \end{aligned}
 \tag{5.6}$$

With a solution of the form

$$x = C3 - C4*z \tag{5.7}$$

$$y = C1 - C2*z$$

$$z = \frac{-BB + \sqrt{BB^2 - 4*AA*CC}}{2*AA}$$

where

$$C1 = \frac{ah - ed}{af - eb} \tag{5.8}$$

$$C2 = \frac{ag - ec}{af - eb} \tag{5.9}$$

$$C3 = \frac{d - b*C1}{a} \tag{5.10}$$

$$C4 = \frac{-b*C2 + C}{a} \tag{5.11}$$

$$AA = C2^2 + C4^2 + 1 \tag{5.12}$$

$$BB = -2(C1*C2 + C3*C4) \tag{5.13}$$

$$CC = C1^2 + C3^2 - 1 \tag{5.14}$$

While the algebra is cumbersome, it is easy to program for a computer. The same algorithm is used to solve for the other six direction cosine components and the complete solution is

$$l_{ij} = \begin{pmatrix} .34 & -.51 & .85 \\ .90 & -.29 & -.32 \\ .41 & .85 & .36 \end{pmatrix} \tag{5.15}$$

To check for accuracy, l_{ij} can now be used to transform any beam direction in one grain for a given tilt into the beam direction of the adjacent grain. Thus, from Table 5.3

$$\begin{pmatrix} .34 & -.51 & .82 \\ .90 & -.29 & -.32 \\ .41 & .85 & .36 \end{pmatrix} \begin{pmatrix} .78 \\ .42 \\ .47 \end{pmatrix} = \begin{pmatrix} .45 \\ .43 \\ .84 \end{pmatrix} \quad (5.16)$$

The direction [.45 .43 .84] compares closely with the experimental result, [.43 .43 .79] and so the l_{ij} matrix must be correct. Since each microdiffraction pattern is correct to only about $1/2^\circ$, the above procedure should be solved for several pairs of beam directions and the components of l_{ij} averaged to provide a more accurate result. Even the abbreviated procedure discussed above, however, shows precisely the nature of the misorientation across the given boundary and should be of use in many related problems.

CHAPTER 6
CONCLUSIONS AND SUGGESTIONS FOR FUTURE RESEARCH

Results of this study show that the interpretation of any microdiffraction method depends upon the use of a convergent, rather than a parallel, or well-collimated, electron beam. The convergence angle, as defined by α_i , directly affects:

- a) signal to noise ratio in the diffraction pattern (larger α_i values increase signal strength),
- b) contamination (larger α_i values increase contamination rates),
- c) form of information in the diffraction pattern (larger α_i values form channel-type patterns while smaller ones produce discrete diffraction spots composed of small diameter discs).

Convergence angles can be calculated directly from microdiffraction patterns as described in Section 4.1, so exact quantitative comparisons of the effect of α_i on the parameters listed above can be found and optimum α_i values can be repeated in subsequent experiments. It is suggested that convergence angles be listed in microdiffraction studies just as "two-beam conditions" are always recorded in selected area diffraction experiments.

The most efficient way to categorize microdiffraction methods is according to the electron-optic lens configuration used to form

the diffraction pattern. The methods described in this work can be summarized as:

- a) Focused Spot--The image can be viewed directly or displayed on a CRT in STEM, but the microdiffraction patterns are always recorded with the plate camera at the base of the microscope column.
- b) Focused Condenser Aperture--Image and diffraction pattern formed in a conventional manner, but a small ($<10\ \mu\text{m}$) condenser is focused on the sample and illuminates only a small area in the diffraction mode.
- c) Rocking Beam--Image formed in a conventional manner but the beam is rocked over the sample, the detector size selects a portion of the image to form diffraction pattern on CRT.

In addition, both the focused spot and rocking beam techniques can form transmission channeling patterns for large convergence angles.

All of the three methods have advantages and disadvantages.

Focused spot methods can examine areas as small as $50\ \text{\AA}$ in diameter but have high contamination rates and cannot be used on sensitive materials. Focused condenser aperture methods have excellent angular resolution in the diffraction pattern and low contamination rates, but the minimum area that can be examined is $500\ \text{\AA}$ (for a $2\ \mu\text{m}$ C2 aperture). The rocking beam technique offers complete control of angular resolution and contamination no higher than conventional TEM, but its signal-to-noise ratio is the poorest of the three methods.

Results from the computer simulation studies in Chapter 5 show that STEM crystal defect images can be simulated in the same manner as those formed by conventional TEM as long as convergence effects are taken into account. The stacking fault simulations verify that the extent that a STEM image will differ from its TEM counterpart is predicted by the equation $\Delta W = \alpha_i \xi_g |g|$. Thus, STEM images undergo the greatest modification for highly convergent probes and higher order reflections. The primary effect of STEM appears to be a loss of contrast, particularly in regions where the defect passes close to the central and lower parts of the specimen. Since the STEM simulations (just as TEM) consists of thousands of column calculations, there appears no immediate advantage to studying diffraction contrast images with a STEM-equipped electron microscope. However, this work does show in a semi-quantitative fashion that STEM differs from TEM only by the convergence angle effect. As a result, the same mathematical formalism developed Howie and Whelan can now be used with confidence to simulate the intensity of n-beam microdiffraction patterns.

The same basic type of information is contained in microdiffraction patterns and selected area diffraction patterns. Microdiffraction has only two advantages over selected area techniques. First, it improves the signal-to-noise ratio of the diffraction pattern from small precipitates. In other words, the precipitate/matrix volume ratio increases because a smaller portion of the sample is used to form the diffraction pattern. Second, the reduction in effective excited specimen volume enables the analysis of

structures that vary periodically over distances of a few hundred Angstroms.

In this work, most of the emphasis was placed on the second class of problem. More data, consisting of at least several microdiffraction patterns, are required to solve a problem, and an efficient means of mathematical analysis has been shown to be essential. It has been shown that slight modifications to the dynamical theory to account for convergence and a few simple relations from analytical geometry can be used to solve a wide variety of problems in metallurgical microscopy.

Probably the single most promising avenue for future research is the solution of the n-beam problems to simulate microdiffraction patterns that have been modified by three-dimensional (non-symmetric) strain fields. Computer simulation of the images of these defects is still far too wasteful of computer time. The possibility of characterizing a defect strain field with only a few microdiffraction patterns, each corresponding to one column of distorted crystal, should be of interest to many investigators.

APPENDIX

The program listed below can be used to compute $|T|^2$ or $|S|^2$ values for rocking curves, intensity versus thickness curves, and dislocation and stacking fault images. The Thölén method of matrix multiplication described in Chapter 2 is used in each case.

```

DIMENSION BM(3),F(3),U(3),G(3),BR(3),BXU(3),V(3),P(3),BRE(3)
DIMENSION DUM(3),GTHETA(5000),GDOTR(5000),X(3),Y(3),Z(3)
DIMENSION A(3,3),IIRROW(121),IIRROW1(121),ROW(121)
DIMENSION ISYM(11),JSYM(11),SYM(11)
DIMENSION F1(3),G1(3),BM1(3),U1(3),BR1(3)
DATA PI,POIS,TWOPI/3.14159,0.33,6.28318/
DATA ISYM/' ','-',':','1','=' ,'"','"','H','"','H','B' /
DATA JSYM/3*' ','-',':','-','-','-' /,'U','Z','%' /
COMPLEX A11(1401),A12(1401),A22(1401),SQ,C1,C2,II,T,S
COMPLEX TEM,C3,C4,DENOM
DATA SYM/1.15,.93,.78,.69,.63,.55,.48,.42,.36,.31,.05/
T=(1.0,0.0)
S=(0.0,0.0)
READ(5,1) BM(1),BM(2),BM(3),F(1),F(2),F(3)
READ(5,1) U(1),U(2),U(3),G(1),G(2),G(3)
READ(5,1) BR(1),BR(2),BR(3),DUM(1),DUM(2),DUM(3)
1  FORMAT(6(F4.1))
   READ(5,2) ANO,WF,TH
2  FORMAT(3(F4.2))
   READ(5,3) NUM,GEXT,ALI
3  FORMAT(12,F4.1,F6.4)
   T=(1.0,0.0)/NUM
   S=(0.0,0.0)
   VAL=0
   DELWF=GEXT*ALI

INSURE U & BM ARE ACUTE
CALL NORM(U,BM,DUM)
CUB=U(1)*BM(1)+U(2)*BM(2)+U(3)*BM(3)
IF(CUB.GE.0.0)GO TO 8
U(1)=-U(1)
U(2)=-U(2)
U(3)=-U(3)
8  CONTINUE

COMPUTE PICTURE COOD. & NORMALIZE
DO 10 I=1,3
10  Z(I)=BM(I)
    CALL XPROD(X,U,BM)
    CALL XPROD(Y,Z,X)
    CALL NORM(X,Y,Z)

DEFINE TRANSFORMATION MATRIX
DO 20 I=1,3
20  A(1,I)=X(I)
    A(2,I)=Y(I)
    A(3,I)=Z(I)

```

```

TRANSFORM INPUT VECTORS TO TO PICTURE COOD.
DO 22 I=1,3
  BM1(I)=BM(I)
  F1(I)=F(I)
  U1(I)=U(I)
  G1(I)=G(1)
22  BR1(I)=BR(I)
    DO 25 I=1,3
      BM(I)=A(I,1)*BM1(1)+A(I,2)*BM1(2)+A(I,3)*BM1(3)
      F(I)=A(I,1)*F1(1)+A(I,2)*F1(2)+A(I,3)*F1(3)
      U(I)=A(I,1)*U1(1)+A(I,2)*U1(2)+A(I,3)*U1(3)
25  G(I)=A(I,1)*G1(1)+A(I,2)*G1(2)+A(I,3)*G1(3)
C   NORMALIZE, BM, F, & U ONLY
    CALL NORM(BM,F,U)
    DOT=BM(1)*F(1)+BM(2)*F(2)+BM(3)*F(3)
    DIG=ABS(DOT-1.)
    PRINT,U(1),U(2),U(3)

C
C   COMPUTE VECTORS PREPENDICULAR TO DISL. & NORMALIZE
    CALL XPROD(BXU,BR,U)
    CALL XPROD(V,U,BXU)
    CALL XPROD(P,V,U)
    CALL NORM(P,V,BXU)

C
C   COMPUTE BURGER'S EDGE COMPONENT
    DO 30 I=1,3
30  BRE(I)=(BR(1)*V(1)+BR(2)*V(2)+BR(3)*V(3))*V(I)

C
C   COMPUTE FOIL THICKNESS SEEN BY BEAM,DZ, & YO
    ANORM=ANO/2.
    TZ=TH/ABS(BM(1)*F(1)+BM(2)*F(2)+BM(3)*F(3))
    DZ=TZ/40
    YO=(U(2)*F(3)*TZ)/(2*(U(2)*F(2)+U(3)*F(3)))
    YO=ABS(YO)
    CR=5000/(10.0*TZ)
    IB=700
    IQQ=100

C
C   COMPUTE CONSTANTS FOR COLUMN CALCULATION
    UA=U(2)**2
    UB=U(2)*U(3)
    UC=U(3)**2

C
C   COMPUTE CONSTANTS FOR DISPLACEMENT C AL'N
    CA=(G(1)*BR(1)+G(2)*BR(2)+G(3)*BR(3))/(2*PI)
    CB=(G(1)*BRE(1)+G(2)*BRE(2)+G(3)*BRE(3))/(8*PI*(1-POIS))
    DUMMY=G(1)*BXU(1)+G(2)*BXU(2)+G(3)*BXU(3)
    CC=DUMMY*((1-2*POIS)/(4*PI*(1-POIS)))
    CD=DUMMY/(8*PI*(1-POIS))

```

```

C
C   COMPUTE & STORE THE DISPLACEMENT MATRIX
DO 35 I=1,5000
GAM=(2*PI/5000)*I
R=(10.0*TZ/5000)*I
GTHETA(I)=CA*GAM+CB*SIN(2*GAM)+CD*COS(2*GAM)
GDOTR(I)=CC*(ALOG(R))
35 CONTINUE
C   COMPUTE & STORE THE 1400 SCATTERING MATRICES
   II=(0.0,1.0)
   DO 5 I=1,1401
   IJ=I-1
   W=-.3.5+.005*IJ
   SQ=CSQRT(1.+W**2-ANO**2+2.*II*ANO)
   DENOM=(TWOPI*II*SQ)
   C1=PI*II*(W+SQ)
   C2=PI*II*(W-SQ)
   C3=PI*(II*W-ANORM)+PI*II*SQ
   C4=PI*(II*W-ANORM)-PI*II*SQ
   A11(I)=(-C2*CEXP(C3*DZ)+C1*CEXP(C4*DZ))/DENOM
   A12(I)=(CEXP(C3*DZ)-CEXP(C4*DZ))/(DENOM/(PI*(II-ANO)))
   A22(I)=(C1*CEXP(C3*DZ)-C2*CEXP(C4*DZ))/DENOM
   TEST=W-WF
   IF(TEST.GE..001)GO TO 5
   TINTB=(CABS((-C2*CEXP(C3*TZ)+C1*CEXP(C4*TZ))/DENOM))**2
5 CONTINUE
C
C   WRITE(6,63)
63 FORMAT(1H1)
C   BEGIN PICTURE CAL'N & COMPUTE CONSTANTS FOR INNER LOOP
DO 40 I=1,60
QM=I-0.5
XX=.618*YO*QM/30-.618*YO
DO 45 J=1,121,2
QJ=J-0.5
YY=(YO*QJ)/60-YO
C
C   COMPUTE POSITION OF COLUMN TOP
IF(DIG.LT..02)Z0=TZ/2
Z0=TZ/2-(F(1)*XX+F(2)*YY)/F(3)
C
C   START COLUMN CAL'N
DO 51 N=1,NUM
WF=WF+DELWF*(N/NUM-0.5)
DO 50 K=1,41
KK=K-1
ZZ=Z0-DZ*KK

```

```

C
C   FIND DISTANCE BETWEEN DISLOCTION & DZ
R2=UC*YY-UB*ZZ
R3=UA*ZZ-UB*YY
R=SQRT((XX**2+R2**2+R3**2))
THETA=ARCOS((XX*V(1)+R2*V(2)+R3*V(3))/R)
COSAP=(XX*P(1)+R2*P(2)+R3*P(3))/R
IF(COSAP.LT.0.0)THETA=TWOPI-THETA
C
C   FIND DISP. MATRIX CORRESPONDING TO R & THETA
IR=CR*R
IF(IR.EQ.0)IR=1
IT=(5000*THETA)/(TWOPI)
IF(IT.EQ.0)IT=5000
IF(K.EQ.1)GO TO 49
C   COMPUTE BETA & CONVERT TO SUBSCRIPT FORM
BETA=(GDOTR(IR)+GTHETA(IT)-HOLD)/DZ + WF
IF(BETA.GT.3.5)BETA=3.5
IF(BETA.LT.-3.5)BETA=-3.494
IB=(BETA+3.5)/.005
IF(K.EQ.2)ITEST=IB
ITEST=IABS(IB-IHOLD)
IF(ITEST.GE.IQQ)IB=IHOLD
C
C   COMPUTE T & S & STORE INTENSITY IN ROW(J)
TEM=T
T=A11(IB)*T+A12(IB)*S
S=A12(IB)*TEM+A22(IB)*S
49  IHOLD=IB
50  HOLD=GDOTR(IR)+GTHETA(IT)
51  VAL=(CABS(T))**2 + VAL
    ROW(J)=VAL/TINTB
    VAL=0
    ROW(J)=((CABS(T))**2)/TINTB
    IF(J.EQ.1)GO TO 44
    ROW(J-1)=(ROW(J)+ROW(J-2))/2
44  T=(1.0,0.0)/NUM
    S=(0.0,0.0)/NUM
45  CONTINUE

```

```

C      PRINT ONE ROW OF THE PICTURE
      DO 54 J=1,121
      DO 55 M=1,11
      IF(ROW(J)-SYM(M))55,60,60
55     CONTINUE
      M=11
60     IIRROW(J)=ISYM(M)
54     IIRROW1(J)=JSYM(M)
      WRITE(6,65)IIRROW
      WRITE(6,66)IIRROW1
65     FORMAT(LX,121A1)
66     FORMAT(LH+,121A1)
40     CONTINUE
      STOP
      END

```

```

C
      SUBROUTINE XPROD(A,B,C)
      DIMENSION A(3),B(3),C(3)
      A(1)=B(2)*C(3)-B(3)*C(2)
      A(2)=B(3)*C(1)-B(1)*C(3)
      A(3)=B(1)*C(2)-B(2)*C(1)
      RETURN
      END

      SUBROUTINE NORM(A,B,C)
      DIMENSION A(3),B(3),C(3)
      SQA=SQRT(A(1)**2+A(2)**2+A(3)**2)
      SQB=SQRT(B(1)**2+B(2)**2+B(3)**2)
      SQC=SQRT(C(1)**2+C(2)**2+C(3)**2)
      DO 7 I=1,3
      A(I)=A(I)/SQA
      B(I)=B(I)/SQB
7     C(I)=C(I)/SQC
      RETURN
      END

```

REFERENCES

- Booker, G. R., D. C. Joy, J. P. Spencer and H. Graf von Harrach (1974); IITRI, Chicago, 1974, 225.
- Booker, G. R. and R. Stickler (1962); Brit. J. Appl. Phys. 13, 446.
- Booker, G. R. and W. J. Tunstall (1966); Phil. Mag. 55, 71.
- Broers, A. N. (1969); J. Sci. Instr. 2, 273.
- Cowley, J. M. and D. J. Smith (1973); J. Appl. Cryst. 4, 482.
- Edington, J. W. (1975); Electron Diffraction in the Electron Microscope (Macmillan, New York) p. 9.
- Fraser, H. L., M. H. Loretto, and I. P. Jones (1976); IITRI, Chicago, 1976, 329.
- Fujimoto, F. K. Komaki and S. Takagi (1972); Z. Naturforsch. 27, 441.
- Geiss, R. H. (1975); Appl. Phys. L. 27, 174.
- Geiss, R. H. (1976); IITRI, Chicago, 1976, 337.
- Goldstein, J. I. and D. B. Williams (1977); IITRI, Chicago, 1977, 172.
- Hall, C. E. (1966); Introduction to Electron Microscopy (McGraw-Hill, New York) p. 52.
- Hall, C. R. (1970); Phil. Mag. 60, 63.
- Head, A. K., and P. Humble, L. M. Clarbrough, A. J. Morton, C. T. Forwood (1973); Computed Electron Micrographs and Defect Identification (North-Holland, New York).
- Helfmeier, H. and M. Feller-Kniepmeier (1977); Appl. Phys. L. 48, 3997.
- Hirsch, P. B. (1972); Phil. Mag. 26, 193.

Hirsch, P. B. and A. Howie, R. B. Nicholson, D. W. Pashly, M. J. Whelan (1965); *Electron Microscopy of Thin Crystals* (Butterworths, Washington).

Hirth, J. P. and J. Loethe (1968); *Theory of Dislocations* (McGraw-Hill, New York), p. 202.

Howie, A. and Z. S. Basinski (1968); *Phil. Mag.* 17, 1039.

Joshi, M. L. (1966); *Acta Met.* 14, 1157.

Joy, D. C. and D. M. Maher (1975); 33rd EMSA Proc. (G. W. Bailey, Las Vegas), p. 204.

Lifshin, E., W. G. Morris, and R. B. Bolon (1969); *Jour. of Met.* 44, 227.

Mahajan, S., G. A. Rozgongji, and D. Brasen (1977); *Appl. Phys. L.* 30, 73.

Maher, D. M. and D. C. Joy (1976); *Mic. Soc. of Canada* 3, 18.

Muraka, S. P. (1977); *J. Vac. Sci. Tech.* 14, 47.

Poole, J. B. (1947); *Philips Techn. Rev.* 9, 33.

Ravi, K. V. (1974); *Phil. Mag.* 30, 1081.

Ravi, K. V. (1974); *Phil. Mag.* 31, 405.

Runyan, B. J. (1965); *The Metallurgy of Silicon* (Texas Instruments Technical Report, Dallas, Texas).

Reimer, L. and P. Aagemann (1976); IITRI, Chicago, 1976, 321.

Thöslén, A. R. (1970); *Phil. Mag.* 22, 175.

Thomas, L. E. (1972); *Phil. Mag.* 24, 1447.

Thompson, M. N. (1977); *A Review of TEM Microdiffraction Techniques* (Philips Technical Report, Eindhoven, Netherlands).

Van Oostrum, K. J., A. Leenhouts, and A. Jore (1973); *Appl. Phys. L.* 23, 283.

Whelan, M. J. and P. B. Hirsch (1957); *Phil. Mag.* 2, 1303.

BIOGRAPHICAL SKETCH

John Beverly Warren was born October 29, 1944, in Omaha, Nebraska. He attended Cornell University in Ithaca, New York, and graduated in 1967, with the Bachelor of Science degree in Materials Science. After receiving the Master of Engineering from the Department of Materials Science and Engineering at the University of Florida in 1968, he entered the United States Army and served in Boston and Korea.

At the conclusion of military service, the author re-entered the Department of Materials Science and completed his graduate studies in 1976.

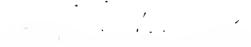
John Beverly Warren is married to the former Barbara-Jean Panessa of New York City. He is now employed at the Brookhaven National Laboratory.

I certify that I have read this study and that in my opinion it conforms to acceptable standards of scholarly presentation and is fully adequate, in scope and quality, as a dissertation for the degree of Doctor of Philosophy.



John J. Hren, Chairman
Professor of Materials Science
and Engineering

I certify that I have read this study and that in my opinion it conforms to acceptable standards of scholarly presentation and is fully adequate, in scope and quality, as a dissertation for the degree of Doctor of Philosophy.



Robert E. Reed-Hill
Professor of Materials Science
and Engineering

I certify that I have read this study and that in my opinion it conforms to acceptable standards of scholarly presentation and is fully adequate, in scope and quality, as a dissertation for the degree of Doctor of Philosophy.



Craig S. Hartley
Professor of Materials Science
and Engineering

I certify that I have read this study and that in my opinion it conforms to acceptable standards of scholarly presentation and is fully adequate, in scope and quality, as a dissertation for the degree of Doctor of Philosophy.



Robert T. DeHoff
Professor of Materials Science
and Engineering

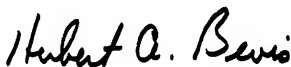
I certify that I have read this study and that in my opinion it conforms to acceptable standards of scholarly presentation and is fully adequate, in scope and quality, as a dissertation for the degree of Doctor of Philosophy.



Martin Eisenberg
Professor of Engineering Sciences

This dissertation was submitted to the Graduate Faculty of the College of Engineering and to the Graduate Council, and was accepted as partial fulfillment of the requirements for the degree of Doctor of Philosophy.

June, 1978



Dean, College of Engineering

Dean, Graduate School

UNIVERSITY OF FLORIDA



3 1262 08553 2850